Master of Science Thesis

Spatio-Temporal Stability Analysis of Shear Flows

Using analytical and non-analytical approaches

N. Kumar

October 14, 2016

Faculty of Mechanical, Maritime and Materials Engineering (3mE)
Delft University of Technology

Spatio-Temporal Stability Analysis of Shear Flows

Using analytical and non-analytical approaches

Master of Science Thesis

For obtaining the degree of Master of Science in Mechanical Engineering at Delft University of Technology

N. Kumar

October 14, 2016

P&E report number: 2786

Faculty of Mechanical, Maritime and Materials Engineering (3mE)
Delft University of Technology

The work in this thesis was done at The von Kármán Institute for Fluid Dynamics, Belgium.

Delft University Of Technology
Department Of
Process and Energy (P&E)

The undersigned hereby certify that they have read and recommend to the Faculty of Mechanical, Maritime and Materials Engineering (3mE) for acceptance a thesis entitled

Spatio-Temporal Stability Analysis of Shear Flows

by

N. Kumar

in partial fulfillment of the requirements for the degree

of

Master of Science Mechanical Engineering.

Dated: October 14, 2016

Graduation committee member(s):

Prof. Dr. ir. B.J. Boersma

Prof. Dr. ir. B.W. van Oudheusden

Dr. ir. R. Pecnik

Dr. ir. F. Pinna

ir. K.J. Groot

Reader(s):

Abstract

A comprehensive understanding of the stability of shear flows is a fundamental problem in fluid mechanics and it has been a subject of both theoretical and practical interest in engineering research. A key aspect of these dynamic flows is the behaviour exhibited by the instabilities as it evolves from initial small perturbations of an equilibrium state, and may lead to fluctuations. In order to control these fluctuations, a study on the spatial and temporal evolution of the perturbations must be carried out.

The objective of this thesis is to perform the spatio-temporal stability analysis on the plane, incompressible shear layers representing confined and unconfined shear flows. The analysis requires the estimation of the response of the flow to the initial perturbations for fixed values of relevant parameters. The numerical tools are developed for the low order piecewise linear profile approximations to the shear layers. The influence of typical flow features, like single and multiple shear dynamics, on the stability behaviour is studied and the convective/absolute instability boundary for various parameter combinations are identified. After validation for the analytical models, the numerical tools are extended to the non-analytical models. The analysis is then performed for higher order approximations of the experimental base flows in order to validate the results from the toolkit.

A variation of the flow features and variables can change the stability behaviour of the shear flows. The single shear layer dynamics cannot contribute to absolute instability in the absence of a dispersive medium, like surface tension. The surface tension acts as a stabilising mechanism for perturbations of short wavelength. The multiple shear layer dynamics dictates that the unconfined jet or wake flow is more unstable than the single shear layer with equivalent parameter values, and that very high values of surface tension stabilises all perturbations. For confined jet or wake flows, the varicose mode perturbations are found to be highly absolutely unstable in the strongly confined dense inner flow limit. The temporal branches obtained from the toolkit match with the Linear Stability Theory (LST) results. This is a key result that allows the extension of the numerical tools developed for the low order analytical models to be applied to the non-analytical models obtained for higher order approximations of the experimental base flow.

Contents

List of Symbols

Roman symbols

c	phase speed, ω/α	ms^{-1}
c_g	group speed, $\mathrm{d}\omega/\mathrm{d}\alpha$	ms^{-1}
$\mathcal{D}$	dispersion relation	–
g	growth rate	s^{-1}
$\mathcal{G}$	Green's function	–
h	confinement parameter	–
h_w	distance of shear layer from wall	m
H	Heaviside step function	–
$\mathcal{J}$	momentum flux	–
k	wavenumber	m^{-1}
L_d	length of computational domain	–
$\mathcal{M}$	mass flux	–
N	number of points in Chebyshev collocation grid	–
$\mathcal{O}$	"big-O"-symbol denoting order of magnitude	–
p	pressure	$\mathrm{N/m}^2$
$\mathbf{q}$	vector of generic flow variable	–
Re	Reynolds number	–
S	density ratio	–
t	time	s
u	streamwise velocity	m/s
v	wall-normal velocity	m/s
V	speed of observer	m/s
w	spanwise velocity	m/s
We	Weber number	–
x	streamwise direction	m
y	wall-normal direction	m
z	spanwise or axial direction	m

Greek symbols

α	streamwise component of wavenumber	m^{-1}
β	spanwise component of wavenumber	m^{-1}
δ_v	vorticity thickness	m
Δ	jump in parameter value	–
ϵ	small parameter	–
η	integer exponent in algebraic approximation of shear layer	–
Λ	velocity ratio	–
ω	frequency	s^{-1}
ϕ	perturbation streamfunction amplitude	m^2/s
ψ	streamfunction	m^2/s
ρ	density	kg/m^3
σ	surface tension	N/m
Σ	surface tension parameter	–
τ	parametric variable	–
Θ	phase function	–
ξ	wavenumber, $\mathrm{sgn}(k_\mathrm{r}).k$	m^{-1}

Sub- and Super-scripts

$\overline{[\cdot]}$	steady base flow
$[\cdot]'$	linearised perturbations of the equilibrium state
$\widetilde{[\cdot]}$	shape function/amplitude of the perturbations
$\widehat{[\cdot]}$	variable after applying Squire's transformation
$[\cdot]_\mathrm{s}$	saddle point
$[\cdot]^\mathrm{d}$	dimensional value
$[\cdot]_\mathrm{ref}$	reference value
$[\cdot]_\mathrm{max}$	maximum value
$[\cdot]_\mathrm{min}$	minimum values

Acronyms

CAIB	Convective/Absolute Instability Boundary
DAC	Domain of Absolute Convergence
DNS	Direct Numerical Simulation
ICP	Inductively Coupled Plasma
LNSE	linearised Navier-Stokes equation
LST	Linear Stability Theory
PIV	Particle Image Velocimetry
SWBLI	Shock-Wave/Boundary-Layer Interaction
TPS	Thermal Protection System
VESTA	VKI Extensible Stability and Transition Analysis toolkit
VKI	The von Kármán Institute for Fluid Dynamics
WKBJ	Wentzel-Kramers-Brillouin-Jeffreys approximation

Chapter 1

Introduction

1.1 Motivation

During the re-entry of a space vehicle into the atmosphere at hypersonic speeds, an extremely hot layer of charged particles, known as *plasma*, forms in the flow near the surface of the vehicle. The vehicle is shielded from the large amount of heat generated in the plasma flow by the thermal protection system (TPS). In order to test the TPS, the harsh re-entry conditions are replicated in ground based test facilities. Particularly, in the VKI plasmatron facility, a subsonic plasma *jet* discharging into a test chamber is generated. A probe is placed facing the jet which forces the formation of a subsonic plasma boundary layer.

The hot plasma flow over the TPS can cause erosion of the surface. The surface irregularity may contribute to surface roughness and influence the boundary layer flow. The similar phenomena is encountered in flow over micro-ramps. Micro-ramps are sub-boundary-layer or micro-vortex generators that are used to suppress the shock-wave/boundary-layer interaction (SWBLI), see Groot *et al.* [9]. The micro-ramps reduce the extent of flow separation in the interaction by generating two steady counter-rotating vortices. A train of hairpin vortices develops in the shear layer surrounding the micro-ramp's *wake*. The vortical structures can be interpreted as inviscid Kelvin-Helmholtz (KH) modes.

In both the *jet* and *wake* flows, an initial perturbation may evolve as fluctuation in the downstream flow domain. The fluctuations are associated with noise generation and energy dissipation in the flow. This induces drag, and also enhances mixing if the two streams contain different fluids, see Schmid & Henningson [27]. The dynamical behaviour of the the jet and wake flows must, therefore, be studied in order to control the fluctuations. Classically, the jet and wake flows have been modelled as a combination of *shear layers*. The plane shear layer is a classical example of turbulent shear flow away from walls. A typical shear layer is formed by the merger of two parallel streams of different velocities, initially separated by a thin plate.

An unsteadiness generated in the initial flow could be convected by the shear layer in the downstream direction or it may evolve locally at the source, often leading to instability. The main sources of instability can be vortex shedding or hydrodynamic perturbations. Depending on the

spectral composition of the disturbance and the variable magnitudes of the shear flow, the disturbance can be either amplified or damped. An analysis of the shear layer unsteadiness, therefore, needs to be performed for an understanding of the physics underlying the fluctuations. A comprehensive study of the evolution of the perturbations provides a necessary tool to control the flow variables at desired spatial and temporal locations.

1.2 Background and literature review

The problem of stability appears in various dynamic flows in physics and engineering applications. A striking aspect in these systems is the behaviour exhibited by instabilities as it evolves from initial small perturbations of an equilibrium state. This is especially true for fluid flow applications. If the system is such that the flow parameters are concentrated at isolated points in the flow, in order to describe the system by ordinary differential equations, then the stability problem can be solved by using linear approximations. As a rule, for small amplitudes of perturbations, these linearised flow models describe the instabilities. However, for flows where the system parameters are not concentrated but distributed, the system is described by partial differential equations or ordinary differential equations (both nonlinear). Also, when the amplitude of unstable perturbations becomes appreciable, the linearised models cease to be valid. To estimate how linear instabilities modify an equilibrium state to a nonlinear state, their evolution is studied using either temporal theory and/or spatial theory.

For the derivation of spatial stability equations, the temporal growth of the disturbance (given by imaginary frequency, ω_i) is neglected. Therefore, we assume a complex streamwise wavenumber ($k \in \mathbb{C}$) and a real frequency ($\omega \in \mathbb{R}$). On the other hand, the temporal stability equations are derived in an analogous manner by assuming real wavenumber ($k \in \mathbb{R}$) and complex frequency ($\omega \in \mathbb{C}$). The goal of the linear stability theory is then to determine the complex eigenvalues as a function of the real frequency or wavenumber.

As a pre-requisite, a general system that is time-invariant and uniform in at least one spatial dimension (y) is considered. In Cartesian coordinates, a generic flow variable, given by, say, the vector $\mathbf{q}(\mathbf{x}, t)$ can be decomposed as

$$\mathbf{q}(\mathbf{x}, t) = \overline{\mathbf{q}}(y; R) + \mathbf{q}'(\mathbf{x}, t)\,, \tag{1.1}$$

where, $\overline{\mathbf{q}}(y; R)$ is the steady base flow that satisfies the Navier-Stokes equations, $\mathbf{q}'(\mathbf{x}, t)$ is the linearised perturbations of the equilibrium state, and R is a control parameter. If we consider the homogeneity in time and spatial dimensions x and z, $\mathbf{q}'(\mathbf{x}, t)$ can be taken to be of the form

$$\mathbf{q}'(\mathbf{x}, t) = \widetilde{\mathbf{q}}(y)\mathrm{e}^{\mathrm{i}(\alpha x + \beta z - \omega t)}\,, \tag{1.2}$$

which is the decomposition of the perturbations into elementary stability waves of complex $\mathbf{k}$ (where $|\mathbf{k}| = \sqrt{\alpha^2 + \beta^2}$) and ω. As evident from the discussion in Schmid & Henningson [27], the distribution function $\widetilde{\mathbf{q}}(y)$ satisfies the ordinary differential equation of Orr-Sommerfeld type. Incorporating the boundary conditions, this leads to eigenvalue problem where the eigenfunctions $\widetilde{\mathbf{q}}(y)$ exist only if only when $\mathbf{k}$ and ω are constrained to satisfy the dispersion relation of the form

$$\mathcal{D}(\alpha, \beta, \omega; R) = 0\,. \tag{1.3}$$

If for some real value of wavenumber, certain complex value(s) of frequency ω exist(s) such that $\mathrm{Im}(\omega) > 0$, then the plane monochromatic wave form of perturbation given by ansatz 1.2 will increase as $t \to \infty$. The dynamic system, as a result, will be unstable.

In practical applications, the small perturbations are not in the form of individual plane monochromatic waves, but in the form of wave packets. The asymptotic behaviour of wave packets differs from the behaviour of monochromatic waves. For instance, even though the individual components of the wave packet increase unbounded in time, the entire wave packet as a whole, when observed from a fixed reference frame, may still remain bounded as the perturbation can *drift* downstream. Therefore, to get a clear understanding of the instability of a dynamic system, instead of restricting the focus only to time growth, the development of the initial perturbations needs to be studied.

Most of the pioneering contributions to the theoretical fundamentals have been made by plasma physicists. The distinction between convective and absolute instabilities was first formalized by Sturrock [28]. In the paper, he suggests using wave kinematics interpreted from the dispersion relation to distinguish between convective and absolute instability. Following Huerre & Monkewitz [12], the objective of instability analysis is to characterize the relationship between *global* and the *local* instability modes. To achieve this, it is essential to assume that the streamwise variation of the basic flow is small over the typical instability wavelength (parallel-flow or WKBJ approximation), and the instability is not dominated by long-range pressure feedback. The *local* instability is defined by Yu & Monkewitz [33] as the instability of a hypothetical parallel flow with velocity and density profiles matching the ones of the nonparallel flow at a given downstream location. On the other hand, the *global* instability refers to the entire flow field. On a local level at each streamwise location, the absolute and convective instabilities mentioned in the previous paragraph characterize the linear impulse response of the parallel flow. In *local absolute instability*, the localised disturbances grow in both the upstream and downstream directions and contaminate the whole flow domain. By contrast, in *local convective instability*, the disturbances *drift* away from the source. Huerre & Monkewitz [12] suggest that the temporal growth of a linear *global* mode is only possible when the flow consists of a region of *local absolute instability*. However, a local absolute instability does not necessarily lead to self-excited oscillations. Therefore, the search for absolute instability gives an efficient, but case-dependent, way of searching the parameter space of complex nonparallel flow for occurrence of self-sustained temporally growing *global* modes.

For ansatz 1.2, Gaster [7] proposes relations for the frequency and amplification rates for temporal (T) and spatial (S) settings.

$$k_{\mathrm{r}}(\mathrm{T}) = k_{\mathrm{r}}(\mathrm{S}), \quad \omega_{\mathrm{r}}(\mathrm{T}) = \omega_{\mathrm{r}}(\mathrm{S}), \quad \text{and} \quad \frac{\omega_{\mathrm{i}}(\mathrm{T})}{k_{\mathrm{i}}(\mathrm{S})} = -\frac{\partial \omega_{\mathrm{r}}}{\partial k_{\mathrm{r}}}\,. \tag{1.4}$$

In spatial stability analysis, these transformations are useful in deciding the initial guess value of k, therefore, simplifying the analysis to the level of temporal stability analysis.

We will briefly discuss the hydrodynamic instability description. Traditionally, the experimental observations of hydrodynamic instability of open flows have been compared with the results of local *spatial* stability problems (given real ω and unknown complex $\mathbf{k}$) dealing with the measured time averaged mean velocity profile at each streamwise location. This approach has been successful in describing the downstream evolution of vortical structures in controlled experiments. The analysis performed by Gaster *et al.* [8] presents one example. However, majority of the hydrodynamic stability literature has been devoted to the *temporal* theory (given real $\mathbf{k}$ and unknown complex

ω) dealing with evolution of flow from a given initial state. The application of local spatial theory with fixed real ω to some open shear flows (*e.g.* hot jets) is not sufficient. Both $\mathbf{k}$ and ω need to be considered complex here. This analysis may give global temporal instability where the flow admits self-sustained global modes.

The local or global and absolute or convective instability concepts discussed above can be applied to differentiate the open shear flows based on their dynamic behaviour. According to Huerre & Monkewitz [12], local convectively unstable shear flows (*e.g.* mixing layers) exhibit extrinsic dynamics;,*i.e.*, their evolution being determined by the excitation parameters. Such flows behave like *amplifiers*. On the other hand, shear flows with pockets of absolute instability (*e.g.* bluff -body wakes) exhibit intrinsic dynamics; temporally growing global modes are present in downstream convected perturbations. Such flows, that are dependant on the temporal growth of initial perturbations and not on the spatial amplification of external excitation, are known as *oscillators*.

It was first remarked by Twiss [30–32], and Landau & Lifshitz [19] that in a perturbed medium, a disturbance can evolve in two physically distinct ways. To arrive at this distinction, the perturbations $\mathbf{q}'(\mathbf{x},t)$ are assumed to satisfy the system of constant coefficient partial differential equations. Following the work in Huerre & Monkewitz [12], it is realised that the differential operator $\mathcal{D}\left[-\mathrm{i}(\partial/\partial x),(\partial/\partial y),-\mathrm{i}(\partial/\partial z),\mathrm{i}(\partial/\partial t);R\right]$ in physical space (x,t) can be associated to the relation 1.3 in the spectral space $(\mathbf{k},\omega)$. The perturbations therefore satisfy

$$\mathcal{D}\left[-\mathrm{i}\frac{\partial}{\partial x},\frac{\partial}{\partial y},-\mathrm{i}\frac{\partial}{\partial z},\mathrm{i}\frac{\partial}{\partial t};R\right]\mathbf{q}'(\mathbf{x},t)=0\,. \tag{1.5}$$

If the perturbations in a wave packet $\mathbf{q}'(\mathbf{x},t)$ remain bounded (or $\mathbf{q}'(\mathbf{x},t)\to 0$) for a stationary frame of reference as $t\to\infty$, it is a *convective* instability. On the other hand, if the perturbations are unbounded (or $\mathbf{q}'(\mathbf{x},t)\to\infty$) for a fixed reference frame as $t\to\infty$, it is an *absolute* instability.

The mathematical framework for the study of plasma instabilities governed by Eq. 1.5 has been an integral part of the problem of distinguishing between spatially amplifying and evanescent waves. Sturrock [28], Briggs [3] and Bers [2] have developed methods that are now the standard procedure to distinguish between the amplifying and evanescent waves. A comprehensive review of the theoretical and experimental work for open shear flows (*e.g.* mixing layers, jets, wakes, boundary layers, etc.) can be found in Huerre & Monkewitz [12].

The integro-differential equations of the form 1.5, and particularly the linearised Ginzburg-Landau equations, have been studied extensively to identify the possible transition mechanisms in open-flow systems. For these equations, the Green's function $\mathcal{G}(\mathbf{x},t)$ defines the impulse response of the system. It is defined for the general differential problem given by Eq. 1.5 as

$$\mathcal{D}\left[-\mathrm{i}\frac{\partial}{\partial x},\frac{\partial}{\partial y},-\mathrm{i}\frac{\partial}{\partial z},\mathrm{i}\frac{\partial}{\partial t};R\right]\mathcal{G}(\mathbf{x},t)=\delta(x)\delta(z)\delta(t)\,. \tag{1.6}$$

The formal distinction between convective and absolute instabilities is obtained by obtaining the asymptotic behaviour of the Green's function at the source, which is defined along a ray $x_n/t=0$, $n=1,2,3$. The basic flow is *convectively unstable* if

$$\lim_{t\to\infty}\mathcal{G}(x_n,t)=0\quad\text{along the ray } x_n/t=0\,, \tag{1.7}$$

and *absolutely unstable* if

$$\lim_{t\to\infty} \mathcal{G}(x_n, t) = \infty \quad \text{along the ray } x_n/t = 0\,. \tag{1.8}$$

The Green's function is evaluated as a double Fourier integral in the (k, ω)-space. Additionally, the most significant contribution to the asymptotic response is given by the wavenumber k_0 for which the group velocity is zero. In other words, for focus is along the ray $x_n/t = 0$ at a *fixed* spatial location. For simplicity, the cross-stream variations are neglected and the spatio-temporal evolution is restricted to the (x, t)-plane. Also, it is assumed that the system 1.3 admits only a single temporal mode $\omega(k)$. The complex k_0 is given by

$$\frac{\partial \omega}{\partial k}(k_0) = 0\,. \tag{1.9}$$

The corresponding *absolute frequency* is given as $\omega_0 \equiv \omega(k_0)$. The *absolute growth rate* is then given as $\omega_{0,\mathrm{i}} \equiv \omega_{\mathrm{i}}(k_0)$. It characterises the asymptotic temporal evolution of the wavenumber k_0 observed from a fixed location.

$$\begin{aligned} \omega_{0,\mathrm{i}} &> 0 \quad \text{for absolutely unstable flow, and} \\ \omega_{0,\mathrm{i}} &< 0 \quad \text{for convectively unstable flow}\,. \end{aligned} \tag{1.10}$$

Typically, ω_0 is an algebraic branch point of the mapping $k(\omega)$ in the complex ω-plane, or k_0 is a saddle point of the mapping $\omega(k)$ in the complex k-plane.

In the seminal works of Briggs [3] and Bers [2], it is highlighted that the conditions given by Eqs. 1.9 and 1.10 are not sufficient to serve as an absolute-convective instability criterion. For simplicity, it is assumed that the temporal mode $\omega(k)$ exhibits a quadratic algebraic branch-point ω_0 with only two spatial branches $k^+(\omega)$ and $k^-(\omega)$. During the simultaneous *deformation* of the integral contours in the (k, ω) space to evaluate the response $\mathcal{G}(\mathbf{x}, t)$, the condition arises the k-plane when the Fourier contour is *pinched* between the branches $k^+(\omega)$ and $k^-(\omega)$. This pinching happens exactly at the saddle point k_0. As indicated by Kupfer *et al.* [18], the ω-plane consists of a cusp at ω_0 in the locus of $\omega(k)$ corresponding to the pinch point k_0. As evident from Eq. 1.10, for absolute (convective) instability, ω_0 must be located in upper (lower) half of the ω-plane. This procedure to distinguish the instability type is known as the Briggs or Briggs-Bers criterion.

Unlike the simple case discussed above, there might be flows (*e.g.* mixing layers) where the temporal modes $\omega(k)$ exhibit non-analytical behaviour. Huerre & Monkewitz [11] provide a remedy by associating the real signal with a complex *analytical* signal. Moreover, due to the complexity of the physical problem (*e.g.* smooth shear layer profiles studied by Balsa [1]), the solution to the dispersion relation in the temporal (linear eigenvalue problem in ω) or spatial (nonlinear eigenvalue problem in k) setup is obtained numerically. Both types of eigenvalue problems can be solved using shooting methods. To solve the problem of distinguishing between branches in complex k/ω-space in a spatio-temporal stability analysis, Suslov [29], suggested an automatic eigenvalue tracking algorithm.

In this thesis, jet/wake flows have been studied. The effect of density variations in promoting absolute instability has been verified by Monkewitz & Sohn [23] for the axisymmetric jet and by Yu & Monkewitz [33] for planar jet. The homogeneous, incompressible jets have been shown to be convectively unstable everywhere. Experimental study to validate the existence of self-sustained

global oscillations in jets was performed by Monkewitz *et al.* [23] for hot round jet and by Yu & Monkewitz [33] for hot planar jet. An additional class of confined jet flows such as those found in fuel injectors has been numerically and experimentally studied over the last five decades. Recently, Juniper [17], [15], [16] gave a comprehensive study of the jet (and wake) flows. They considered a continuous range of confinement defined by the ratio h of the outer flow thickness, h_2, to inner flow thickness, h_1, or $h = h_2/h_1$. The range of $h = 0.1$, for strong confinement, to $h = 10$, for weak confinement, was studied. This is physically equivalent to matching the wavenumber of the principal flow-mode of the inner and outer flows. Other regions of high instability appear due to the interaction of harmonics of the inner and outer flows. For certain confinement ratios, the results from Juniper [17] indicate that the flow can be absolutely unstable.

1.3 Objectives

The main goal of the project is to perform a spatio-temporal stability analysis on the plane shear layers for the three types of flows - unconfined single shear layer, confined and unconfined jets/wakes, and semi-unconfined shear layer. To achieve this goal, the project can be subdivided into following objectives.

The first objective is to develop and validate the numerical tool using MATLAB and MAXIMA to obtain the analytical dispersion relation for different configurations of shear flows, and use it in conjunction with the Briggs-Bers criterion for spatio-temporal stability analysis. The detailed study of the analytical models gives a better understanding of the underlying physics of the flow. The application of the analytical approach includes, but is not limited to, calculating the impulse response which gives the asymptotic evolution of the perturbation.

The second objective is to implement and validate the numerical tools for a shear flow with non-analytical dispersion relation. The task is to combine the linear stability theory (LST) tools in the VKI extensible stability and transition analysis (VESTA) toolkit with the numerical implementation performed for the analytical dispersion relations. This forms a new branch of the VESTA toolkit which is capable of predicting the spatio-temporal behaviour of the shear flow. The results need to be validated with the literature.

The third and last objective is to develop and verify a numerical tool to identify the convective/absolute instability boundary (CAIB). The tool is required to span the parameter space to identify the locations where the growth rate ω_i is zero and therefore traverse along the transition boundary.

The spatio-temporal stability analysis has been studied under the small perturbations limit for inviscid shear flows. The assumptions are explained in detail in the following paragraphs.

Firstly, the disturbances are assumed small in comparison with the mean flow and the problem is linearised around the base solution,*i.e.*, the laminar mean flow. For free shear layers, this is true at a point immediately downstream of the location where the perturbation is triggered, exhibiting oscillatory behaviour with small amplitudes. Further downstream, the perturbation amplitude may increase up to a level where it is no longer small compared to the mean flow and the non-linear effects take over. The perturbation amplitude could be so high that it may set transition and the flow becomes turbulent. The current study is valid for study of experimental flows with probe placement near the perturbation origin.

Secondly, the instabilities in steady parallel flows can be classified in two groups. The *inertial* instability is inviscid and is unstable as long as the Reynolds number is above a low threshold, $Re \approx 1 - 10$. The disturbances grow in time comparable to the turnover time of the base flow, $t = \mathcal{O}(\delta_v/\Delta U)$. These instabilities can be studied using the Rayleigh's stability equation. The second group of instabilities is appears in flows that are stable to the perturbations of the first type and depend on the viscosity for destabilising mechanisms. The growth rates of the second type of instabilities is much lower than the inertial type, see Jiménez [13], and therefore are not considered in this study.

1.4 Outline

Chapter 2 is concerned with the development of the theoretical framework that is used to identify the spatio-temporal behaviour of the shear flow. This theory has been used throughout the thesis. The Briggs-Bers criterion for the identification of absolute/convective instability has been introduced and a mathematical explanation of the criterion is given in Appendix A.

Chapter 3 develops the numerical procedure for the spatio-temporal stability analysis of the analytical and non-analytical dispersion relations. The governing equation for the planar inviscid shear flows with piecewise linear profiles is derived, with the details given in Appendix B and Appendix C. The numerical implementation for smooth profiles using VESTA toolkit is explained.

Chapter 4 reviews the stability of various simple shear layer models for which the analytical dispersion relations has been derived using MAXIMA. These form the basis to implement and validate the results of the non-analytical models in later part of the thesis. The complexity of the model is increased from single shear layer without confinement to the double shear layer with confinement.

Chapter 5 is concerned with the numerical implementation of the non-analytical model using VESTA. The convergence study is performed and the results are validated with the literature.

Chapter 6 deals with the identification of the transition boundary where the flow changes its behaviour from being convectively unstable to absolutely unstable or vice versa. The parametric tracking method of the neutrally stable saddle point is developed. The method is then applied to various shear flows and result is validated with the literature.

The conclusion of this project and research direction for the future work are discussed in Chapter 7.

□

Chapter 2

Theoretical framework

2.1 Modal stability theory

The instability of flows to small amplitude perturbations has been conventionally studied using *modal* approach. In this section, the pedagogical treatment by Juniper *et al.* [16]) followed. In this approach, an operator that describes the evolution of small perturbations is derived from the governing equations. The *modal* approach considers the temporal or spatial development of the individual eigenmodes of the operator. This leads to the *modal* linear stability theory (LST) where a flow quantity $\mathbf{q}$ is decomposed into a steady part $\overline{\mathbf{q}}$, which is also the *base* flow [1], and an unsteady part $\mathbf{q}'$

$$\mathbf{q}(\mathbf{x}, t) = \overline{\mathbf{q}}(\boldsymbol{x}) + \epsilon \mathbf{q}'(\mathbf{x}, t)\,, \tag{2.1}$$

where $\boldsymbol{x}$ is the space coordinate vector, t is the time, and $\epsilon \ll 1$ is the amplitude. The *linearised Navier-Stokes equations* (LNSE) can be derived from the decomposition Eq. 2.1. For incompressible flows, the LNSE is given as

$$\frac{\partial \mathbf{u}'}{\partial t} + \mathbf{u}' \cdot \nabla \mathbf{u}' = -\nabla p' + \frac{1}{Re} \nabla^2 \mathbf{u}'\,, \tag{2.2}$$

$$\nabla \cdot \mathbf{u}' = 0\,. \tag{2.3}$$

The basic state $\overline{\mathbf{q}}$ is calculated and inserted in the LNSE, which is solved as an in initial-boundary-value problem and are valid for any small amplitude perturbation.

The stability of a basic state to an arbitrary small perturbation can be verified by either solving the LNSE, which is rarely performed, or performing a direct numerical simulation (DNS), which is more prevalent, of the full nonlinear equations of motion. These approaches are computationally

[1] Different from the term *mean* flow, which is used only for the time- and/or space-averaged turbulent flow

expensive. LST offers a cheaper alternative. However, due to the lack of experimental results, numerical solutions of the LNSE or DNS results are used to check the results of LST.

The framework of the LST is defined from the approximation of the homogeneous directions of the basic state $\overline{\mathbf{q}}$, The LST models vary in the level of approximation from the *local* LST, which is based on the assumption of homogeneous basic state along two spatial directions and parallel-flow or WKBJ approximation, to the more general *TriGlobal* LST, where the basic flow is considered inhomogeneous in all spatial dimensions.

Here, we will focus on the *local* stability analysis, *i.e.*, the perturbations will be restricted to *feel* the base flow changes only in the wall normal y-direction. This is achieved by assuming the perturbation $\mathbf{q}'$ to be of the form

$$\mathbf{q}'(\boldsymbol{x},t) = \widetilde{\mathbf{q}}(y)\mathrm{e}^{\mathrm{i}(\alpha x+\beta z-\omega t)}\,, \tag{2.4}$$

where $\widetilde{\mathbf{q}}(y)$ is the *amplitude* function and the terms inside bracket in the exponent is the *phase* function, often represented as $\Theta(x,z,t)$. Inserting the above ansatz into the LNSE Eq. 2.2-2.3, we obtain a one-dimensional eigenvalue problem.

Before going into the details of spatio-temporal stability, the concept of temporal instability, spatial instability, and phase and group velocity will be introduced briefly.

2.1.1 Temporal local stability

The temporal linear stability analysis is performed by fixing the wavenumber parameters in Eq. 2.3 as real ($\alpha,\beta \in \mathbb{R}$). The desired eigenvalue is the complex frequency ($\omega \in \mathbb{C}$). In two dimensional framework ($\beta = 0$), the perturbation formulation becomes

$$\mathbf{q}' = \widetilde{\mathbf{q}}(y)\mathrm{e}^{\mathrm{i}\alpha(x-ct)} + c.c. = \widetilde{\mathbf{q}}(y)\exp\left[\mathrm{i}\alpha(x-(c_\mathrm{r}+\mathrm{i}c_\mathrm{i})t)\right] + c.c.\,. \tag{2.5}$$

Here, the complex eigenvalue ($c = \omega/\alpha$) contains a real part (c_i) which is the phase speed and an imaginary part (c_i) which is the growth rate (either amplification or decay) of the perturbation. The complex conjugate *c.c.* appears in the equation which results from the pair of complex conjugate roots (c) of the eigenvalue problem. As a result of the addition of *c.c.*, the real, physical perturbation $\mathbf{q}'$ is retrieved.

The perturbation can be considered as a linear superposition of monochromatic waves that evolve in x-direction periodic wave packets of lengths equivalent to the periodicity wavelength $\lambda_x = 2\pi/\alpha$. Individual waves propagate at their respective constant phase speed c_r and grow at their respective growth rate $\exp(\alpha c_\mathrm{i} t)$. For asymptotic response ($t \to \infty$), only one of these wave packets with leading eigenmode dominates.

2.1.2 Spatial local stability

In spatial approach, a constant real frequency ($\omega \in \mathbb{R}$) is considered to solve for complex eigenvalue ($\alpha,\beta \in \mathbb{C}$). The linear perturbation equation is written as

$$\mathbf{q}' = \widetilde{\mathbf{q}}(y)\exp\left[\mathrm{i}\left((\alpha_\mathrm{r}+\mathrm{i}\alpha_\mathrm{i})x-\omega t\right)\right] + c.c.\,. \tag{2.6}$$

Here, α_i is the spatial growth rate of the wave while α_r is the wavenumber. The eigenvalue problem to be solved in this framework is nonlinear.

2.1.3 Phase velocity and Group velocity

From Eq. 2.5 it is observed that for a given value of α the value of perturbations $\widetilde{\mathbf{q}}$ becomes constant along a ray with constant value of $(x - ct)$. Therefore, for real α, c is the velocity of the wave crests, the *phase* velocity. If each wavenumber has same phase velocity (*i.e.*, ω is directly proportional to α), the medium is known as *nondispersive*.

In a more general framework, the perturbation is the superposition of several waves. It has an identifiable envelope (Fig. 2.1). The velocity of the envelope is given by *group* velocity ($c_g = \mathrm{d}\omega/\mathrm{d}\alpha$). If the wavecrests of different wavenumbers move at different velocities, the interference pattern changes shape with time and the envelope moves at a different velocity. The medium is known as *dispersive*.

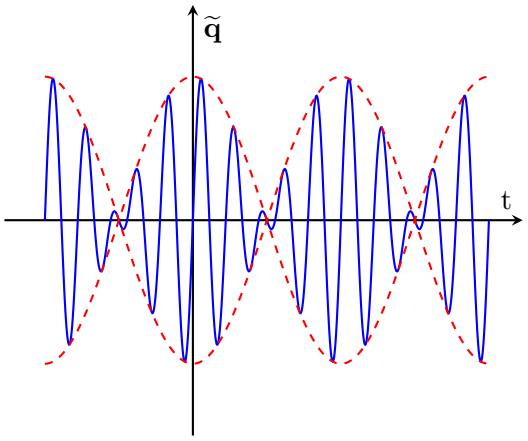

Figure 2.1: Wave packets (solid) and envelope(dashed). Wave crests propagate at phase velocity and envelope travels at group velocity

2.2 Spatio-temporal analysis

As discussed in the previous chapter, a localized pulse on a uniform system can grow and propagate away from the source so that the disturbance decays with time for a fixed point in space – a *convective instability*. Alternatively, the pulse may grow with time at all the points in space – a nonconvective or *absolute instability*. This definition will be illustrated below.

As discussed in the previous section, the linear stability analysis begins with deriving a linearised set of equations that satisfy the governing equations subjected to small perturbations $u'(x,t)$, and describe the response of a simple basic state. Before treating the problem in a general fashion, a standard instability behaviour will be introduced with a simple model.

2.2.1 Stability of a toy model

Following the analysis similar to the one outlined in § 4.6 of Duffy [6], we will consider a linear equation from the toy model proposed by Drazin [5] p70.

$$\frac{\partial u'}{\partial t} + W\frac{\partial u'}{\partial x} = \frac{\partial^2 u'}{\partial x^2} + (R - R_c)u'; \quad -\infty < x < \infty; \quad 0 < t; \quad W, R, R_c \in \mathbb{R}\,. \tag{2.7}$$

The toy problem resembles the Ginzburg-Landau equation which governs the amplitude of perturbations in the fluid flow. It is assumed that the perturbations remain homogeneous in space and time. Therefore, the solutions to Eq. 2.7 can be expressed as a superposition of normal modes,

$$u'(x,t) = A\mathrm{e}^{\mathrm{i}(kx-\eta t)}\,. \tag{2.8}$$

Note that this is a monochromatic perturbation. The relationship between the frequency (η) and wavenumber (k) can be obtained by substituting the solution Eq. 2.8 in the governing equation Eq. 2.7. This is called the *dispersion relation* $\mathcal{D}(k,\eta;R) = 0$, given as

$$\mathcal{D}(k,\eta;R) = -\mathrm{i}\eta + \mathrm{i}Wk + k^2 - (R - R_c)\,. \tag{2.9}$$

Also, the governing equation Eq. 2.7 can be symbolically written as

$$\mathcal{D}\left(-\mathrm{i}\frac{\partial}{\partial x}, \mathrm{i}\frac{\partial}{\partial t}; R\right) u' = 0\,. \tag{2.10}$$

From the dispersion relation Eq. 2.9, it is evident that $\eta = f(k)$, which is given as

$$\eta = Wk + \mathrm{i}\left[(R - R_c) - k^2\right]\,. \tag{2.11}$$

As evident from Eq. 2.8, the perturbations amplify temporally when for a *real* wavenumber ($k \in \mathbb{R}$), a *complex* frequency with $\mathrm{Im}(\eta) > 0$ is obtained. Therefore, the flow is unstable with respect to the temporal growth of spatially periodic disturbances of infinite extent. In this example, instability occurs when

$$\mathrm{Im}(\eta) = (R - R_c) - k^2 > 0, \text{ or } \quad |k| < (R - R_c)\,. \tag{2.12}$$

In most practical applications however, the initial perturbations are *not* monochromatic. The perturbations may now propagate away from the source (Bers [2]). Therefore, even for unstable normal modes, the flow may remain stable in a fixed, local region. Identification of the transition from convective to absolute instability is the prime focus of stability analysis. The application of *Green's function*[2] to the problem gives a clear understanding of this phenomenon.

[2]The Green's function provides an alternative method to solve ordinary differential equations posed as either initial-value problems or boundary-value problems. A problem of the form $Lu(x) = f(x)$, where L is an ordinary linear differential operator, $f(x)$ is a known function, and $u(x)$ is the desired solution, can be written in Green's formulation as $Lg = \delta(x - \xi)$. The solution $u(x)$ is then given as the integral involving the Green's function $g(x|\xi)$ and $f(\xi)$. Refer Duffy [6] for more details.

The solution to the model subjected to an impulse perturbation can be expressed in terms of the Green's function. The Green's function associated with the toy model Eq. 2.7 is given by

$$\frac{\partial g}{\partial t} + W\frac{\partial g}{\partial x} - \frac{\partial^2 g}{\partial x^2} - (R - R_c)g = \delta(x-\xi)\delta(t-\tau); \quad -\infty < x, \xi < \infty; \quad 0 < t, \tau\,. \tag{2.13}$$

This is a two dimensional partial differential equation which is invariant with respect to the time displacement and uniform in spatial dimension. Here ξ denotes the position of the source of perturbation. The Eq. 2.13 governs the effect of an impulse as it propagates from the source at $x = \xi$ as time increases from $t = \tau$. For $t < \tau$, causality requires that $g(x, t|\xi, \tau) = 0$ if the impulse is the sole source of the disturbance. An additional requirement appears in the form of homogeneous boundary condition for the perturbation u' that needs to be satisfied by g.

The Laplace and Fourier transforms are now applied in time and space respectively, to obtain the joint transform $\mathcal{G}(k, s|\xi, \tau)$ as

$$\mathcal{G}(k, s|\xi, \tau) = \frac{\mathrm{e}^{-\mathrm{i}k\xi - s\tau}}{s + k^2 + \mathrm{i}Wk - (R - R_c)}\,. \tag{2.14}$$

Performing the inverse transforms, we get back the Green's function in variables (x, t)

$$g(x, t|\xi, \tau) = \frac{1}{4\pi^2\mathrm{i}} \int_{c-\mathrm{i}\infty}^{c+\mathrm{i}\infty} \int_{-\infty}^{\infty} \frac{\mathrm{e}^{\mathrm{i}k(x-\xi)+s(t-\tau)}}{s + k^2 + \mathrm{i}Wk - (R - R_c)}\,\mathrm{d}k\,\mathrm{d}s\,. \tag{2.15}$$

The Laplace transform in time is inverted first. This gives

$$g(x, t|\xi, \tau) = \frac{H(t-\tau)}{2\pi\mathrm{i}} \int_{-\infty}^{\infty} \exp\left[\mathrm{i}k(x-\xi) - \left[k^2 + \mathrm{i}Wk - (R - R_c)\right](t-\tau)\right]\,\mathrm{d}k\,, \tag{2.16}$$

where H is the Heaviside step function.

$$H(t-\tau) = \begin{cases} 1, & t > \tau \\ 0, & t < \tau \end{cases} \tag{2.17}$$

Finally, performing the inverse Fourier transform in space, we obtain the Green's function as

$$g(x, t|\xi, \tau) = \frac{\exp\left[-(t-\tau)W^2/4 + (x-\xi)W/2 + (t-\tau)(R - R_c)\right]}{2\sqrt{\pi(t-\tau)}} \exp\left[-\frac{(x-\xi)^2}{4(t-\tau)}\right] H(t-\tau)\,. \tag{2.18}$$

We can use the Green's function from Eq. 2.18 to examine the definition of *absolute* and *convective* instabilities given by Bers [2]. these are based on physical intuition. There are three types of instabilities based on the asymptotic behaviour of the Green's function.

① The first type of stability is governed by

$$\lim_{t\to\infty} |g(x,t|\xi,\tau)| \to \infty\,, \tag{2.19}$$

for any arbitrary value of x. This is the condition for *absolute instability*. From Eq. 2.18, it can be inferred that condition 2.19 will be satisfied when $\underline{W=0}$ and

$$(R-R_c) > \frac{W^2}{4} \quad \Rightarrow \underline{R > R_c}\,. \tag{2.20}$$

② The second type of stability is governed by

$$\lim_{t\to\infty} |g(\Xi+vt,t|\xi,\tau)| \to 0\,, \tag{2.21}$$

for some velocity v of the frame of reference and an arbitrary fixed value of Ξ. This is the condition for *absolute stability*; the disturbances will decay in any frame of reference. From Eq. 2.18, the condition 2.21 is satisfied when

$$(R-R_c) < \frac{(W-v)^2}{4}\,. \tag{2.22}$$

As $(W-v)^2$ is always positive, the condition 2.21 will always be satisfied if $\underline{R < R_c}$ and the flow will be *temporally* stable.

③ Finally, the third type of stability is governed by

$$\lim_{t\to\infty} |g(x,t|\xi,\tau)| \to 0, \quad \text{and} \quad \lim_{t\to\infty} |g(\Xi+vt,t|\xi,\tau)| \to \infty\,, \tag{2.23}$$

for some velocity v of the frame of reference and arbitrary fixed values of x and Ξ. The condition 2.23 is satisfied, inferring from the previous two conditions, for $\underline{W\neq 0}$ and $\underline{R > R_c}$. This is the condition for *convective* or *spatial instability*. The disturbances will decay at an arbitrary stationary point but there exists a moving frame of reference in which the disturbances are amplified. As the disturbances convect away from the point of observation, the system returns to its original, unperturbed state.

The system behaviour for different values of $(R-R_c)$ and W is plotted in Fig. 2.2.

The Green's function formulation discussed above can be adapted to apply for general problems where $g(x,t|\xi,\tau)$ cannot be expressed in analytic form.

2.2.2 Stability of a generic system

We start the development of the general analytic tool by acknowledging that a linear, constant coefficient partial differential equation in the perturbation $u'(x,t)$ will have Green's function of the form

$$\begin{aligned} g(x,t|\xi,\tau) &= \frac{1}{4\pi^2\mathrm{i}} \int_{c-\mathrm{i}\infty}^{c+\mathrm{i}\infty} \int_{-\infty}^{\infty} \frac{\mathrm{e}^{\mathrm{i}k(x-\xi)+s(t-\tau)}}{\mathcal{D}(k,s)}\,\mathrm{d}k\,\mathrm{d}s \\ \Rightarrow \quad g(x,t|\xi,\tau) &= \frac{1}{4\pi^2} \int_{-\infty+\mathrm{i}\sigma}^{\infty+\mathrm{i}\sigma} \int_{-\infty}^{\infty} \frac{\mathrm{e}^{\mathrm{i}k(x-\xi)-\mathrm{i}\omega(t-\tau)}}{\mathcal{D}(k,\omega)}\,\mathrm{d}k\,\mathrm{d}\omega\,, \end{aligned} \tag{2.24}$$

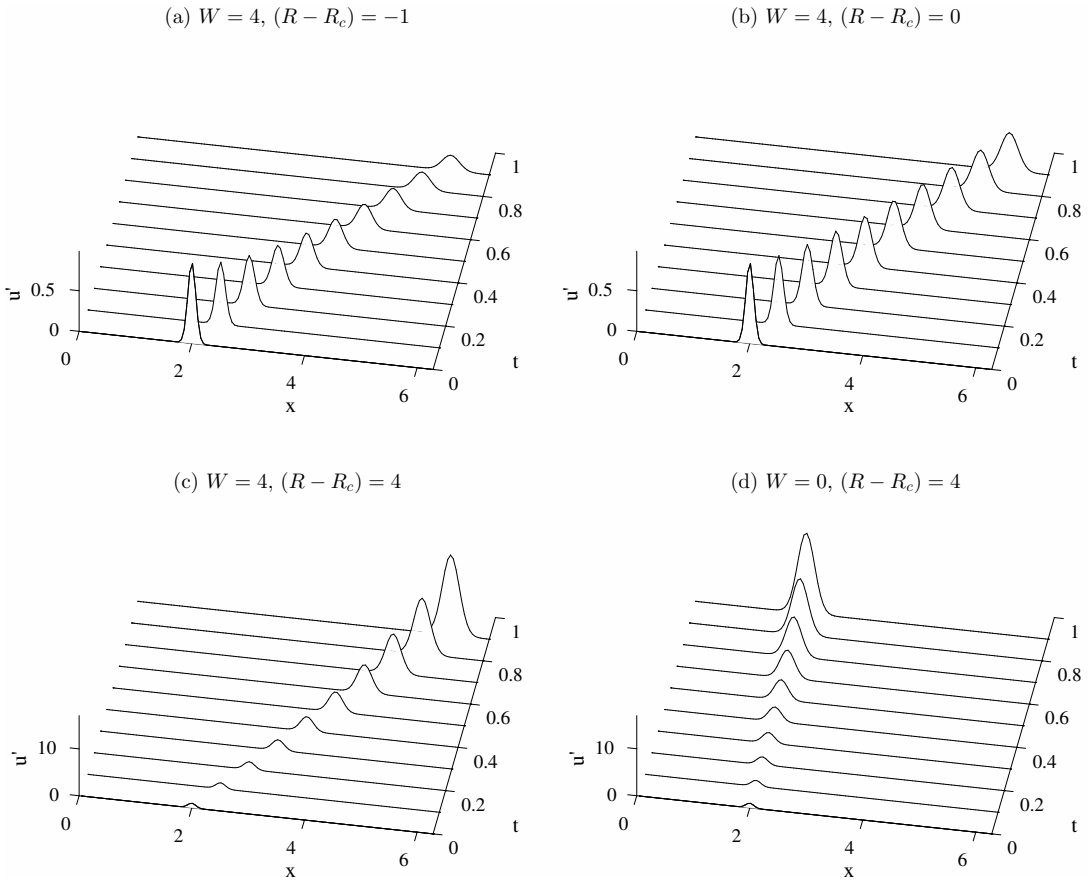

Figure 2.2: Response of the toy model 2.7 to impulse perturbation at $(\xi, \tau) = (2, 0)$. The plots show possible stability scenarios for variable parameters $(R - R_c) = [-1, 0, 4, 4]$ and $W = [4, 4, 4, 0]$: (a) and (b) *temporal* and *absolute stability*, (c) *convective instability*, and (d) *absolute instability*

where the the inverse Laplace transform has been converted to inverse Fourier transform by using $s = -\mathrm{i}\omega$. The integration contour in the complex frequency plane is called the *Bromwich contour*. It is a straight horizontal line located above the singularities of the integrand to satisfy causality. This condition is satisfied in Eq. 2.24 by setting the value of $\sigma > \mathrm{Im}(\omega)$, where ω is obtained from the dispersion relation $\mathcal{D}(k, \omega) = 0$ for a given path in the complex k-plane. The path initially lies on the real k-axis. The maps of the Laplace and Fourier contours with possible closures of the contour integral in k and ω-planes respectively are shown in Fig. 2.3.

We consider a simple case where Eq. 2.24 has a single discrete temporal mode $\omega(k)$. Using residue theorem for the contour integration in ω-plane, the Green's function is given as

$$g(x, t|\xi, \tau) = -\frac{1}{2\pi} H(t - \tau) \int_{-\infty}^{\infty} \frac{\mathrm{e}^{\mathrm{i}[k(x-\xi)-\omega(k)(t-\tau)]}}{\mathcal{D}_\omega\left[k, \omega(k)\right]} \mathrm{d}k\,. \tag{2.25}$$

The Eq. 2.25 can be verified by using the the dispersion relation $\mathcal{D}(k, \omega) = -\mathrm{i}\omega + k^2 + \mathrm{i}Wk - (R - R_c)$, obtained from Eq. 2.15. We have, $\mathcal{D}_\omega\left[k, \omega(k)\right] = -\mathrm{i}$, and $\omega(k) = Wk + \mathrm{i}\left[(R - R_c) - k^2\right]$. These values can be substituted in Eq. 2.25 to recover the Eq. 2.16.

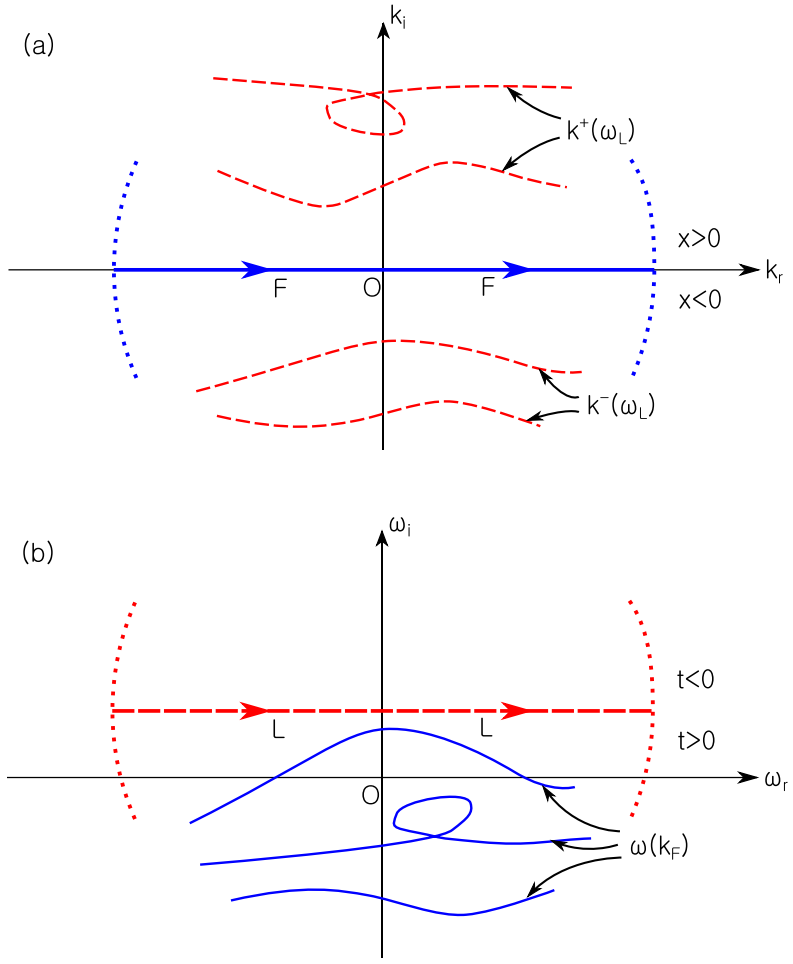

Figure 2.3: (a) Map of the Laplace contour in the complex k-plane (dashed lines), and closures of the Fourier integral contour F (dots) on $k \to \infty$ for $x > 0$ and $x < 0$. (b) Map of the real k-axis in the complex ω-plane (solid lines), and Laplace contour L satisfying causality with closures (dots) on $|\omega| \to \infty$ for $t < 0$ and $t > 0$. (Bers [2])

In general, Eq. 2.25 cannot be evaluated exactly in a similar manner as Eq. 2.16. With careful calculations, the Fourier integral Eq. 2.25 can be performed by the method of steepest descent for $t \to \infty$ and fixed $(x-\xi)/(t-\tau)$. Again, for a simple case, it is assumed that there is only a single stationary point (k_s) where

$$\frac{\partial \omega(k_\mathrm{s})}{\partial k} = \frac{x-\xi}{t-\tau}\,. \tag{2.26}$$

The integration contour in Eq. 2.25 can be deformed from the real k-axis to a steepest descent path passing through the saddle point k_s. The Green's function therefore becomes

$$g(x,t|\xi,\tau) \sim -\frac{\mathrm{e}^{\mathrm{i}\pi/4}}{\sqrt{2\pi}} \frac{\exp\left[\mathrm{i}\left(k_\mathrm{s}(x-\xi) - \omega(k_\mathrm{s})(t-\tau)\right)\right]}{\mathcal{D}_\omega\left[k_\mathrm{s}, \omega(k_\mathrm{s})\right] \sqrt{\omega''(k_\mathrm{s})(t-\tau)}}\,, \tag{2.27}$$

where $''$ represents the second derivative with respect to k. From the dispersion relation for the

toy model, we obtain $\omega''(k_\mathrm{s}) = -2\mathrm{i}$ and

$$k_\mathrm{s} = -\frac{\mathrm{i}W}{2} + \frac{i}{2}\left(\frac{x-\xi}{t-\tau}\right), \quad \text{and} \quad \omega(k_\mathrm{s}) = \mathrm{i}\left[(R-R_c) - \frac{W^2}{4} + \frac{1}{4}\left(\frac{x-\xi}{t-\tau}\right)\right]. \tag{2.28}$$

By substituting these results into Eq. 2.27, the asymptotic evaluation of Eq. 2.25 matches the exact solution Eq. 2.18; but this is not true generally.

The asymptotic response Eq. 2.25 is sufficient for the stability analysis. It is more intuitive to think of the Green's function behaving like a wave packet in the (x,t) plane. The asymptotic response along each ray $(x-\xi)/(t-\tau)$ is dominated by a specific complex wavenumber such that the real group velocity satisfies Eq. 2.26.

2.3 Briggs-Bers criterion

A stability analysis that allows the distinction between convective and absolute instabilities was developed by Briggs [3] and Bers [2]. These are based on the study of pulse response of a continuous medium. For small amplitude perturbations, the analytical treatment of the spatio-temporal impulse response, *i.e.*, Green's function, is sufficient to develop the theory.

The development of the criteria in Briggs [3] and Bers [2] begins with plasma theory but the generic formulation is applicable to fluid dynamic applications also. The Green's function can be expressed in terms of double Fourier integral in the (k,ω) space.

$$\mathcal{G}(\mathbf{x},t) = \int_L \frac{\mathrm{d}\omega}{2\pi}\mathrm{e}^{-\mathrm{i}\omega t}\int_F \frac{\mathrm{d}^2k}{(2\pi)^2}\mathrm{e}^{\mathrm{i}(\alpha x+\beta z)}\frac{1}{\mathcal{D}(\mathbf{k},\omega;R)}. \tag{2.29}$$

The integral is formally evaluated from residue calculation. For simplicity, we will now only consider the evolution of the instability waves in the (x,t)-plane and neglect the variations in the y,z-directions. from Eq. 2.29

$$\mathcal{G}(x,t) = \int_L \frac{\mathrm{d}\omega}{2\pi}\mathrm{e}^{-\mathrm{i}\omega t}\underbrace{\int_F \frac{\mathrm{d}k}{2\pi}\mathrm{e}^{\mathrm{i}kx}\frac{1}{\mathcal{D}(k,\omega;R)}}_{I(x,\omega)}. \tag{2.30}$$

The integration must be performed on contours placed in the domains of absolute convergence (DAC) in the k- and ω-planes. In the k-plane, in order to obtain a well-behaved bidirectional physical response, the DAC is a strip including the real k-axis. In the ω-plane, to satisfy causality, *i.e.*, $\mathcal{G}(x,t) = 0\,\forall\,(x,t<0)$, the DAC is taken as a half plane.

Suppose that the F-contour is fixed on the real k-axis as shown in Fig. 2.3(a). This contour produces a set of images $\omega(k_F)$ in the complex ω-plane through the dispersion relation $\mathcal{D}(k_F,\omega) = 0$, as shown in Fig. 2.3(b). In order to satisfy causality, the L-contour is chosen to lie above the highest branch of $\omega(k_F)$. The image of L given by $k(\omega_L)$ similarly appears on the complex k-plane through the dispersion relation $\mathcal{D}(k,\omega_L) = 0$. It is worth noting that for the L and F contours selected in this manner, the branches in the k-plane do not cross the real k-axis. Therefore, the k-plane integration in Eq. 2.30 exhibits proper division of the modes generated for $x > 0$ and $x < 0$.

After defining the contours, the integrals in Eq. 2.30 are evaluated to obtain the response. As evident from Eqs. 1.7 and 1.8, the time-asymptotic response of $\mathcal{G}(x,t)$ is sufficient to determine the nature of instability. In Fig. 2.3(b), this instability corresponds to a $\omega(k_\mathrm{r})$ branch having $\omega_\mathrm{i}(k_\mathrm{r}) > 0$. The instabilities are distinguished as *convective* and *absolute*. Their importance lies in the transition of the linear perturbations to the nonlinear regime. Absolute instability exhibits build-up of perturbation (oscillator) and the convective instability represents stable amplification of signals (amplifier).

2.3.1 Absolute instability

In this section, the absolute instabilities will be characterized as the normal modes of linearly unstable medium. From the Fig. 2.3, it is evident that the singularities in the ω-plane between the L-contour and the real ω-axis can inhibit the extension of the domain of absolute convergence to the lower-half ω-plane. This forces the deformation of the F-contour as shown in Fig. 2.4. The singularities of the integral $I(x,\omega)$ (Eq. 2.30) 'appear' at the values of ω for which the F-contour cannot be deformed further (without violating causality) as the L-contour is lowered. At $\omega = \omega_\mathrm{s}$, the *pinch* point in the k-plane exhibits a double root at $k = k_\mathrm{s}$, implying

$$\mathcal{D}(k_\mathrm{s},\omega_\mathrm{s}) = 0 \quad \text{and} \quad \frac{\partial \mathcal{D}}{\partial k}(k_\mathrm{s},\omega_\mathrm{s}) = 0\,. \tag{2.31}$$

The Briggs-Bers criterion states that the pinch point will introduce singularity in $I(x,\omega)$ at $\omega = \omega_\mathrm{s}$ only for the double roots in the k-plane that merge by the pinching (by one k^+ and one k^- branch) of the deformed F-contour.

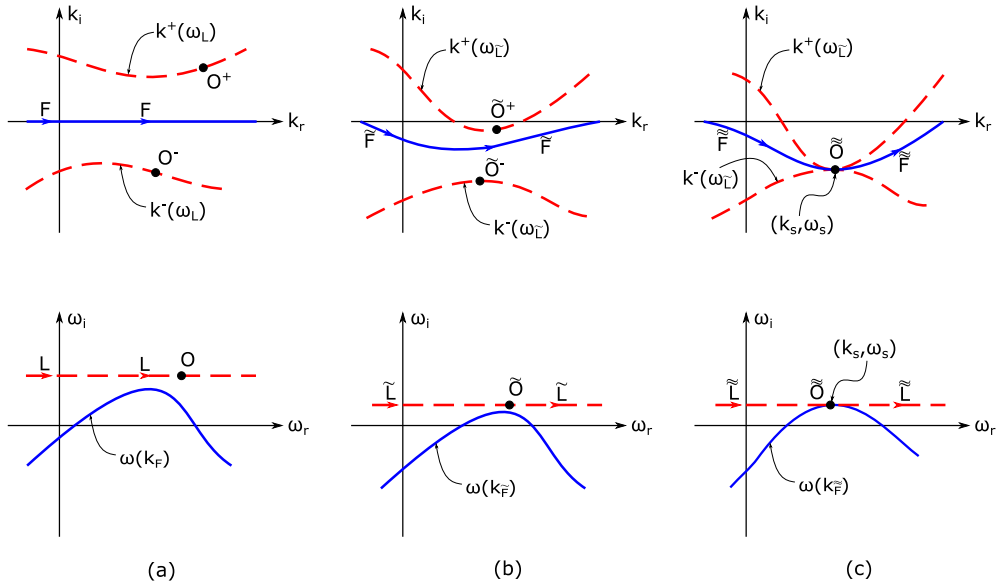

Figure 2.4: Deformation of the F-contour to $\widetilde{F}$ and $\widetilde{\widetilde{F}}$ with corresponding lowering of the L-contour to $\widetilde{L}$ and $\widetilde{\widetilde{L}}$. Causality is satisfied across the deformations and the map of $\widetilde{\widetilde{L}}$ in complex k-plane pinches $\widetilde{\widetilde{L}}$ at the saddle point k_s with corresponding branch point ω_s in the ω-plane. (Bers [2])

The criterion is discussed in detail and time-asymptotic response has been calculated in Appendix A. The response is given as the Green's function

$$\lim_{t\to\infty} |\mathcal{G}(x,t)| \sim \frac{\exp[\mathrm{i}(k_\mathrm{s}x-\omega_\mathrm{s}t)]}{\left[2\pi\mathrm{i}\left(\frac{\partial\mathcal{D}}{\partial\omega}\right)\left(\frac{\partial^2\mathcal{D}}{\partial k^2}\right)\right]_\mathrm{s}^{1/2} t^{1/2}}\,. \tag{2.32}$$

The response is equivalent to the one represented in Eq. 2.27. If the branch point at $\omega = \omega_\mathrm{s}$ has $\mathrm{Im}(\omega_\mathrm{s}) > 0$, the time-asymptotic response grows in time at all locations x, resulting in *absolute* instability.

The absolute instability can also be examined by tracking the pinch point $\widetilde{\widetilde{O}}$ from the initial *unpinched* position (O^+ and O^-). In Fig. 2.4(a), $\omega(O)$ on L is placed above the highest $\omega(k_F)$ branch, *i.e.*, the temporal growth of the source is sufficiently high, which ensures that *causality* is satisfied and therefore the localised response given by O^+ and O^- decays in space for $x > 0$ and $x < 0$ respectively. As $k_\mathrm{r}^+(\omega_L) \neq k_\mathrm{r}^-(\omega_L)$, the spatial response at $x = 0$ is discontinuous which is corrected by a source. In Fig. 2.4(b), as the L contour is lowered to $\widetilde{L}$, the response given by $\widetilde{O}^+$ exhibits spatial growth for $x > 0$ as the temporal growth of the source at $\widetilde{O}$ is less than the highest value of $\omega(k_F)$ at O. The response remains decaying for $x < 0$ and discontinuous at $x = 0$. Finally, in Fig. 2.4(c), the spatial growth for both $x < 0$ and $x > 0$ coincide and the non-attributed source at $x = 0$ is removed. The oscillations become self-sustained and therefore the response $\widetilde{\widetilde{O}}$ appears as a *normal mode* of the medium. The pinch point $\widetilde{\widetilde{O}}$ with the maximum value of ω_i dominates the asymptotic response. Therefore, for absolute instability, we have the temporally amplifying normal mode if $\mathrm{Im}(\omega_\mathrm{s}) > 0$.

2.3.2 Convective instability

In some cases, a part of the map of F-contour in the complex ω-plane ($\omega(k_\mathrm{r})$) may have $\omega_\mathrm{i}(k_\mathrm{r}) > 0$, but without any singularity in $I(x,\omega)$ (Eq. 2.30) in the upper half ω-plane. This allows the lowering of the L-contour to at least $\widetilde{L}$-contour, coincident with the real ω-axis as shown in Fig. 2.5. The F-contour is simultaneously deformed to $\widetilde{F}$-contour. The asymptotic response from Eq. 2.30 can then be expressed as

$$\lim_{t\to\infty} \mathcal{G}(x,t) = \lim_{t\to\infty} \int_{\widetilde{L}} \frac{\mathrm{d}\omega_\mathrm{r}}{2\pi} \exp\left(-\mathrm{i}\omega_\mathrm{r}t\right) I(x,\omega_\mathrm{r}) = 0\,. \tag{2.33}$$

Therefore, as the response at a given location decays to the unperturbed state, absolute instability is absent. However, as a part of $\omega(k_F)$ branch has $\omega_\mathrm{i} > 0$, some part of $k(\omega_{\widetilde{L}})$ branch crosses the real k-axis as the L-contour is deformed to $\widetilde{L}$ as shown in Fig. 2.5. The part of $k^+(\omega_\mathrm{r})$ ($k^-(\omega_\mathrm{r})$) branch which has $k_\mathrm{i} < 0$ ($k_\mathrm{i} > 0$) indicates spatially growing waves for $x > 0$ ($x < 0$). This response is characteristic to *convective* instability.

The convective nature of the instability can be obtained from the Lagrangian formulation of the Green's function. For the case shown in Fig. 2.5, where the spatially growing wave is observed

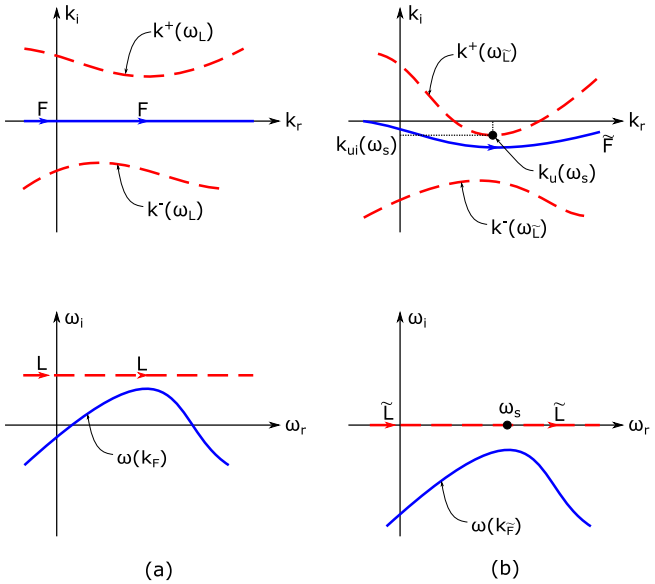

Figure 2.5: Deformation of the F-contour to $\widetilde{F}$ with corresponding lowering of the L-contour to $\widetilde{L}$ when absolute instability is absent. $k_{ui}(\omega_s)$ is the maximum spatial growth rate associated with the asymptotic response for a observer moving with velocity V_s. (Bers [2])

for $x > 0$, we consider $x = Vt > 0$, where V is the speed of the observer. Thus, substituting the expression for $I^+(x,\omega)$ (as the k^- branch is stable) from Eq. A.5 into Eq. 2.33, we get

$$\lim_{t\to\infty} \mathcal{G}(Vt,t) = \lim_{t\to\infty} \int_{-\infty}^{\infty} \frac{\mathrm{d}\omega_\mathrm{r}}{2\pi} \sum_{k^+} \frac{\mathrm{i}H(Vt)}{(\partial\mathcal{D}/\partial k)_{k^+}} \exp\left[-\mathrm{i}\left(\omega_\mathrm{r} - Vk^+(\omega_\mathrm{r})\right)t\right] . \tag{2.34}$$

As no singularity of $I(x,\omega)$ exists on the ω_r-axis, the integrand is analytic and the response is free from absolute instability. The time-asymptotic response is obtained at the saddle point which is given by

$$\begin{aligned} &\frac{\partial}{\partial\omega_\mathrm{r}}\left[\omega_\mathrm{r} - Vk^+(\omega_\mathrm{r})\right] = 0 \\ \Rightarrow \qquad &1 - V\frac{\partial k_\mathrm{r}^+}{\partial\omega_\mathrm{r}} - \mathrm{i}V\frac{\partial k_\mathrm{i}^+}{\partial\omega_\mathrm{r}} = 0\,. \end{aligned}$$

The saddle point is obtained by considering the real and imaginary parts of the relation individually. From the imaginary part,

$$\frac{\partial k_\mathrm{i}^+}{\partial\omega_\mathrm{r}} = 0\,, \tag{2.35}$$

we get the location of saddle point at $\omega_\mathrm{r} = \omega_\mathrm{s}$ when the observer velocity is obtained from the real part as

$$V = V_\mathrm{s} = \left(\frac{\partial k_\mathrm{r}^+}{\partial\omega_\mathrm{r}}\right)^{-1}_{\omega_\mathrm{s}} . \tag{2.36}$$

From Eq. 2.36, we have $\omega_s = V_s k_r^+(\omega_s)$. Thus, in Eq. 2.34, for $\omega_r = \omega_s$ and $k^+ = k_r^+ + \mathrm{i}k_i^+$, we have $\left[\omega_s - V_s k_r^+(\omega_s) - \mathrm{i}V_s k_i^+(\omega_s)\right] = V_s k_i^+(\omega_s)$. Thus, The asymptotic response is given as

$$\lim_{t\to\infty} \mathcal{G}(t) \sim t^{-1/2} \exp\left[-V_s k_r^+(\omega_s) t\right] . \tag{2.37}$$

The Eq. 2.34 gives the evolution of the convective instability. The Eq. 2.37 gives the maximum spatial amplification ($k_i^+(\omega_s)$) of the signal around $\omega = \omega_s$, travelling at speed $V = V_s$. If the convectively unstable modes appear for both $z > 0$ and $z < 0$, in the same frequency range, the system is inherently absolutely unstable.

2.4 Global analysis

The complete three-dimensional impulse response of the base flow to the perturbations can be calculated from the global analysis. These analyses are usually computationally expensive and require parallelised numerical schemes. The global analyses are classified as *linear* or *nonlinear* valid for specific classes of developing flows.

The *linear* global analysis is valid for flows that exhibit slow temporal and spatial growth. The near-transition physics of the self-sustained global structures can be obtained from this analysis. The governing theory for this analysis was developed by Huerre and Monkewitz [12]. The theory is based on WKBJ approximation which allows the analytical continuation of the local analysis in the slowly varying x-direction to the complex x-plane. The linear global modes take the form of the ansatz 1.2. The medium can allow self-sustained oscillations if the global modes are unstable.

The *nonlinear* global analysis is used for flows with low spatial growth and high temporal growth. The post-transition physics can obtained from this analysis. The governing theory for this analysis was developed by Pier and Huerre [24].

Both the linear and nonlinear approaches require finite regions of local absolute instability as a necessary but not sufficient condition for global analysis. Therefore, computationally inexpensive local analysis is used to estimate the global stability properties. The local analysis was performed by Lingwood [20] and concluded that the absolute instability triggers the onset of transition in flows.

□

Chapter 3

Numerical implementation for analytical and non-analytical models

3.1 Analytical model

3.1.1 Inviscid theory

The inviscid theory is reviewed in this section. For a parallel two-dimensional flow, the basic steady flow is given as

$$\mathbf{U} = U^{\mathrm{d}}(y^{\mathrm{d}})\widehat{\mathbf{i}}, \quad y_1^{\mathrm{d}} \leq y^{\mathrm{d}} \leq y_2^{\mathrm{d}}\,. \tag{3.1}$$

The superscript 'd' denotes dimensional variable.

The governing equations can be given in dimensionless form with respect to the reference quantities: reference velocity (U_{ref}), reference density (ρ_{ref}) and reference length (L_{ref}). The average of maximum and minimum velocities in co-flow, counter-flow jets/wakes gives U_{ref} as

$$U_{\mathrm{ref}} = \frac{U_{\mathrm{max}} + U_{\mathrm{min}}}{2}\,. \tag{3.2}$$

Similarly, the reference density is given by the average density such that no special preference is given to either of the layers. Thus,

$$\rho_{\mathrm{ref}} = \frac{\rho_{\mathrm{max}} + \rho_{\mathrm{min}}}{2}\,. \tag{3.3}$$

For confined flows $y^{\mathrm{d}} \in [y_1^{\mathrm{d}}, y_2^{\mathrm{d}}]$, the reference length is given as,

$$L_{\mathrm{ref}} = \frac{y_1^{\mathrm{d}} + y_2^{\mathrm{d}}}{2}\,. \tag{3.4}$$

For unconfined flows, Eq. 3.4 is not valid and a more relevant reference length scale is used, as suggested by Juniper [17] for instance, shear width or ratio of surface tension to dynamic pressure

$(\sigma/\rho_{\text{ref}}U_{\text{ref}}^2)$. Using the reference scales given by Eq. 3.2-3.4, the non-dimensional form of the flow variables is given as

$$t = \frac{t^{\text{d}}U_{\text{ref}}}{L_{\text{ref}}}, \quad \mathbf{x} = \frac{\mathbf{x}^{\text{d}}}{L_{\text{ref}}}, \quad \mathbf{u} = \frac{\mathbf{u}^{\text{d}}}{U_{\text{ref}}}, \quad p = \frac{p^{\text{d}}}{\rho_{\text{ref}}U_{\text{ref}}^2}, \quad \rho = \frac{\rho^{\text{d}}}{\rho_{\text{ref}}}\,. \tag{3.5}$$

Using this information and applying the inviscid assumption along to the Euler equation and the continuity equation, the Rayleigh's equation has been derived in Appendix B, which is rewritten here

$$\rho\left[(U-c)(\phi'' - k^2\phi) - U''\phi\right] = 0\,, \tag{3.6}$$

along with the boundary condition

$$k\phi = 0 \quad \text{at} \quad y = y_1, y_2\,. \tag{3.7}$$

where the right-quote $'$ represents differentiation with respect to y and $\phi = \phi(y)$ is the perturbation stream function amplitude given by Eq. B.14.

3.1.2 Linear profile approximation of flows

The flows that are studied in this thesis using the analytical treatment have piecewise linear velocity profiles and piecewise constant density profiles, *i.e.*, $U''(y) = 0$ and $p'(y) = 0$ respectively. The Rayleigh's equation simplifies to

$$\rho(U-c)(\phi'' - k^2\phi) = 0\,. \tag{3.8}$$

For the discrete spectrum with $U \neq c$, the equation is simplified as

$$\phi'' - k^2\phi = 0\,. \tag{3.9}$$

The eigenfunction is obtained as a solution of this ODE which is given as

$$\phi = A\mathrm{e}^{-\xi y} + B\mathrm{e}^{\xi y}\,, \tag{3.10}$$

where $\xi \equiv +\sqrt{k^2}$. The use of linear profile approximation therefore simplifies the Rayleigh's equation in each section of the flow as $U'' = 0$. But it introduces complication at the points where the derivatives become discontinuous. It is therefore necessary to use the matching condition at these locations with discontinuity ($y = y_D$). This will be discussed in the following section.

3.1.2.1 Matching conditions

The matching conditions are based on the condition that the eigenfunctions across the different sections of the flow profile must be equal. The matching conditions have been derived in Appendix B. The *dynamic* matching condition is rewritten as

$$\left[\!\left[\rho(U-c)\phi' - \rho U'\phi\right]\!\right] = 0\,, \tag{3.11}$$

where $[\![\cdot]\!]$ gives the *jump* in a quantity. Also, the *kinematic* matching condition is given as

$$\left[\!\left[\frac{\rho\phi}{(U-c)}\right]\!\right] = 0\,. \tag{3.12}$$

For continuous U profile, this condition corresponds to the requirement of the normal velocity of the fluid to be continuous across the discontinuity.

The two matching conditions and the Rayleigh's equation 3.9 along with the boundary condition 3.7 are used to determine the coefficients of the fundamental solutions 3.10. This results in an expression of c as a function of k, or in other words, the dispersion relation.

3.1.2.2 Boundary conditions

The fundamental solution given by Eq. 3.10 must satisfy the boundary conditions imposed on the governing equation. For this reason, the eigenfunctions must be invariant under the transformation $\xi \to -\xi$. The confined and unconfined flow cases will be discussed in the following sections.

Confined flows

Confined flows comprise of bounding walls at $y_1 = -1$ and $y_2 = +1$ where the zero normal velocity is imposed. The solution given by Eq. 3.10 is applicable to the upper $(+)$ and lower $(-)$ regions individually. The complete solution is a linear combination of both eigenfunctions

$$\begin{aligned} \phi_+ &= A_+ \mathrm{e}^{-\xi(y-1)} + B_+ \mathrm{e}^{+\xi(y-1)} \,, \\ \phi_- &= A_- \mathrm{e}^{-\xi(y+1)} + B_- \mathrm{e}^{+\xi(y+1)} \,. \end{aligned} \tag{3.13}$$

From Eq. B.15, it is observed that for $v = 0$, we should have $\phi = 0$ at $y = \pm 1$. From Eq. 3.13, this condition is satisfied for $A + B = 0$. Imposing the transformation $\xi \to -\xi$, we get

$$\begin{aligned} \phi_+ &= A_+ \mathrm{e}^{+\xi(y-1)} + B_+ \mathrm{e}^{-\xi(y-1)} \,, \\ \phi_- &= A_- \mathrm{e}^{+\xi(y+1)} + B_- \mathrm{e}^{-\xi(y+1)} \,. \end{aligned} \tag{3.14}$$

The eigenfunction will satisfy the boundary condition again when $A + B = 0$. Therefore, for confined flow, the solution is invariant in the transformation $\xi \to -\xi$ and it is sufficient to consider $\xi = +\sqrt{k^2}$.

Unconfined flows

the unconfined flow cases, the zero normal velocity condition is imposed at $y_1 = -\infty$ and $y_2 = +\infty$. As the regions extend to infinity, only the spatially decaying component of the eigenfunction in each of the upper and lower regions forms the solution. For $\mathrm{Re}(k) > 0$, the eigenfunctions are given as

$$\begin{aligned} \phi_+ &= A_+ \mathrm{e}^{-\xi y} \,, \\ \phi_- &= B_- \mathrm{e}^{+\xi y} \,. \end{aligned} \tag{3.15}$$

Satisfying the boundary condition at $y = \pm\infty$ gives $B = 0$. Imposing the transformation $\xi \to -\xi$, we get

$$\begin{aligned} \phi_+ &= B_+ \mathrm{e}^{-\xi y} \,, \\ \phi_- &= A_- \mathrm{e}^{+\xi y} \,. \end{aligned} \tag{3.16}$$

Satisfying the boundary condition at $y = \pm\infty$ gives $A = 0$. This is inconsistent with the condition obtained before the transformation $\xi \to -\xi$. Therefore. the solution is not invariant. The special

treatment of such flows is discussed by Rees [26]. The transformation $\xi \to -\xi$ is equivalent to the crossing of the branch cut by the saddle point solution. The spatio-temporal analysis is used to follow the saddle point as the parameters are varied. The full impulse response is then used to decide whether the flow is convectively or absolutely unstable.

3.1.2.3 Single shear layer dynamics

The plane shear layer appears downstream of a thin plate, located away from walls, by merger of two parallel streams initially on either sides of the plate; see Fig. 3.1. The shear layer grows along the stream from the initial velocity and/or density discontinuity. The region with velocity-gradient between the two streams is also known as the mixing layer. The shear layer appears in various flows, such as initial parts of jets, and on top of locally separated boundary layers.

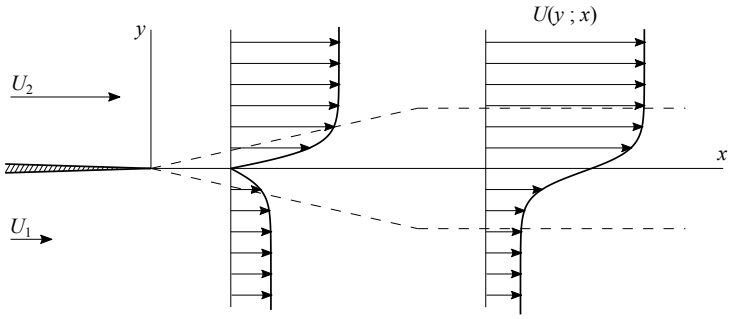

Figure 3.1: Spatially developing mixing layer (Ho and Huerre [10]).

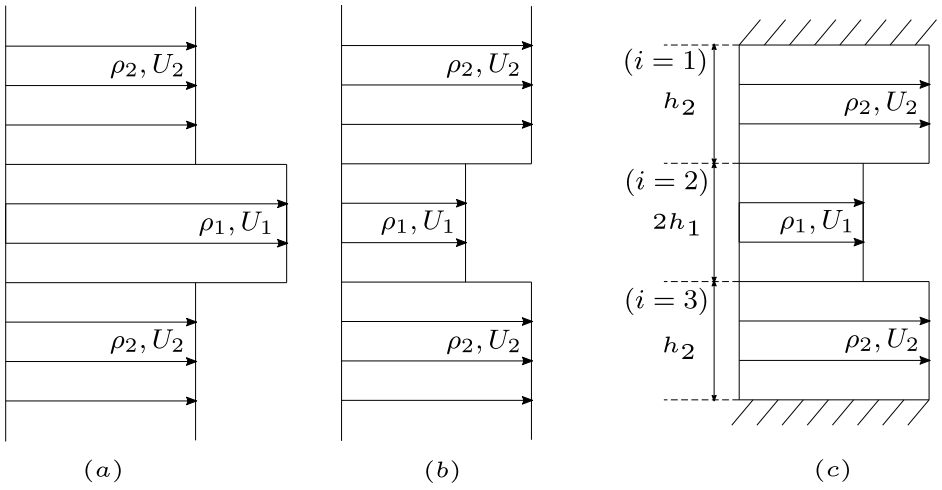

Figure 3.2: Profiles of velocity for the study of absolute instability of inviscid plane (a) jets and (b) wakes by Huerre and Monkewitz [12]. The flow domain is considered infinite in both streamwise and normal directions. The study on (c) confined flows was performed by Juniper [17].

The focus of the thesis is on co-flow jets and wakes. A jet (wake) flow has a local region with higher (lower) velocity than the surroundings. The jets and wakes exhibit oscillations around a specific base flow, *e.g.* von Kármán vortex street in the wake behind a cylinder. Such flow is

considered unstable and it is associated with the flow geometry and characteristic parameters. Confined flow, *i.e.*, flow near walls, appears when the mixing layer forms in a narrow channel. For unconfined flow, the walls are located far from the shear layer; theoretically at $y = \pm\infty$.

The co-flow jets and wakes form when one inner and two outer streams enter the flow-field at different velocities and mix together. The flow is symmetric about the centreline. For jet (wake) flow, out of the two streams, the inner stream has a higher (lower) velocity. In the thesis, the theory of weakly nonparallel flows is used to study the stability of co-flow jets and wakes. According to Huerre and Monkewitz [12], in the weakly nonparallel flows, local streamwise velocity profiles can be used to approximate the frequency, growth rates and shapes of the linear global modes. Then, for a growing mode to exist, the presence of a finite region of local absolute instability is a sufficient requirement. Therefore, the identification of absolute instability in the jet and wake profiles is of great significance.

Huerre and Monkewitz [12] studied the local absolute instability of plane inviscid jets and wakes, with constant velocity and density in the inner and outer streams (Fig. 3.2). It was concluded that the absolute instability enhances with the degree of shear, given by the velocity difference. In the jet, the varicose mode (symmetric for streamwise velocity, antisymmetric for normal velocity) always become unstable before the sinuous mode (antisymmetric for streamwise velocity, symmetric for normal velocity). For the wake, it is the sinuous mode that becomes unstable first (Fig. 3.3).

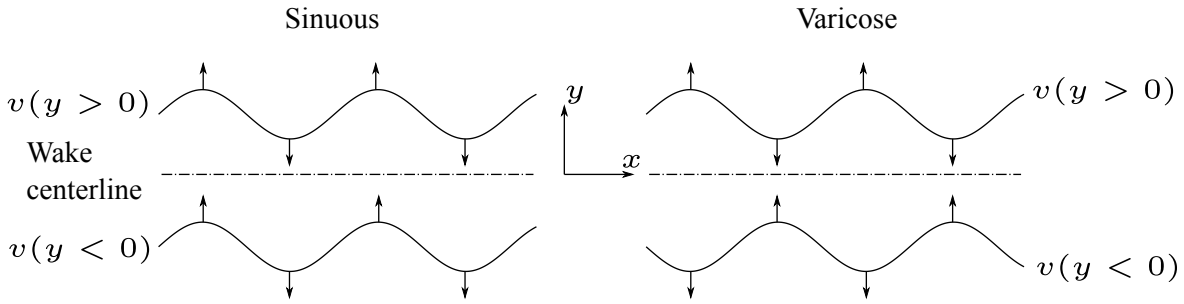

Figure 3.3: Sinuous and varicose modes defined in terms of vertical perturbation velocity.

The co-flow jets and wakes as shown in Fig. 3.3 can be considered as a combination of two shear layers which interact with each other as sinuous or varicose modes or with their image system in the wall as varicose modes. The study of the dynamics of a single shear layer offers insight into the interaction when a second shear layer or wall is introduced.

3.1.2.4 Multiple shear layer dynamics

As discussed in § 3.1.2.3, the single shear layer dynamics can be expanded to jet and wake flows by including a second shear layer and, if needed, a confining wall. The confined double vortex sheet and double shear layer models will be studied in this chapter. The models used here are discussed by Juniper [17] and Juniper [14] respectively.

As shown in Fig. 3.3, the shear layers interactions can be categorised as sinuous or varicose motions. As the governing equations given in § 3.1.2 are linear, the initial normal mode perturbation can be decomposed into sinuous and varicose modes. Therefore, stability analysis can be performed on each mode individually. The effect of confining wall can be introduced in computation by

considering it as an additional shear layer which is obtained as an image of the physical shear layer by reflecting it in the wall (see Fig. 3.4). For confined flows with two shear layers, the confinement decides the dominance of interaction wither amongst the shear layers or with the image system.

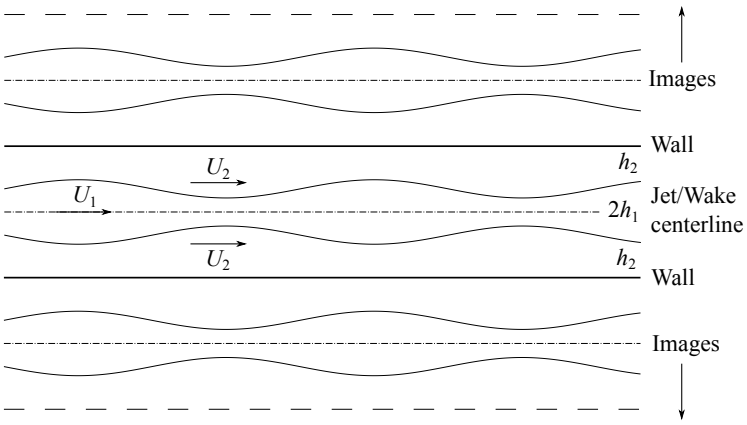

Figure 3.4: Image systems of a confined varicose flow (Juniper [17])

The low order models discussed in this section will be used to develop an understanding of the mechanisms for instability that can be used in design for specific applications. By establishing the parameters that affect the instability, the flow can be controlled for a specific spatio-temporal behaviour.

3.2 Non-analytical model

The analytical models described above sacrifice the C^1-continuity of the flow profiles which enables to derive and study the dispersion relations analytically. To study the physical base flow profiles, a better approximation is obtained by considering the functions which are at least C^2-continuous. In Chapter 5, three such functions, namely algebraic function, 'tanh' function and error function, are used to study the instability behaviour of a shear flow. The analytical expressions for the dispersion relation cannot be obtained for these cases. Therefore, the flow is implemented and verified using VESTA.

These high order models are capable of reproducing the flows well. The results from these simulations do not tend to drive the design process but can be used to validate proposed alterations of the flow configuration. These calculations can be provide an accurate description of the flow from which the useful information about the dominant frequency spectra can be extracted, but these do not provide any insight into the dominant mechanisms responsible for the instability.

3.3 Methodology

The procedure for numerical implementation of the analytical and non-analytical dispersion relations in order to obtain the convective/absolute instability transition boundary are discussed in this section. The block diagram of the solution scheme is shown in Fig. 3.5.

3.3.1 Saddle point calculation

The saddle point calculation forms the basis of the application of the Briggs-Bers criterion to identify whether the flow is convectively or absolutely unstable. To begin with the calculation, the Riemann sheet is first plotted in the complex k-space. The Riemann sheet is the complex ω solution to the dispersion relation $\mathcal{D}(k,\omega) = 0$. The saddle point is a point on the Riemann sheet that satisfies the additional criteria

$$\frac{\partial \mathcal{D}}{\partial k}(k,\omega) = 0\,. \tag{3.17}$$

The value of the saddle point $(k_\mathrm{s}, \omega_\mathrm{s})$ is calculated from a user selected initial guess (k_0, ω_0) on the Riemann sheet which lies near the expected location of the saddle point. The exact value of the saddle point is calculated iteratively using MATLAB's `fsolve` routine.

3.3.2 Pinch point identification

The saddle points that form valid k^+/k^- pinching are identified as the presence of such saddle points indicates that the flow is absolutely unstable. These pinch points lie on the integration contour that is obtained as a path of steepest descent.

The pinch points are also easily identified from the Riemann sheet with the contour plots of ω_i (or ω_r) in the complex k-space where two hills meet with adjacent valleys on either side, with one hill extending to the $k_\mathrm{i} > 0$ plane and the other hill extending to the $k_\mathrm{i} < 0$ plane.

3.3.3 Numerical method for solving general eigenvalue problem

To solve the Rayleigh's equations for the inviscid flows, the linear stability analysis tools provided by the VKI Extensible Stability and Transition Analysis (VESTA) toolkit has been used. The toolkit provides all the necessary functions required to perform the stability analysis on a specific base flow, see Pinna [25]. However, to include the capability to verify the criteria for the convective/absolute instability transition, the tools developed for the analysis in the previous chapters are integrated with VESTA.

The numerical approach is accomplished with the compressible linear stability solvers in VESTA. A short summary of the solver implementation and validation will be discussed here. For a more comprehensive study, the reader is referred to Pinna [25].

The VESTA toolkit employs the Chebyshev collocation method for the solution in the computational domain. The Chebyshev collocation method offers flexibility in terms of application to numerous base flow profiles. The resulting eigenvalue problem is solved using QZ algorithm. The global solver calculates the whole spectrum of eigenmodes at once. A convergence study was performed to reproduce the results in Table 2.2 of Pinna [25] to understand the solver before applying the tool to the shear flow.

□

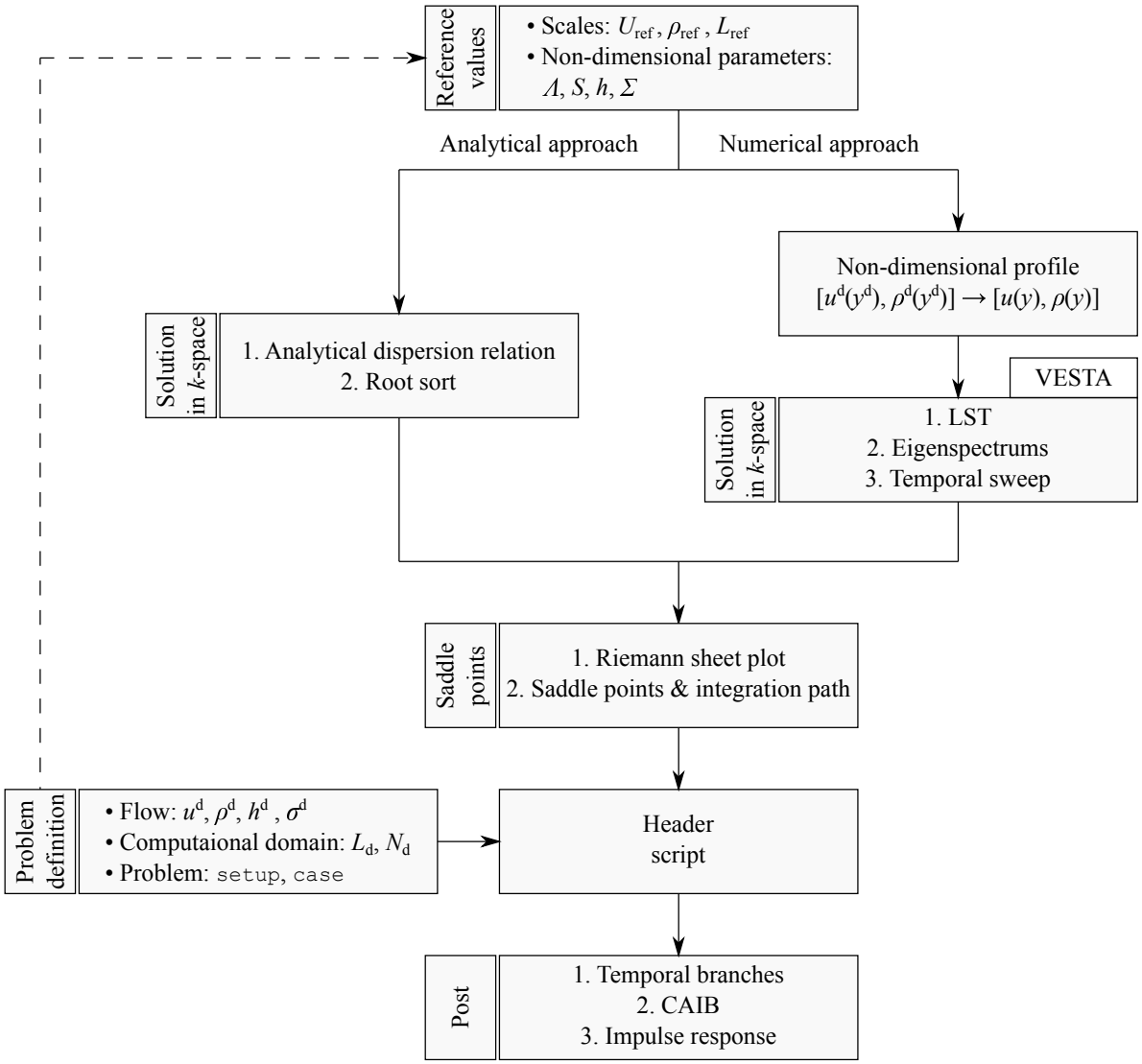

Figure 3.5: Block diagram of the solution scheme for spatio-temporal analysis of a base flow using analytical or numerical approach.

Chapter 4

Analytical models

In this chapter, the piecewise linear approximations to the plane shear layers will be studied with varying complexities.

4.1 Inviscid planar single shear layer

4.1.1 Unconfined single vortex sheet

As shown in Fig. 3.3, the single shear layer can be approximated as a vortex sheet formed between two inviscid, irrotational, and incompressible flows with a finite surface tension at the interface. Both streams are semi-infinite in the normal direction, infinite in streamwise direction and uniform in the spanwise direction.

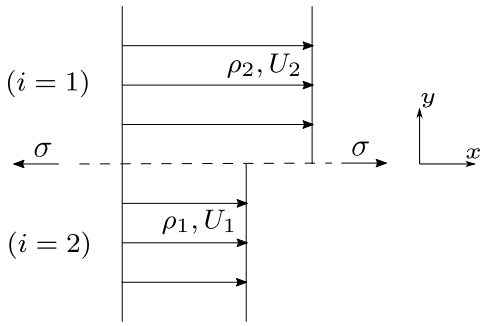

Figure 4.1: The vortex sheet is formed at the interface of two co-flowing or counter-flowing streams, each with a constant density and velocity, and a nonzero surface tension at the interface.

Surface tension was first introduced by Juniper [17] to make the stability problem suitable for Briggs-Bers analysis. In the limit $\sigma \to 0$, the effect of other flow parameters, like confinement, on the stability of the flow can be studied.

From Eq. B.14, the perturbation streamfunction for each stream ($i = 1, 2$) is given as

$$\psi_i(x, y, t) = \phi_i(y)\mathrm{e}^{\mathrm{i}(kx-\omega t)}\,, \tag{4.1}$$

and from Eq. 3.9, the governing equation for the each eigenfunction can be written as

$$\phi_i'' - \xi_\pm^2\phi_i = 0\,, \tag{4.2}$$

where $\xi_\pm = \pm\sqrt{k^2}$. The eigenfunction obtained from the governing equation satisfies the boundary condition given by Eq. 3.7 and the matching conditions in § 3.1.2.1.

4.1.1.1 Dispersion relation

The eigenfunctions for streams $i = 1$ and $i = 2$ are given as

$$\begin{aligned} \phi_1 &= A\mathrm{e}^{-\xi^{\mathrm{d}}y^{\mathrm{d}}}\,, \\ \phi_2 &= B\mathrm{e}^{+\xi^{\mathrm{d}}y^{\mathrm{d}}}\,, \end{aligned} \tag{4.3}$$

where, the superscript 'd' represents dimensional quantities. The solution in this form ensures that the condition $\phi_i = 0$ is satisfied at the boundaries $y^{\mathrm{d}} = \pm\infty$. The dimensional form of the kinematic matching condition at the interface gives

$$\begin{aligned} &\left[\!\left[\frac{\phi_i}{(U_i - c^{\mathrm{d}})}\right]\!\right] = 0 \\ \Rightarrow \qquad &\frac{A}{(U_2 - c^{\mathrm{d}})} = \frac{B}{(U_1 - c^{\mathrm{d}})}\,. \end{aligned} \tag{4.4}$$

The dimensional form of dynamic matching condition at the interface gives

$$\left[\!\left[\rho_i(U_i - c^{\mathrm{d}})\phi_i' - \rho_i U_i'\phi_i\right]\!\right]\mathrm{e}^{\mathrm{i}(k^{\mathrm{d}}x^{\mathrm{d}}-\omega^{\mathrm{d}}t^{\mathrm{d}})} = \Delta p^{\mathrm{d}}\,. \tag{4.5}$$

where Δp^{d} is the pressure jump as a result of the surface tension at the interface. Rees [26] gives a solution of pressure jump by calculating the pressure jump across the perturbed interface in terms of either of the eigenfunction amplitudes A or B. This is derived in Appendix B. Without loss of generality, for $i = 1$, the pressure jump Δp^{d} is given as

$$\Delta p^{\mathrm{d}} = -A\frac{\sigma(k^{\mathrm{d}})^2}{(U_2 - c^{\mathrm{d}})}\mathrm{e}^{\mathrm{i}(k^{\mathrm{d}}x^{\mathrm{d}}-\omega^{\mathrm{d}}t^{\mathrm{d}})}\,. \tag{4.6}$$

Inserting this expression of Δp^{d} in the RHS and substituting eigenfunctions for the stream $i = 1, 2$ in the LHS of Eq. 4.5, we get

$$-A\rho_2(U_2 - c^{\mathrm{d}})\xi^{\mathrm{d}} - B\rho_1(U_1 - c^{\mathrm{d}})\xi^{\mathrm{d}} = -A\frac{\sigma(k^{\mathrm{d}})^2}{(U_2 - c^{\mathrm{d}})}\,. \tag{4.7}$$

Now, as both the kinematic and dynamic matching conditions have been derived, we can now formulate the dispersion relation. The coefficients of the eigenfunction amplitudes A, B can be collected from the matching conditions given by Eq. 4.4 and Eq. 4.7 to give

$$\begin{bmatrix} (U_1 - c^{\mathrm{d}}) & -(U_2 - c^{\mathrm{d}}) \\ \rho_2(U_2 - c^{\mathrm{d}}) - \sigma\xi^{\mathrm{d}}/(U_2 - c^{\mathrm{d}}) & \rho_1(U_1 - c^{\mathrm{d}}) \end{bmatrix}\begin{bmatrix} A \\ B \end{bmatrix} = 0\,. \tag{4.8}$$

For non-trivial cases, the determinant of the coefficient matrix must be zero. This gives the dimensional dispersion relation as

$$\mathcal{D}^{\mathrm{d}}(k^{\mathrm{d}},\omega^{\mathrm{d}}) = \rho_1(U_1 - c^{\mathrm{d}})^2 + \rho_2(U_2 - c^{\mathrm{d}})^2 - \sigma\xi^{\mathrm{d}} = 0\,. \tag{4.9}$$

The dispersion relation can be transformed to non-dimensional form by using the reference scales for velocity, density and length as

$$U_{\mathrm{ref}} = \frac{U_1 + U_2}{2}, \quad \rho_{\mathrm{ref}} = \frac{\rho_1 + \rho_2}{2}, \quad L_{\mathrm{ref}} = \frac{\sigma}{2\rho_{\mathrm{ref}}U_{\mathrm{ref}}^2}\,. \tag{4.10}$$

The dimensionless variables can be then derived from the dimensional counterparts using these reference scales.

$$c = \frac{c^{\mathrm{d}}}{U_{\mathrm{ref}}}, \quad k = k^{\mathrm{d}}L_{\mathrm{ref}}, \quad \xi = \xi^{\mathrm{d}}L_{\mathrm{ref}}, \quad \omega = \frac{\omega^{\mathrm{d}}L_{\mathrm{ref}}}{U_{\mathrm{ref}}}\,. \tag{4.11}$$

The dimensionless parameters are also given as

$$\Lambda = \frac{U_1 - U_2}{U_1 + U_2}, \quad S = \frac{\rho_1 - \rho_2}{\rho_1 + \rho_2}\,. \tag{4.12}$$

Using the above quantities, the dimensionless dispersion relation is given as

$$\mathcal{D}(k,\omega) = (1+S)(1+\Lambda-c)^2 + (1-S)(1-\Lambda-c)^2 - 2\xi = 0\,. \tag{4.13}$$

4.1.1.2 Stability analysis

The benefit of considering piecewise linear profile for the shear layer can be easily seen now. The dispersion relation given by Eq. 4.13 can be easily solved analytically. As explained in § 2.3, the dispersion relation can be used to obtain the saddle point, which is required to identify the convective/absolute nature of the instability.

The condition for saddle point given by Eq. 2.31 requires that apart from satisfying the condition $\mathcal{D} = 0$ given by Eq. 4.13, the saddle point must also satisfy

$$\begin{aligned} &\frac{\partial \mathcal{D}}{\partial k} = 0 \\ \Rightarrow \qquad &(1+S)(1+\Lambda-c)c + (1-S)(1-\Lambda-c)c - \xi = 0\,. \end{aligned} \tag{4.14}$$

To solve for the saddle point, first the complex k-space is defined and the solution $\omega = ck$ is obtained from the dispersion relation given by Eq. 4.13. Then MATLAB's `fsolve` routine is used to solve Eq. 4.14 arrive at the saddle point iteratively.

Temporal stability analysis

For the temporal stability analysis, Eq. 4.13 is solved to obtain the value of complex ω for real values of k. The solutions for $\omega = ck$ are obtained analytically as the roots of the dispersion relation.

$$\omega = \xi\left[1 + \Lambda S \pm \mathrm{i}\sqrt{\Lambda^2(1-S^2) - \xi}\right]\,. \tag{4.15}$$

It is inferred that temporal instability, given by $\omega_\mathrm{i} > 0$ for $k \in \mathbb{R}$, exists for the wavenumber values in the range $0 < k < \Lambda^2(1 - S^2)$. Therefore, the flows with small density variations ($|S| \ll 1$) exhibit temporal instability for higher value of wavenumber than that for the flows with large density difference ($S \simeq \pm 1$).

The maximum temporal growth rate $\omega_{i,\max}$ can be calculated from Eq. 4.15 from the condition $\partial\omega_\mathrm{i}/\partial k = 0$. The value of k_max is then obtained as

$$k_\mathrm{max} = \frac{2}{3}\Lambda^2(1 - S^2)\,, \tag{4.16}$$

for which the value of maximum temporal growth rate is obtained as

$$\omega_{i,\max} = +k_\mathrm{max}\sqrt{\frac{\Lambda^2}{3}(1 - S^2)}\,. \tag{4.17}$$

The temporal growth rate plot with surface tension ($\sigma = 1$) and without surface tension ($\sigma = 0$) is shown in Fig. 4.2. For non-zero surface tension, it is observed that the vortex sheet is stable ($\omega_\mathrm{i} < 0$) for $k < 0$ and becomes neutrally stable ($\omega_\mathrm{i} = 0$) at $k_\sigma = \Lambda^2(1 - S^2) = 1$. The range of unstable dimensional wavenumbers is inversely related to the surface tension σ. On the other hand, for zero surface tension, the flow is temporally unstable for all values of $k_\mathrm{r} > 0$. The maximum growth rate for the given parameter values is $\omega_\mathrm{i} = 0.6667$ at $k_\mathrm{r} = 0.3849$.

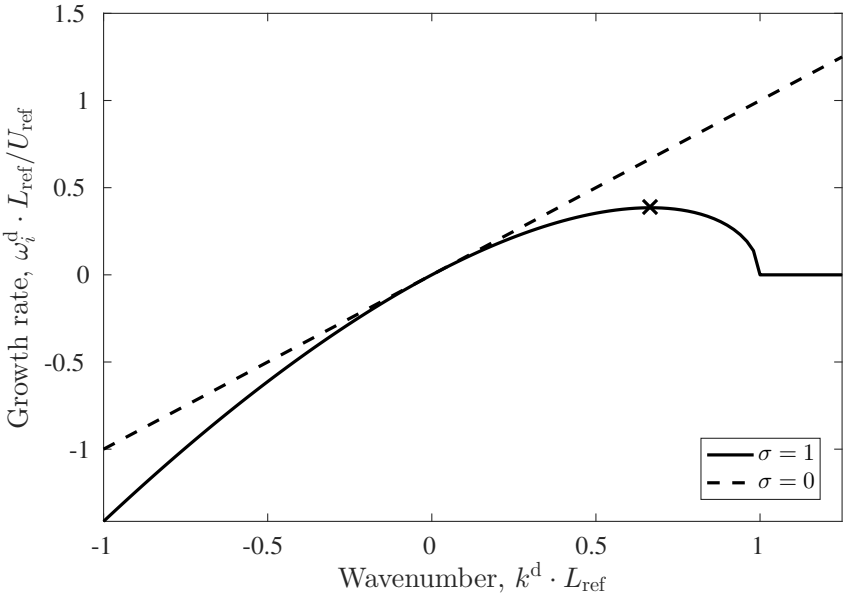

Figure 4.2: Temporal growth rate for the parameter $(\Lambda, S) = (1, 0)$ for single vortex sheet with and without surface tension. The $\times$ indicates the temporal mode with the highest growth rate.

Spatio-temporal stability analysis

The dispersion relation $\mathcal{D}(k, \omega; R) = 0$ has four unknowns as $k_\mathrm{i}, k_\mathrm{r}, \omega_\mathrm{i}, \omega_\mathrm{r}$ and two constraints $\mathrm{Re}(\mathcal{D}) = 0$ and $\mathrm{Im}(\mathcal{D}) = 0$. Thus, as suggested by Juniper [17], the solution of the dispersion

relation is a two-dimensional manifold in four dimensional space. For the vortex sheet, it is observed from the dispersion relation 4.13 that ω can be explicitly expressed as a function of k as $\omega(k) = f(k) \pm \sqrt{g(k)}$, where both $f(k)$ and $g(k)$ are single-valued functions. The two solutions are mapped conformally to two Riemann surfaces in the k-space. The Riemann surfaces meet at branch points of order 1, locations where $g(k) = 0$. For dispersion relations with two roots, the branch cuts are defined between arbitrarily chosen pairs of branch points.

For the given case, Eq. 4.13 and Eq. 4.14 can be solved analytically to obtain the saddle point location in the complex k-space. The solution is given as

$$\begin{aligned} c_\mathrm{s} &= \frac{1}{3}\left[2(\Lambda S+1) \pm \sqrt{2\Lambda S(2\Lambda S+1) - 3\Lambda^2 + 1}\right], \\ k_\mathrm{s} &= \frac{1}{9}\left[-4\Lambda S(\Lambda S-1) + 6\Lambda^2 + 2 \pm (2\Lambda S+2)\sqrt{2\Lambda S(2\Lambda S+1) - 3\Lambda^2 + 1}\right], \end{aligned} \tag{4.18}$$

which can be used to obtain $\omega_\mathrm{s} = c_\mathrm{s} k_\mathrm{s}$. The ω_i contours for one of the Riemann sheets is plotted in Fig. 4.3 for the homogeneous vortex sheet with parameter $R \equiv (\Lambda, S) = (1, 0)$. The other Riemann surface is mirror image about the k_r-axis and is not shown here. No analytic minima or maxima exists on the surface, therefore, the group velocity $\partial\omega/\partial k$ is zero only at the saddle point(s). As the mapping is conformal, the ω_i and ω_r contours are orthogonal except at the branch points and poles of the dispersion relation. Therefore, if $\partial\omega_\mathrm{i}/\partial k = 0$ at an analytical point on the Riemann surface, the point must be a saddle point and also $\partial\omega_\mathrm{r}/\partial k = 0$. The plot of contours of ω_i therefore gives all the saddle points corresponding to the wavenumbers with zero group velocity. The saddle point value for the given parameter set which also satisfies the pinching condition is $(k_\mathrm{s}, \omega_\mathrm{s}) = (0.8890 - 0.3143\mathrm{i}, 0.7407 + 0.2095\mathrm{i})$.

The eigenfunction corresponding to the saddle point is plotted in Fig. 4.4. The eigenfunction is discontinuous at $y = 0$ and decays exponentially to $\phi = 0$ as $y \to \pm\infty$. Mathematically, the discontinuity appears because $B = A(1 - \Lambda - c)/(1 + \Lambda - c) \Rightarrow B < A$ and from Eq. 4.3, the eigenfunctions have the peak defined by coefficients A and B at $y = 0$.

4.1.2 Unconfined single shear layer

The unconfined single shear layer is approximated by a piecewise linear profile as shown in Fig. 4.5. A shear layer ($i = 2$) forms between two streams ($i = 1, 3$) of uniform velocity. The thickness of shear layer is equal to the vorticity thickness[1], $2d = \delta_\mathrm{v}$. The flow is again considered inviscid and incompressible. The shear layer has a linear velocity profile. However, for density in the shear layer, it is assumed that the upper and lower streams are well mixed with a constant mean density of $\rho_\mathrm{ref} = (\rho_1 + \rho_2)/2$.

[1]The vorticity thickness δ_v is calculated as

$$\delta_\mathrm{v} = \frac{\Delta U}{\left.\dfrac{\mathrm{d}U(y)}{\mathrm{d}y}\right|_\mathrm{max}}, \qquad \text{where} \quad \Delta U = U_2 - U_1.$$

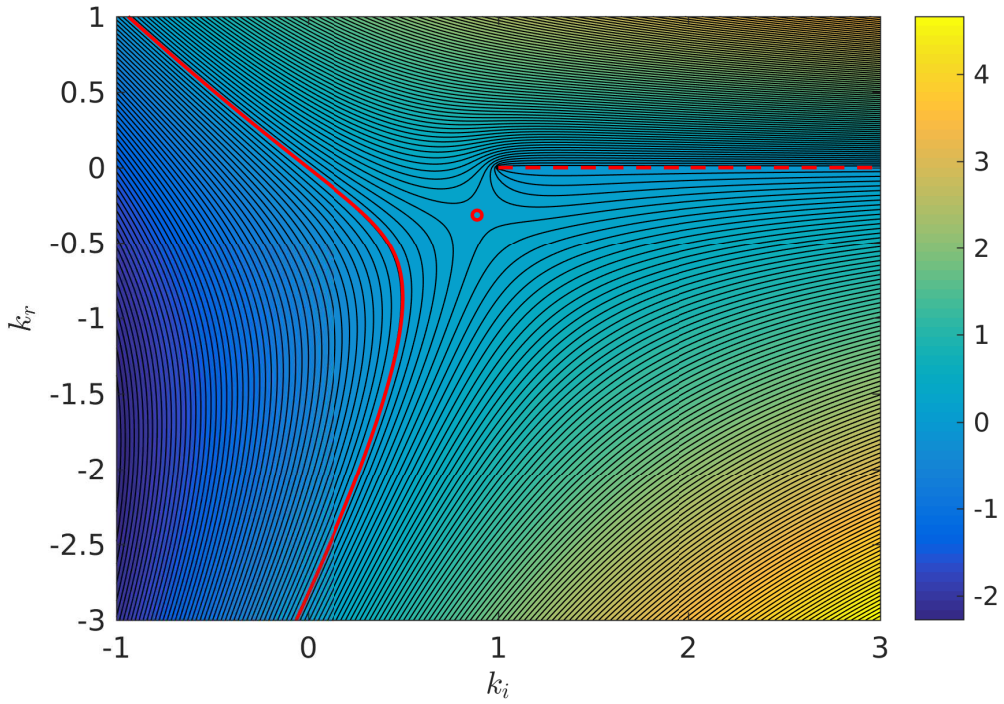

Figure 4.3: Solution to the dispersion relation $\mathcal{D}(k,\omega) = 0$ for unconfined single vortex sheet for the parameter $(\Lambda, S) = (1, 0)$ with non-zero surface tension. The solution is represented by the contours of ω_i in the complex k-plane. The contours of ω_r (not shown) will be orthogonal to these contours. The saddle point (circle) represents modes with zero group velocity as $\partial\omega/\partial k = 0$ at saddle point. The saddle lies on the k^+/k^- pinch point. Additionally, zero temporal growth rate is obtained for modes along the thick solid line, and a branch cut (thick dashed line) is obtained along the real k-axis.

4.1.2.1 Dispersion relation

The eigenfunctions for the streams $i = 1$, $i = 2$ and $i = 3$ is given as

$$\begin{aligned}\phi_1 &= A_1 \mathrm{e}^{-\xi^\mathrm{d}(y^\mathrm{d}-d)}\,,\\ \phi_2 &= A_2 \mathrm{e}^{-\xi^\mathrm{d} y^\mathrm{d}} + B_2 \mathrm{e}^{+\xi^\mathrm{d} y^\mathrm{d}}\,,\\ \phi_3 &= B_3 \mathrm{e}^{+\xi^\mathrm{d}(y^\mathrm{d}+d)}\,.\end{aligned} \tag{4.19}$$

The solution in this form ensures that the condition $\phi = 0$ is satisfied at the boundaries $y^\mathrm{d} = \pm\infty$. The dimensional form of the kinematic matching condition at the interface gives

$$\left[\!\left[\frac{\phi_i}{(U_i - c^\mathrm{d})}\right]\!\right] = 0\,. \tag{4.20}$$

The matching conditions can be applied at the two interfaces. Firstly, at $y^\mathrm{d} = +d$, we have the interface between the streams $i = 1$ and $i = 2$. From Eq. 4.20, we get

$$\begin{aligned}\frac{A_1 \mathrm{e}^{-\xi^\mathrm{d}.0}}{U_2 - c^\mathrm{d}} &= \frac{A_2 \mathrm{e}^{-\xi^\mathrm{d} d} + B_2 \mathrm{e}^{+\xi^\mathrm{d} d}}{U_2 - c^\mathrm{d}}\\ \Rightarrow \qquad A_1 &= A_2 \mathrm{e}^{-\xi^\mathrm{d} d} + B_2 \mathrm{e}^{+\xi^\mathrm{d} d}\,.\end{aligned} \tag{4.21}$$

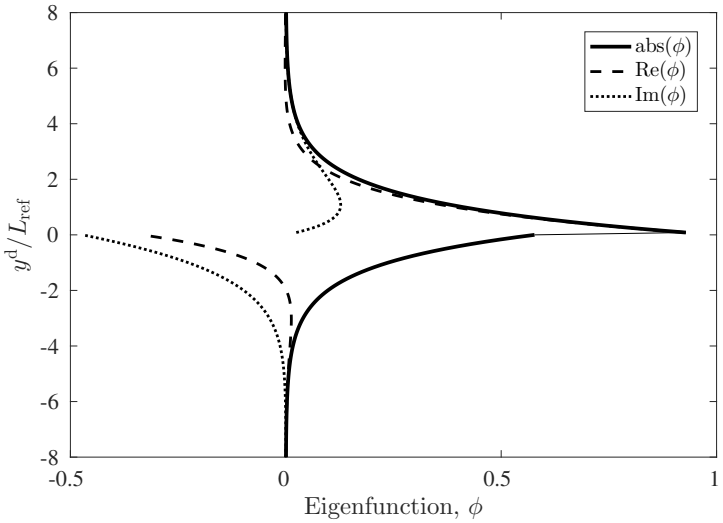

Figure 4.4: Eigenfunction for unconfined single vortex sheet at the saddle point corresponding to the parameter $(\Lambda, S) = (1, 0)$. Note the discontinuity of the eigenfunction at $y = 0$.

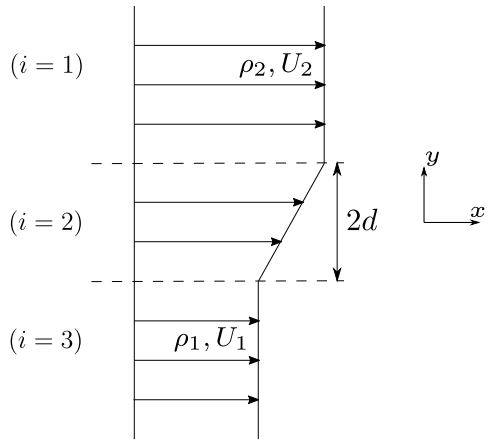

Figure 4.5: The shear layer is formed in a region between two co-flowing or counter-flowing streams, each with a constant density and velocity.

Similarly, at $y^{\mathrm{d}} = -d$, the matching condition gives

$$\begin{aligned} \frac{A_2 \mathrm{e}^{-\xi^{\mathrm{d}}(-d)} + B_2 \mathrm{e}^{+\xi^{\mathrm{d}}(-d)}}{U_1 - c^{\mathrm{d}}} &= \frac{B_3 \mathrm{e}^{+\xi^{\mathrm{d}}.0}}{U_1 - c^{\mathrm{d}}} \\ \Rightarrow \qquad A_2 \mathrm{e}^{+\xi^{\mathrm{d}} d} + B_2 \mathrm{e}^{-\xi^{\mathrm{d}} d} &= B_3 \,. \end{aligned} \tag{4.22}$$

The dimensional form of dynamic matching condition at the interface gives

$$\left[\!\left[\rho_i (U_i - c^{\mathrm{d}}) \phi_i' - \rho_i U_i' \phi_i \right]\!\right] = 0 \,. \tag{4.23}$$

At $y^{\mathrm{d}} = +d$, we get

$$-A_1 \rho_2 (U_2 - c^{\mathrm{d}}) \xi^{\mathrm{d}} = \rho_{\mathrm{ref}} \left[(-A_2 \mathrm{e}^{-\xi^{\mathrm{d}} d} + B_2 \mathrm{e}^{+\xi^{\mathrm{d}} d})(U_2 - c^{\mathrm{d}}) \xi^{\mathrm{d}} - (A_2 \mathrm{e}^{-\xi^{\mathrm{d}} d} + B_2 \mathrm{e}^{+\xi^{\mathrm{d}} d}) \frac{(U_2 - U_1)}{2d} \right] , \tag{4.24}$$

and at $y^{\mathrm{d}} = -d$, we get

$$B_3\rho_1(U_1 - c^{\mathrm{d}})\xi^{\mathrm{d}} = \rho_{\mathrm{ref}}\left[(-A_2\mathrm{e}^{+\xi^{\mathrm{d}}d} + B_2\mathrm{e}^{-\xi^{\mathrm{d}}d})(U_1 - c^{\mathrm{d}})\xi^{\mathrm{d}} - (A_2\mathrm{e}^{+\xi^{\mathrm{d}}d} + B_2\mathrm{e}^{-\xi^{\mathrm{d}}d})\frac{(U_2 - U_1)}{2d}\right]. \tag{4.25}$$

The coefficients of the eigenfunction amplitudes can be collected from the matching conditions to give

$$\begin{bmatrix} 1 & -\mathrm{e}^{-\xi^{\mathrm{d}}d} & -\mathrm{e}^{+\xi^{\mathrm{d}}d} & 0 \\ -2\rho_2 d(U_2 - c^{\mathrm{d}})\xi^{\mathrm{d}} & \begin{matrix}2\rho_{\mathrm{ref}}d(U_2 - c^{\mathrm{d}})\xi^{\mathrm{d}}\mathrm{e}^{-\xi^{\mathrm{d}}d} \\ +\rho_{\mathrm{ref}}(U_2 - U_1)\mathrm{e}^{-\xi^{\mathrm{d}}d}\end{matrix} & \begin{matrix}-2\rho_{\mathrm{ref}}d(U_2 - c^{\mathrm{d}})\xi^{\mathrm{d}}\mathrm{e}^{+\xi^{\mathrm{d}}d} \\ +\rho_{\mathrm{ref}}(U_2 - U_1)\mathrm{e}^{+\xi^{\mathrm{d}}d}\end{matrix} & 0 \\ 0 & \begin{matrix}2\rho_{\mathrm{ref}}d(U_1 - c^{\mathrm{d}})\xi^{\mathrm{d}}\mathrm{e}^{+\xi^{\mathrm{d}}d} \\ +\rho_{\mathrm{ref}}(U_2 - U_1)\mathrm{e}^{+\xi^{\mathrm{d}}d}\end{matrix} & \begin{matrix}-2\rho_{\mathrm{ref}}d(U_1 - c^{\mathrm{d}})\xi^{\mathrm{d}}\mathrm{e}^{-\xi^{\mathrm{d}}d} \\ +\rho_{\mathrm{ref}}(U_2 - U_1)\mathrm{e}^{-\xi^{\mathrm{d}}d}\end{matrix} & 2\rho_1 d(U_1 - c^{\mathrm{d}})\xi^{\mathrm{d}} \\ 0 & \mathrm{e}^{+\xi^{\mathrm{d}}d} & \mathrm{e}^{-\xi^{\mathrm{d}}d} & -1 \end{bmatrix} \begin{bmatrix} A_1 \\ A_2 \\ B_2 \\ B_3 \end{bmatrix} = 0\,. \tag{4.26}$$

In a similar manner as the analysis of the single vortex sheet in the previous section, the determinant of the coefficient matrix can be calculated to obtain the dispersion relation. The coefficient matrix can be simplified from the 4×4 form to 2×2 form by performing the row operations[2]: R2−R1×$2\rho_2 d(U_2 - c^{\mathrm{d}})\xi^{\mathrm{d}}$ and R3+R4×$2\rho_1 d(U_1 - c^{\mathrm{d}})\xi^{\mathrm{d}}$. This gives

$$\mathcal{D}^{\mathrm{d}}(k^{\mathrm{d}}, \omega^{\mathrm{d}}) = \begin{vmatrix} \begin{matrix}2d(\rho_2 - \rho_{\mathrm{ref}})(U_2 - c^{\mathrm{d}})\xi^{\mathrm{d}}\mathrm{e}^{-\xi^{\mathrm{d}}d} \\ -\rho_{\mathrm{ref}}(U_2 - U_1)\mathrm{e}^{-\xi^{\mathrm{d}}d}\end{matrix} & \begin{matrix}2d(\rho_2 + \rho_{\mathrm{ref}})(U_2 - c^{\mathrm{d}})\xi^{\mathrm{d}}\mathrm{e}^{\xi^{\mathrm{d}}d} \\ -\rho_{\mathrm{ref}}(U_2 - U_1)\mathrm{e}^{\xi^{\mathrm{d}}d}\end{matrix} \\ \begin{matrix}2d(\rho_1 + \rho_{\mathrm{ref}})(U_1 - c^{\mathrm{d}})\xi^{\mathrm{d}}\mathrm{e}^{\xi^{\mathrm{d}}d} \\ +\rho_{\mathrm{ref}}(U_2 - U_1)\mathrm{e}^{\xi^{\mathrm{d}}d}\end{matrix} & \begin{matrix}2d(\rho_1 - \rho_{\mathrm{ref}})(U_1 - c^{\mathrm{d}})\xi^{\mathrm{d}}\mathrm{e}^{-\xi^{\mathrm{d}}d} \\ +\rho_{\mathrm{ref}}(U_2 - U_1)\mathrm{e}^{-\xi^{\mathrm{d}}d}\end{matrix} \end{vmatrix} = 0\,. \tag{4.27}$$

We adopt the following reference scales for velocity, density and length. Unlike the unconfined single vortex sheet discussed in the previous section, the single shear layer has a physical parameter in the form of the half shear width d which can be used as the length scale.

$$U_{\mathrm{ref}} = \frac{U_1 + U_2}{2}, \quad \rho_{\mathrm{ref}} = \frac{\rho_1 + \rho_2}{2}, \quad L_{\mathrm{ref}} = d\,. \tag{4.28}$$

The dimensionless variables can be then derived from the dimensional counterparts using these reference scales.

$$c = \frac{c^{\mathrm{d}}}{U_{\mathrm{ref}}}, \quad k = k^{\mathrm{d}}L_{\mathrm{ref}}, \quad \xi = \xi^{\mathrm{d}}L_{\mathrm{ref}}, \quad \omega = \frac{\omega^{\mathrm{d}}L_{\mathrm{ref}}}{U_{\mathrm{ref}}}\,. \tag{4.29}$$

The dimensionless parameters are also given as

$$\Lambda = \frac{U_1 - U_2}{U_1 + U_2}, \quad S = \frac{\rho_1 - \rho_2}{\rho_1 + \rho_2}\,. \tag{4.30}$$

Using the above quantities, the dimensionless dispersion relation is given as

$$\mathcal{D}(k, \omega) = \begin{vmatrix} -S(1 - \Lambda - c)\xi\mathrm{e}^{-\xi} + \Lambda\mathrm{e}^{-\xi} & (2 - S)(1 - \Lambda - c)\xi\mathrm{e}^{\xi} + \Lambda\mathrm{e}^{\xi} \\ (2 + S)(1 + \Lambda - c)\xi\mathrm{e}^{\xi} - \Lambda\mathrm{e}^{\xi} & S(1 + \Lambda - c)\xi\mathrm{e}^{-\xi} - \Lambda\mathrm{e}^{-\xi} \end{vmatrix} = 0\,. \tag{4.31}$$

[2]The notations R1,R2,... are used to represent rows 1,2,... respectively.

The dispersion relation can be verified by considering the value of the determinant in the long-wave limit $k \to 0$ or $\xi \to 0$. To begin with the calculation, the exponentials in Eq. 4.31 must be expanded as a Taylor series about $\xi = 0$ up-to $\mathcal{O}(\xi^2)$.

$$\mathrm{e}^{\pm\xi} = \sum_{n=0}^{\infty} \frac{(\pm 1)^n \xi^n}{n!} = 1 \pm \xi + \frac{\xi^2}{2} + \mathcal{O}(\xi^3)\,.$$

From Eq. 4.31, we get

$$\begin{aligned}
\mathcal{O}(\xi^0): \quad & -\Lambda^2 + \Lambda^2 = 0 \quad \checkmark \\
\mathcal{O}(\xi^1): \quad & 2\Lambda^2 + \Lambda S\left[(1+\Lambda-c) - (1-\Lambda-c)\right] \\
& + 2\Lambda^2 - \Lambda\left[(2+S)(1+\Lambda-c) - (2-S)(1-\Lambda-c)\right] \\
= \; & 4\Lambda^2 + 2\Lambda S(1-c) - 2\Lambda\left[(1+\Lambda-c) - (1-\Lambda-c)\right] \\
& - \Lambda S\left[(1+\Lambda-c) + (1-\Lambda-c)\right] \\
= \; & 4\Lambda^2 + 2\Lambda S(1-c) - 4\Lambda^2 - 2\Lambda S(1-c) = 0 \quad \checkmark \\
\mathcal{O}(\xi^2): \quad & -2*\Lambda^2 - 2\left[2\Lambda S(1-c)\right] - S^2(1+\Lambda-c)(1-\Lambda-c) \\
& + 2\Lambda^2 - 2\left[4\Lambda^2 + 2\Lambda S(1-c)\right] - (4-S^2)(1+\Lambda-c)(1-\Lambda-c) \\
= \; & -8\Lambda^2 - 8\Lambda S(1-c) - 4(1+\Lambda-c)(1-\Lambda-c) \\
= \; & -2\left[4\Lambda^2 + 2(1+\Lambda-c)(1-\Lambda-c)\right] - 2S \times 4\Lambda(1-c) \\
= \; & -2\left[(1+\Lambda-c)^2 + (1-\Lambda-c)^2\right] - 2S\left[(1+\Lambda-c)^2 - (1-\Lambda-c)^2\right] \\
= \; & -2\left[(1+S)(1+\Lambda-c)^2 + (1-S)(1-\Lambda-c)^2\right]\,.
\end{aligned}$$

Comparing the leading order expression in the long-wave limit with Eq. 4.13 (without surface tension, the third term in the dispersion relation vanishes), we see that the dispersion relation for unconfined vortex sheet is recovered. We infer that, up to $\mathcal{O}(\xi^2)$, the dispersion relation Eq. 4.31 for shear layer gives the same result in the long-wave limit as the vortex sheet and therefore, the dispersion relation is valid.

4.1.2.2 Stability analysis

The dispersion relation obtained from Eq. 4.31 is quadratic in c and is calculated from the determinant as

$$\begin{aligned}
\mathcal{D}(k,\omega) = \xi^2 \left[(\mathrm{e}^{+2\xi} - \mathrm{e}^{-2\xi})S^2 - 4\mathrm{e}^{+2\xi}\right] c^2 + \left[2(\mathrm{e}^{+2\xi} - \mathrm{e}^{-2\xi})(\xi LS - \xi^2 S^2) + 8\mathrm{e}^{+2\xi}\xi^2\right] c \\
+ (\mathrm{e}^{+2\xi} - \mathrm{e}^{-2\xi})\left[(\xi S - L)^2 - \xi^2 L^2 S^2\right] + 4\left[\xi^2(L^2-1) - \xi L^2\right]\mathrm{e}^{+2\xi} = 0\,.
\end{aligned} \tag{4.32}$$

Temporal stability analysis

For the temporal analysis, the value of complex ω is calculated for real k values from Eq. 4.32

$$\omega = \xi \frac{-p_1 \pm \sqrt{p_1^2 - 4p_2p_0}}{2p_2}\,, \tag{4.33}$$

where p_0, p_1, p_2 are the coefficients of c^0, c^1, c^2 in Eq. 4.32 respectively. For simplified case of homogeneous flow, both upper and lower streams having same density, we have $S = 0$ and the phase velocity can be calculated from Eq. 4.33 as

$$c = \frac{\omega}{k} = 1 \pm \mathrm{i}\frac{\Lambda}{2\xi}\sqrt{\mathrm{e}^{-4\xi} - (1-2\xi)^2}\,. \tag{4.34}$$

From Eq. 4.34, it is inferred that the neutral stability ($\omega_\mathrm{i} = 0$) appears at $k = k_d$, which is calculated for $\mathrm{e}^{-4k_d} - (1-2k_d)^2 = 0$. The temporal growth rate plot for the shear layer and unconfined vortex sheet without surface tension is shown in Fig. 4.6. Therefore, the shear layer is temporally unstable for value of k in the range $0 < k < k_d$. For the parameter set $(\Lambda, S) = (1, 0)$, we have $k_d = 0.64$. This value is less than that of unconfined vortex sheet, where $k_d = 1$. This indicates that the piecewise linear shear layer has a stabilising effect. The maximum temporal growth rate for the homogeneous case can also be calculated from Eq. 4.34. We have

$$\frac{\partial\omega}{\partial k} = 1 \pm \mathrm{i}\Lambda\frac{-\mathrm{e}^{-4\xi} - (1-2\xi)}{\sqrt{\mathrm{e}^{-4\xi} - (1-2\xi)^2}} = 0\,, \tag{4.35}$$

which gives the maximum temporal growth rate of $\omega_\mathrm{i} = 0.201$ at $k = 0.398$. From the Fig. 4.6, the recovery of the vortex sheet behaviour from the shear layer in the long wave limit ($k \to 0$) can also be observed.

Spatio-temporal stability analysis

The dispersion relation $\mathcal{D}(k, \omega; R) = 0$ given by Eq. 4.32 is second order in c. This yields two Riemann surfaces in the complex k-space. The solution is plotted in Fig. 4.7. The saddle point is given by the simultaneous solution of Eq. 4.32 and $\partial\mathcal{D}/\partial k = 0$. Due to appearance of several exponential terms which introduce periodicity in the solution $c(k; R)$ to the dispersion relation, the Riemann surface has multiple saddle points in the complex k-space. The saddle point that satisfies the pinching condition for the parameter $(\Lambda, S) = (2, 0)$ is obtained at $(k_s, \omega_s) = (0.6658 + 0\mathrm{i}, 0.6157 + 0\mathrm{i})$. As $\omega_\mathrm{i} = 0$, the shear layer is stable.

The eigenfunction corresponding to the saddle point is plotted in Fig. 4.8. The contribution from $\mathrm{Im}(\phi)$ is zero as is expected for the saddle point with $\xi_\mathrm{i} = 0$.

4.1.3 Alternate reference scale and parameter definition

For consistency with the proceeding formulation in § 4.2 and § 4.3, an alternate set non-dimensionalising parameters is introduced. The reformulated reference scales and parameters ensures that the behaviour of the dispersion relation is dominated by the relative, rather than absolute, velocity. As the behaviour will also be dominated by the denser fluid, which is already captured by the average density ρ_ref, the density reference scale remains unchanged.

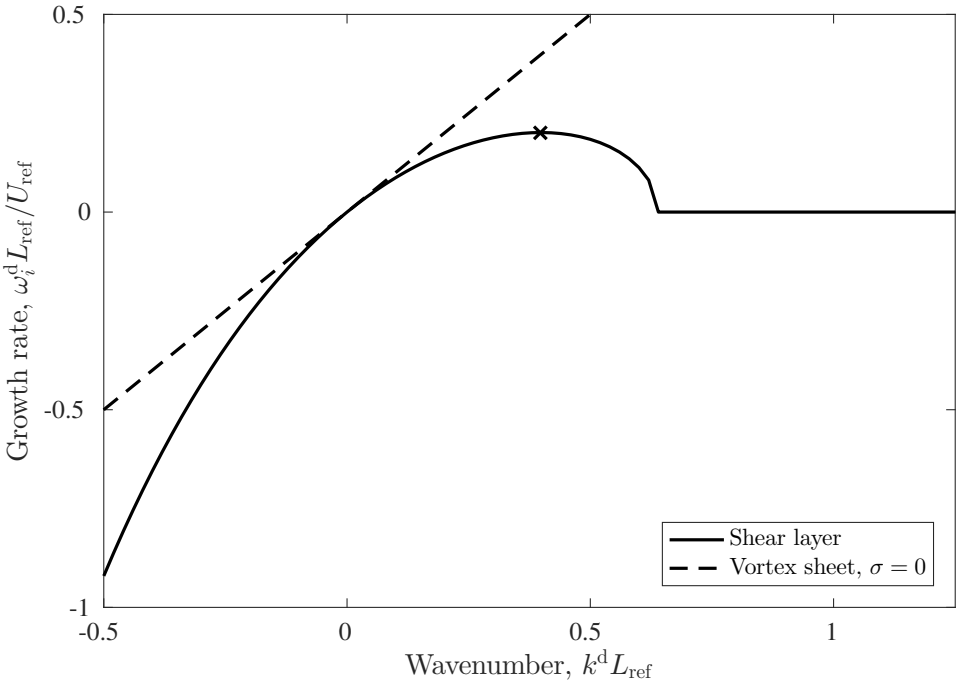

Figure 4.6: Temporal growth rate for the parameter $(\Lambda, S) = (1, 0)$ for single shear layer and unconfined vortex sheet without surface tension. The $\times$ indicates the temporal mode with the highest growth rate.

The reference velocity scale is redefined from the mean velocity to the characterisation of the shear strength.

$$U_{\mathrm{ref}} = \frac{U_2 - U_1}{2}\,. \tag{4.36}$$

The reference length scale for the flow with surface tension is determined by the value σ and therefore it remains unchanged as well. Only a factor 2 is removed from the scale for brevity.

$$L_{\mathrm{ref}} = \frac{\sigma}{\rho_{\mathrm{ref}} U_{\mathrm{ref}}^2}\,. \tag{4.37}$$

The non-dimensional parameter for velocity and density are also redefined as

$$\Lambda = \frac{U_2 - U_1}{U_2 + U_1}, \quad S = \frac{\rho_2 - \rho_1}{\rho_2 + \rho_1}\,. \tag{4.38}$$

The rest of the reference scales remain unchanged. The dispersion relations derived for the unconfined vortex sheet and piecewise linear shear layer can be reformulated in terms of the alternate scaling defined above.

We introduce non-dimensional parameters for *mass flux* ($\mathcal{M}$) and *momentum flux* ($\mathcal{J}$) which will be used to simplify the dispersion relation further.

$$\mathcal{M} = \frac{\frac{1}{2}(\rho_1 U_1 + \rho_2 U_2)}{\rho_{\mathrm{ref}} U_{\mathrm{ref}}} = \frac{1}{\Lambda} + S\,, \text{ and} \tag{4.39}$$

$$\mathcal{J} = \frac{\frac{1}{2}(\rho_1 U_1^2 + \rho_2 U_2^2)}{\rho_{\mathrm{ref}} U_{\mathrm{ref}}^2} = \frac{1}{\Lambda^2} + \frac{2S}{\Lambda} + 1\,. \tag{4.40}$$

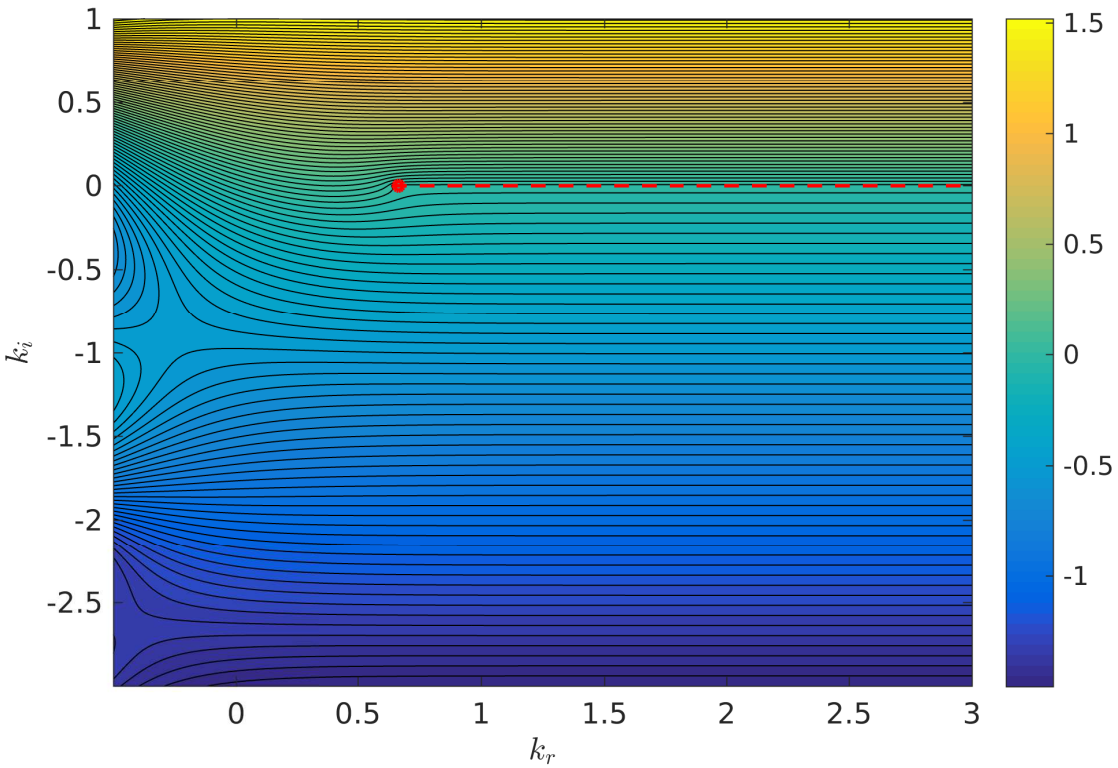

Figure 4.7: Solution to the dispersion relation $\mathcal{D}(k,\omega)=0$ for unconfined shear layer for the parameter $(\Lambda,S)=(2,0)$. The solution is represented by the contours of ω_i in the complex k-plane. The saddle point (circle) and branch cut (dashed line) are also indicated.

4.1.3.1 Unconfined single vortex sheet

From equation Eq. 4.9, the dispersion relation is given in terms of the scaling introduced in this section as

$$\mathcal{D}(k,\omega)=(1-S)(1/\Lambda-1-c)^2+(1+S)(1/\Lambda+1-c)^2-\xi=0\,. \tag{4.41}$$

The saddle point location can be calculated from the condition $\partial\mathcal{D}/\partial k=0$, which gives

$$k\frac{\partial\mathcal{D}}{\partial k}=2(1-S)(1/\Lambda-1-c)c+2(1+S)(1/\Lambda+1-c)c-k=0\,. \tag{4.42}$$

We note that $\xi=k$ when the real part of k is positive and $\xi=-k$ when the real part of k is negative. Using this information for $k_\mathrm{r}>0$ and the parameters given by Eq. 4.39 and Eq. 4.40, the Eq. 4.41 and Eq. 4.42 can be simplified as

$$2c^2-4\mathcal{M}c+2\mathcal{J}-k=0\,,\ \text{and} \tag{4.43}$$

$$-4c^2+4\mathcal{M}c-k=0\,. \tag{4.44}$$

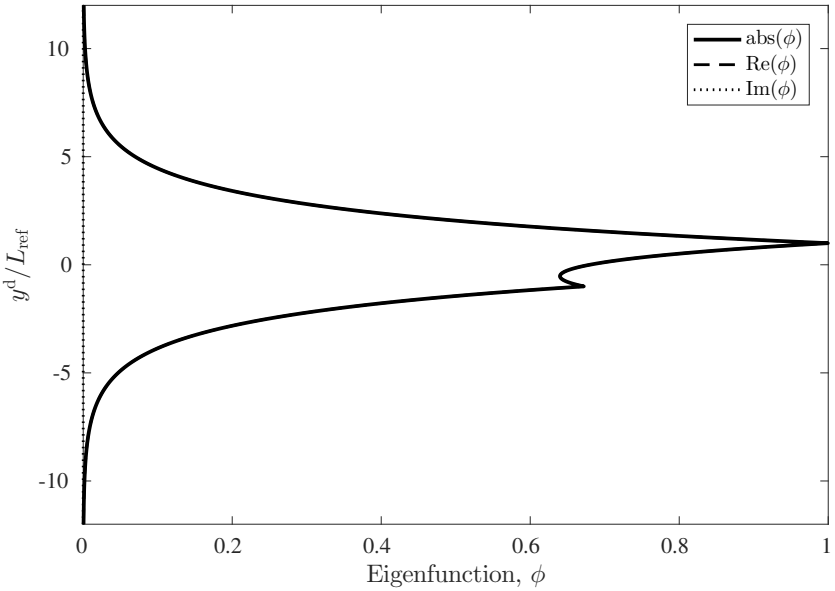

Figure 4.8: Eigenfunction for piecewise linear shear layer at the saddle point corresponding to the parameter $(\Lambda, S) = (2, 0)$.

The location of the saddle point is given as the solution of the two equations

$$c = \frac{2}{3}(1 \pm \mathcal{Q}^{1/2})\mathcal{M}\,, \text{ and} \tag{4.45}$$

$$k = \frac{8}{9}(1 - 2\mathcal{Q} \mp \mathcal{Q}^{1/2})\mathcal{M}^2\,, \tag{4.46}$$

where $\mathcal{Q} = 1 - 3\mathcal{J}/(4\mathcal{M}^2)$. The transition occurs when $\mathcal{Q} = 0$, or $3\mathcal{J} = 4\mathcal{M}^2$. As $\mathcal{J} = \mathcal{M}^2 - S^2 + 1$, the transition condition is given as

$$\frac{1}{3}\mathcal{M}^2 + S^2 = 1\,. \tag{4.47}$$

Substituting the value of $\mathcal{M}$ from Eq. 4.39 into Eq. 4.47, we recover the Eq. 6.13 for the CAIB, see § 6.2. The results discussed in § 4.1.1 remain qualitatively the same with this change of definition of reference scales.

4.1.3.2 Unconfined single shear layer

From equation Eq. 4.27, the dispersion relation is given in terms of the scaling introduced in this section as

$$\mathcal{D}(k, \omega) = 4\Lambda^2\xi^2c^2 - 8\Lambda\xi^2c + 4\xi^2 - (2\xi - 1)^2\Lambda^2 + \Lambda^2\mathrm{e}^{-4\xi} = 0\,. \tag{4.48}$$

Because of the presence of exponential term, a closed form solution for the saddle point similar to the unconfined single vortex sheet case cannot be obtained analytically and therefore the numerical procedures are employed to obtain the solutions. The results discussed in § 4.1.2 remain qualitatively the same with this change of definition of reference scales.

4.1.4 Conclusion

The single shear layer with and without surface tension is examined to study the behaviour of an isolated shear layer without the contribution from neighbouring shear layer interactions which will be discussed in § 4.2.

The presence of non-zero surface tension and/or shear width act as stabilising mechanisms for perturbations with short wavelengths. The neutral stability at long wave limits is expected to be dictated by the more dominant mechanism. This behaviour can be used to formulate the criterion for the surface tension dominated and shear layer dominated regimes. The flow is surface tension dominated for $k_\sigma^{\mathrm{d}} \ll k_d^{\mathrm{d}}$ and shear layer dominated for $k_\sigma^{\mathrm{d}} \gg k_d^{\mathrm{d}}$. As $k_\sigma = 1$ and $k_d = 0.64$, we have

$$\frac{k_\sigma^{\mathrm{d}}}{k_d^{\mathrm{d}}} = \frac{2k_\sigma U_{\mathrm{ref}}^2/\sigma}{k_d/d} = \frac{2dU_{\mathrm{ref}}^2}{0.64\sigma}\,. \tag{4.49}$$

We can use the Weber number, $We \equiv 2dU_{\mathrm{ref}}^2/\sigma$ to define the criterion for surface tension dominated regime as $We \ll 0.64$ and for shear layer dominated regime as $We \gg 0.64$.

4.2 Inviscid planar jets and wakes

4.2.1 Double vortex sheet

In this section, the spatio-temporal stability of inviscid jet and wake flow with surface tension will be performed. This analysis follows from the stability analysis for the double vortex sheet performed by Juniper [17]. In the solution, surface tension contributes to one mode and the confinement contributes to several *column* modes. The instability arises due to interaction of the two modes. The saddle point s_1 due to the surface tension is more unstable (has a larger ω_i value) than the saddle point obtained for finite shear layer (see § 4.1.2.2). The surface tension causes the interface to act as a elastic sheet, on which the perturbations can propagate upstream. The interaction between the two shear layers for jet and wake cases also introduces infinite number of saddle points s_2. The variation of surface tension causes the s_1 and s_2 saddle points to interact which will be examined in this section.

In this analysis, viscosity is neglected which makes the result applicable to only high Reynolds number $Re > 10^3$. Also the plug velocity profile is considered which makes the analysis independent of the stabilising effect of the finite shear thickness. Therefore, for practical flows with finite shear width δ_v, if the saddle point corresponding to the absolute instability has wavenumber $k_s > \mathcal{O}(2\pi/\delta_v)$, the flow will be actually stabilised.

4.2.1.1 Dispersion relation

The schematic for the flow is shown in Fig. 3.2(c). The parallel flow is infinite in the streamwise x-direction and uniform in the spanwise z-direction.

The streamfunctions in the three streams $i = 1, 2, 3$ are given as

$$\begin{aligned}
\phi_1 &= A_1 \cosh(\xi^{\mathrm{d}}(y^{\mathrm{d}} - h_1 - h_2)) + B_1 \sinh(\xi^{\mathrm{d}}(y^{\mathrm{d}} - h_1 - h_2))\,,\\
\phi_2 &= A_2 \cosh(\xi^{\mathrm{d}} y^{\mathrm{d}}) + B_2 \sinh(\xi^{\mathrm{d}} y^{\mathrm{d}})\,,\\
\phi_3 &= A_3 \cosh(\xi^{\mathrm{d}}(y^{\mathrm{d}} + h_1 + h_2)) + B_3 \sinh(\xi^{\mathrm{d}}(y^{\mathrm{d}} + h_1 + h_2))\,.
\end{aligned} \tag{4.50}$$

As discussed in the previous section, the solution can be decomposed to represent sinuous or varicose modes individually. As $\sinh(x)$ is an odd function and $\cosh(x)$ is an even function, the eigenfunction associated with the inner stream $i = 2$ can be distinctly expressed for each mode. For varicose mode, we have

$$\phi_2(-y^{\mathrm{d}}) = -\phi_2(y^{\mathrm{d}}) \quad \Rightarrow \quad A_2 = 0\,, \tag{4.51}$$

and for sinuous mode, we have

$$\phi_2(-y^{\mathrm{d}}) = \phi_2(y^{\mathrm{d}}) \quad \Rightarrow \quad B_2 = 0\,, \tag{4.52}$$

As the varicose and sinuous modes can be incorporated in the analysis by excluding the first and the second terms respectively from ϕ_2, the third streamfunction ϕ_3 can be neglected. In order to derive the dispersion relation $\mathcal{D}(k,\omega)$, we apply the matching conditions at the two interfaces. Using the dimensional form of kinematic matching condition

$$\left[\!\left[\frac{\phi_i}{(U_i - c^{\mathrm{d}})}\right]\!\right] = 0\,, \tag{4.53}$$

we get for varicose mode

$$\frac{A_1\cosh(\xi^d h_2) - B_1\sinh(\xi^d h_2)}{U_2 - c^{\mathrm{d}}} = \frac{B_2\sinh(\xi^d h_1)}{U_1 - c^{\mathrm{d}}}\,, \tag{4.54}$$

and for sinuous mode

$$\frac{A_1\cosh(\xi^d h_2) - B_1\sinh(\xi^d h_2)}{U_2 - c^{\mathrm{d}}} = \frac{A_2\cosh(\xi^d h_1)}{U_1 - c^{\mathrm{d}}}\,. \tag{4.55}$$

Next, the dimensional form of dynamic matching condition gives

$$\left[\!\left[\rho_i(U_i - c^{\mathrm{d}})\phi_i' - \rho_i U_i'\phi_i\right]\!\right] \mathrm{e}^{\mathrm{i}(k^{\mathrm{d}}x^{\mathrm{d}} - \omega^{\mathrm{d}}t^{\mathrm{d}})} = \Delta p^{\mathrm{d}}\,, \tag{4.56}$$

where Δp^{d} is the pressure jump as a result of the surface tension at the interface. From Appendix B, the pressure jump can be calculated. The matching condition for the varicose mode is given as

$$\begin{aligned}\frac{\sigma(\xi^{\mathrm{d}})^2}{U_2 - c^{\mathrm{d}}}(A_1\cosh(\xi^{\mathrm{d}}h_2) - B_1\sinh(\xi^{\mathrm{d}}h_2)) + \rho_2\xi^{\mathrm{d}}(U_2 - c^{\mathrm{d}})(B_1\cosh(\xi^{\mathrm{d}}h_2) - A_1\sinh(\xi^{\mathrm{d}}h_2))\\ = B_2\rho_1\xi^{\mathrm{d}}(U_1 - c^{\mathrm{d}})\cosh(\xi^{\mathrm{d}}h_1)\,.\end{aligned} \tag{4.57}$$

Next, the matching condition for the sinuous mode is given as

$$\begin{aligned}\frac{\sigma(\xi^{\mathrm{d}})^2}{U_2 - c^{\mathrm{d}}}(A_1\cosh(\xi^{\mathrm{d}}h_2) - B_1\sinh(\xi^{\mathrm{d}}h_2)) + \rho_2\xi^{\mathrm{d}}(U_2 - c^{\mathrm{d}})(B_1\cosh(\xi^{\mathrm{d}}h_2) - A_1\sinh(\xi^{\mathrm{d}}h_2))\\ = A_2\rho_1\xi^{\mathrm{d}}(U_1 - c^{\mathrm{d}})\sinh(\xi^{\mathrm{d}}h_1)\,.\end{aligned} \tag{4.58}$$

The eigenfunction represented in Eq. 4.50 satisfies the boundary condition $\phi_i = 0$ at $y^{\mathrm{d}} = \pm(h_1 + h_2)$ if $A_1 = A_3 = 0$. Thus, for the matching condition at the interface at $y^{\mathrm{d}} = +h_1$, we have two matching conditions and two constant eigenfunction amplitudes B_1, B_2 or B_1, A_2 corresponding to

varicose and sinuous modes respectively. By eliminating the constants, we obtain the dimensional form of dispersion relation $\mathcal{D}^{\mathrm{d}}(k^{\mathrm{d}}, \omega^{\mathrm{d}})$. For varicose mode, we get

$$\mathcal{D}^{\mathrm{d}}(k^{\mathrm{d}}, \omega^{\mathrm{d}}) = \rho_1 (U_1 - c^{\mathrm{d}})^2 \coth(\xi^{\mathrm{d}} h_1) + \rho_2 (U_2 - c^{\mathrm{d}})^2 \coth(\xi^{\mathrm{d}} h_2) - \sigma \xi^{\mathrm{d}} = 0\,. \tag{4.59}$$

For sinuous mode, we get

$$\mathcal{D}^{\mathrm{d}}(k^{\mathrm{d}}, \omega^{\mathrm{d}}) = \rho_1 (U_1 - c^{\mathrm{d}})^2 \tanh(\xi^{\mathrm{d}} h_1) + \rho_2 (U_2 - c^{\mathrm{d}})^2 \coth(\xi^{\mathrm{d}} h_2) - \sigma \xi^{\mathrm{d}} = 0\,. \tag{4.60}$$

The dispersion relation can be made non-dimensional by using reference scales and non-dimensional parameters. The reference scales for velocity and density are given as

$$U_{\mathrm{ref}} = \frac{U_2 - U_1}{2}\,, \tag{4.61}$$

$$\rho_{\mathrm{ref}} = \frac{\rho_1 + \rho_2}{2}\,. \tag{4.62}$$

The reference scale for length can be defined in terms of the surface tension or the distance between shear layers.

$$L_{\mathrm{ref}} = \frac{\sigma}{\rho_{\mathrm{ref}} U_{\mathrm{ref}}^2}\,, \tag{4.63}$$

$$h_{\mathrm{ref}} = \left(\frac{1}{h_1} + \frac{1}{h_2}\right)^{-1}\,. \tag{4.64}$$

For the current study of the confined double vortex sheet, the length scale L_{ref} is used. The dimensionless variables can be then derived from the dimensional counterparts using these reference scales.

$$c = \frac{c^{\mathrm{d}}}{U_{\mathrm{ref}}}, \quad k = k^{\mathrm{d}} L_{\mathrm{ref}}, \quad \xi = \xi^{\mathrm{d}} L_{\mathrm{ref}}, \quad \omega = \frac{\omega^{\mathrm{d}} L_{\mathrm{ref}}}{U_{\mathrm{ref}}}\,. \tag{4.65}$$

The dimensionless parameters are also given as

$$\Lambda = \frac{U_2 - U_1}{U_1 + U_2}\,, \tag{4.66}$$

$$S = \frac{\rho_2 - \rho_1}{\rho_1 + \rho_2}\,, \tag{4.67}$$

$$h = \frac{h_2 - h_1}{h_2 + h_1}\,, \tag{4.68}$$

$$\Sigma = \frac{\sigma}{h_{\mathrm{ref}} \rho_{\mathrm{ref}} U_{\mathrm{ref}}^2} = \frac{L_{\mathrm{ref}}}{h_{\mathrm{ref}}}\,. \tag{4.69}$$

As discussed above, the model has limited application at extremely small surface tension, which implies that L_{ref} may be smaller than $\mathcal{O}(\delta_v)$. In non-dimensional form, the varicose and sinuous dispersion relations are given as

$$\begin{aligned}\mathcal{D}(k, \omega) = {} & (1 - S)(1/\Lambda - 1 - c)^2 \coth\left(\frac{2\xi}{\Sigma(1 + h)}\right) \\ & + (1 + S)(1/\Lambda + 1 - c)^2 \coth\left(\frac{2\xi}{\Sigma(1 - h)}\right) - \xi\,,\end{aligned} \tag{4.70}$$

$$\begin{aligned}\mathcal{D}(k, \omega) = {} & (1 - S)(1/\Lambda - 1 - c)^2 \tanh\left(\frac{2\xi}{\Sigma(1 + h)}\right) \\ & + (1 + S)(1/\Lambda + 1 - c)^2 \coth\left(\frac{2\xi}{\Sigma(1 - h)}\right) - \xi\,.\end{aligned} \tag{4.71}$$

4.2.1.2 Spatio-temporal stability analysis

The stability analysis is performed to evaluate the response to an impulse at a spatial point or the full impulse response in the outer flow. The saddle point needs to be tracked for each of these analyses. The positions of the saddle point can be characterised by the components of the dispersion relation.

To begin with identifying the location of the saddle points, we can look at the simple form of non-dimensional dispersion relation for an unconfined vortex sheet with surface tension as given by Eq. 4.13. The dispersion relation should be first rewritten in terms of the non-dimensional parameters defined in the previous section.

$$\mathcal{D}(k,\omega) = (1-S)(1/\Lambda - 1 - c)^2 + (1+S)(1/\Lambda + 1 - c)^2 - \xi = 0\,. \tag{4.72}$$

When compared with Eq. 4.70 and Eq. 4.71, it can be observed that the addition of the additional shear layer manifests itself in the form of the factors $\coth(2\xi/\Sigma(1+h)$ and $\tanh(2\xi/\Sigma(1+h)$ multiplied to the first term for varicose and sinuous perturbations respectively. For the unconfined flow, we have $\coth(2\xi/\Sigma(1-h) \to 1$ as $h \to 1$. The hyperbolic functions lead to an infinite number of simple poles in the k space along the k_i-axis where the function value is infinite. The poles occur at

$$k = \mathrm{i}n\pi\frac{\Sigma(1+h)}{2} \qquad \text{for varicose mode, and} \tag{4.73}$$

$$k = \mathrm{i}\left(n+\frac{1}{2}\right)\pi\frac{\Sigma(1+h)}{2} \qquad \text{for sinuous mode}\,. \tag{4.74}$$

where $n \in \mathbb{Z}$. For confined flows, an additional $\coth(2\xi/\Sigma(1-h))$ factor appears with the second term in both varicose and sinuous dispersion relations. This factor introduces additional poles along the k_i-axis at

$$k = \mathrm{i}n\pi\frac{\Sigma(1-h)}{2}\,. \tag{4.75}$$

The third term in the dispersion relation $(-\xi)$ represents the contribution of the surface tension at the interface of two streams. For low values of surface tension parameter $\Sigma \to 0$, the hyperbolic functions take the value ± 1. Following the same temporal analysis as in § 4.1.1.2, the position of the branch point in the k-space is obtained along the k_r-axis at $k = +\infty$ and $k = 2(1-S^2)$ for both varicose and sinuous modes. For higher values of surface tension parameter, we have

$$\lim_{\Sigma\to\infty} \coth\left(\frac{2\xi}{\Sigma(1\pm h)}\right) = \frac{\Sigma(1\pm h)}{2\xi} \quad \text{, and} \tag{4.76}$$

$$\lim_{\Sigma\to\infty} \tanh\left(\frac{2\xi}{\Sigma(1+h)}\right) = \frac{2\xi}{\Sigma(1+h)}\,. \tag{4.77}$$

Using these values in Eq. 4.70 and Eq. 4.71, we can obtain the location of the branch point near $k = 0$ in the k-space. For the varicose mode, the branch point appears at

$$k = \sqrt{\frac{(1-h^2)(1-S^2)\Sigma}{1-hS}}\,. \tag{4.78}$$

Similarly, for the sinuous mode, the branch point appears at

$$k = \sqrt{\frac{(1-h)(1+S)(\Sigma(1+h)+8(S-1))\Sigma}{4(S-1)}}\,. \tag{4.79}$$

The series of poles associated with the hyperbolic functions form the saddle points of the sinuous and varicose dispersion relations along the k_i-axis. These saddle points correspond to the modes associated with the interaction between shear layers or the interaction between shear layer and its image system. The location of these modes, referred as *jet/wake column modes*, is influenced by parameters h and Σ. The presence of the surface tension branch point also introduces a saddle point near the k_r-axis. The *surface tension saddle* accounts for the influence of surface tension on the shear layer instability.

4.2.2 Evaluation of impulse response

We recall from § 2.3 that the nature of response $\mathcal{G}(\mathbf{x},t)$ to a perturbation observed at the source of the perturbation gives the nature of instability. If the response at the source grows temporally, the flow is absolutely unstable. On the other hand, a temporally decaying response indicates either convectively unstable or stable. According to Juniper [14], as a result of the kinematic response to the perturbation at the shear layer, the perturbation that initiates and evolves in the shear layer also propagates and evolves in the outer flow.

When the perturbations are restricted to real wavenumbers ($k \in \mathbb{R}$), the waves propagate with constant amplitude in the x-direction and with exponentially decaying amplitude in the y-direction. However, for complex wavenumbers ($k \in \mathbb{C}$), the perturbation waves propagate with constant amplitude along a ray at an angle to the x-direction and exponentially decay in the direction orthogonal to the ray. The study of the modes that propagate and evolve in the outer fluid therefore provides a better understanding of the response.

4.2.2.1 One-dimensional response

The one dimensional response for a unit impulse is given by Eq. 2.30. Following a similar analysis as Juniper [14], the perturbations stream function for shear flows, given by Eq. 4.1 for example, can be used to evaluate the response along the streamwise direction as

$$\psi_i(x,t) = \frac{1}{(2\pi)^2}\int_F\int_L \widehat{\psi}_i(k,\omega)\mathrm{e}^{\mathrm{i}(kx-\omega t)}\,\mathrm{d}\omega\,\mathrm{d}k\,, \tag{4.80}$$

where $\widehat{[\cdot]}$ represents the terms in (k,ω)-space obtained from double Fourier transform of functions in (x,t)-space. Following Eq. 1.6, the unit impulse $S_i(x,t) = \delta(x)\delta(t)$ can be replaced by a generic source $S_i(x,t)$. Therefore, the source of perturbation $S_i(x,t)$ can be given as the operation of dispersion relation $\mathcal{D}(k,\omega)$ in the form of a differential operator on the perturbation streamfunction.

$$\mathcal{D}\left(-\mathrm{i}\frac{\partial}{\partial x}, \mathrm{i}\frac{\partial}{\partial t}\right)\psi_i(x,t) = S_i(x,t)\,. \tag{4.81}$$

By definition, the source can also be defined by the double Fourier integral of the normal modes

$$S_i(x,t) = \frac{1}{(2\pi)^2}\int_F\int_L \widehat{S}_i(k,\omega)\mathrm{e}^{\mathrm{i}(kx-\omega t)}\,\mathrm{d}\omega\,\mathrm{d}k\,. \tag{4.82}$$

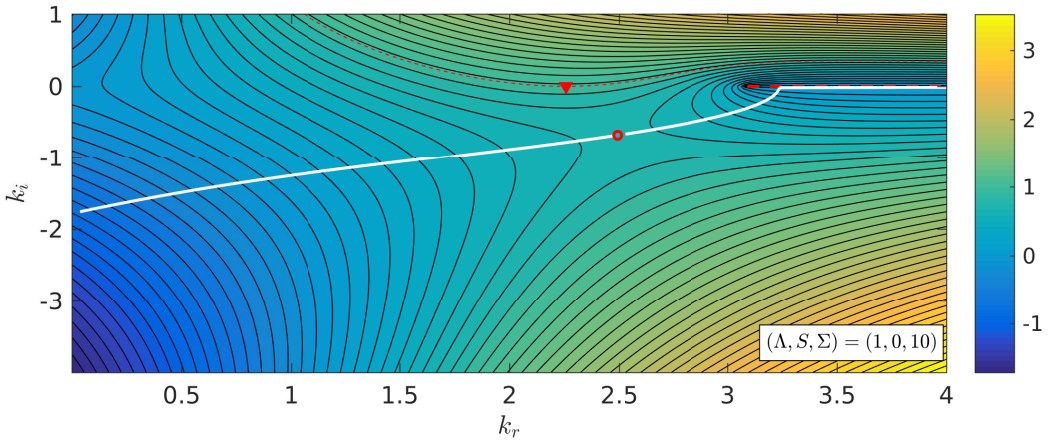

(a)

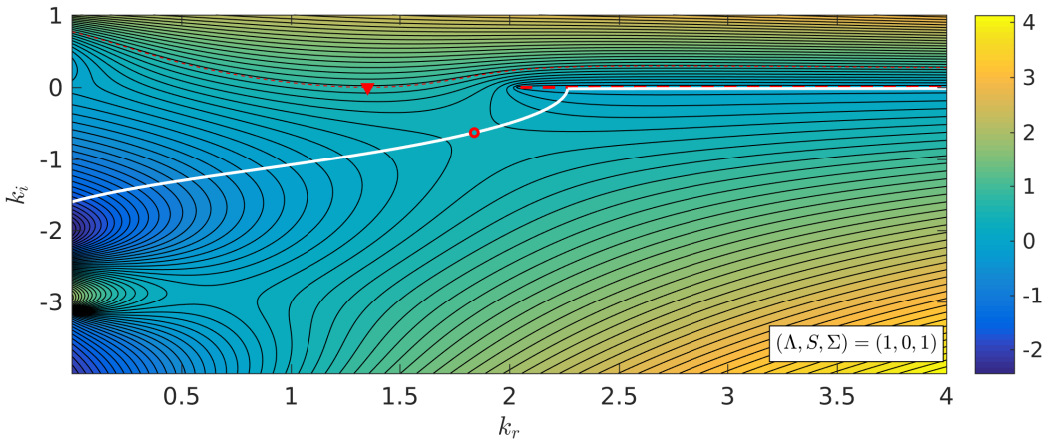

(b)

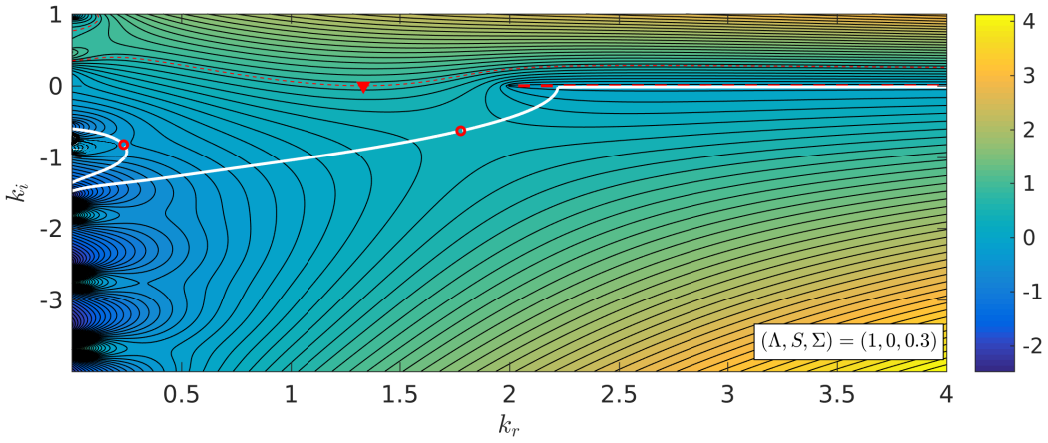

(c)

Figure 4.9: Contours of ω_i for varicose perturbations in uniform density ($S = 0$) unconfined wake ($\Lambda > 1$) flow with surface tension ($\Sigma \neq 0$). The saddle points near the k_r-axis (say s_1) represent surface tension modes while saddle points along the k_i-axis (say $s_{2\mathrm{a}}, s_{2\mathrm{b}}$, etc. in order from top to bottom) represent jet/wake column modes. The position of the maximum growth rate predicted by temporal analysis is shown by a triangle. As the surface tension decreases, the integration path (white line) traverses both the saddle points s_1 and $s_{2\mathrm{a}}$.

Using Eq. 4.80 and Eq. 4.82, Eq. 4.81 can be rewritten as

$$\widehat{\psi}_i(k,\omega)\mathcal{D}(k,\omega) = \widehat{S}_i(k,\omega)\,. \tag{4.83}$$

For unit impulse, we have $\widehat{S}_i(k,\omega) = 1$ and $\psi(x,t)$ gives the impulse response.

4.2.2.2 Two-dimensional response

A mode of the perturbation stream function in two spatial dimensions is given by Eq. 4.1 as

$$\psi_i(x,y,t) = \phi_i(y;\xi)\mathrm{e}^{\mathrm{i}(kx-\omega t)}\,. \tag{4.84}$$

The eigenfunction $\phi_i(y;\xi)$ gives the mode shape and can be calculated by using Eq. 4.2 with relevant boundary conditions. The full streamfunction is obtained in the similar form of Eq. 4.80 by taking the double Fourier transform of the product of normal mode perturbation $\widehat{\psi}_i$ and the mode shape $\phi_i(y;\xi)$.

$$\psi_i(x,y,t) = \frac{1}{(2\pi)^2}\int_F\int_L \widehat{\psi}_i(k,\omega)\phi_i(y;\xi)\mathrm{e}^{\mathrm{i}(kx-\omega t)}\,\mathrm{d}\omega\,\mathrm{d}k\,. \tag{4.85}$$

In a similar fashion, the two-dimensional form of source for a uniformly perturbed flow can be obtained from Eq. 4.82 by taking the double Fourier transform of the product of the normal modes in Eq. 4.82 and the mode shape

$$S_i(x,y,t) = \frac{1}{(2\pi)^2}\int_F\int_L \widehat{S}_i(k,\omega)\phi_i(y;\xi)\mathrm{e}^{\mathrm{i}(kx-\omega t)}\,\mathrm{d}\omega\,\mathrm{d}k\,. \tag{4.86}$$

Substituting Eq. 4.85 and Eq. 4.86 in Eq. 4.81, the same spectral relation as Eq. 4.83 is obtained. Therefore, the two-dimensional response can be obtained by substituting Eq. 4.83 into Eq. 4.85. The integration method will be explained now.

4.2.2.3 Evaluation of double Fourier integral

The integration in ω can be performed using the residue theorem. The procedure is similar to the one explained in Appendix A where the integration over k is performed first which results in Eq. A.7. A similar result is obtained when the integration over ω is performed first. The modes that are excited by the impulse and satisfy dispersion relation, $\mathcal{D}(k,\omega) = 0$ are only retained. For each value of k, two values of ω exist that satisfy the dispersion relation. The solutions are symmetric under the transformation $\mathrm{Re}\{k^+,\omega^+\} \leftrightarrow -\mathrm{Re}\{k^-,\omega^-\}$. Therefore, the integration paths and ω-plane are mirror images of each other about the imaginary axis in the complex k- and ω-planes. Thus, integration can be performed only over one of the branches to give the full response as

$$\psi_i(x,y,t) = -\frac{\mathrm{i}}{2\pi}\int_F \frac{\phi_i(y;\xi)}{\frac{\partial\mathcal{D}}{\partial\omega}(k,\omega(k))}\mathrm{e}^{\mathrm{i}(kx-\omega(k)t)}\,\mathrm{d}k\,. \tag{4.87}$$

Therefore, the response in the outer fluid $i = 1$ to the eigenfunction of form $\phi_1(y;\xi) = A\mathrm{e}^{+\xi y}$ is calculated as

$$\psi_1(x,y,t) = -\frac{\mathrm{i}}{2\pi}\int_F \frac{A}{\frac{\partial\mathcal{D}}{\partial\omega}(k,\omega(k))}\mathrm{e}^{-\mathrm{i}gt}\,\mathrm{d}k\,, \tag{4.88}$$

where, $g \equiv \omega(k) - kx/t - \mathrm{i}\xi y/t$. The growth rate corresponding to the impulse response in the outer fluid is given by the imaginary part g_i in the $(x/t, y/t)$-space. By definition, at the source $(x/t, y/t) = (0, 0)$, the flow is convectively unstable for $g_\mathrm{i} < 0$ and absolutely unstable for $g_\mathrm{i} > 0$. This also allows to make the distinction alternatively from the value of y/t at $x/t = 0$ while bringing the growth rate to $g_\mathrm{i} = 0$; if $y/t < 0$, flow is convectively unstable and if $y/t > 0$, flow is absolutely unstable. The result from one such analysis is given in Table 4.1. The values correspond to the dominant surface tension saddle s_1. It is observed that for the given parameter set, the flow transitions from absolute to convective instability as the magnitude of non-dimensional velocity parameter Λ reduces.

Table 4.1: Example of impulse response in outer fluid for varicose perturbation of unconfined double vortex sheet

(Λ, S, Σ, h)	x/t	y/t	g_i
$(-2/3, -0.2, 0.001, 1)$	0	$+0.4873$	0
$(-1/3, -0.2, 0.001, 1)$	0	-0.2930	0

For a given value of $(x/t, y/t)$, the dominant contribution to the integral in Eq. 4.88 comes from the saddle point of the function $g(k; x/t, y/t)$. We have $\partial g/\partial k = 0$ at the saddle points and therefore, the group velocity becomes

$$\frac{\partial \omega}{\partial k} = \frac{x}{t} + \mathrm{i}\frac{y}{t}\,. \tag{4.89}$$

This indicates that the dominant contributions come from the disturbances that travel with the same group velocity as the observer.

4.2.2.4 Integration contour for asymptotic impulse response

The method of contour integration for asymptotic response has been discussed by Juniper [17]. The contours of g_i for $(x/t, y/t) = (0, 0)$ are plotted in Fig. 4.9 for decreasing value of surface tension parameter Σ. The asymptotic impulse response is obtained from Eq. 4.88 by integrating along the path that originally lies along the k_r-axis and runs from $k_\mathrm{r} \to -\infty$ to $k_\mathrm{r} \to +\infty$. However, the integral is more easily evaluated by deforming the path over the steepest descent line of saddle points while simultaneously avoiding the branch points and poles of hg_i. The deformed path is shown by a white line in Fig. 4.9. The integration path passes through the s_1 which results in the most dominating contribution to the integral as it has a higher value of g_i.

According to Briggs-Bers criterion explained in § 2.3, the saddle point contributes to the integration only if it has a hill made of upstream-propagating k^+-branches on one side and a hill of downstream propagating k^--branches on the other side. It is seen from the Fig. 4.9 that the integration path only traverses kind of saddle points. For saddle points lying in the $k_\mathrm{i} < 0$ half-plane, the k^+ branches are identified as those which lie entirely in the $k_\mathrm{i} > 0$ half-plane for g_i higher than the maximum temporal growth rate. On the other hand, the k^- remain in the lower half as g_i increases. Saddle s_1 forms a valid k^+/k^- pinch point and therefore it lies on the integration path.

The steepest descent path must, ideally, have a constant g_r to avoid oscillating terms (in $\mathrm{e}^{\mathrm{i}gt}$) but the condition is relaxed at large negative values of g_i with negligible contribution to the integral. This is needed when the surface tension decreases and the column modes s_2 also become valid k^+/k^- pinch points. This is shown in Fig. 4.9(c) where the integration path passes through a s_2

saddle point. More saddle points form valid k^+/k^- pinch points as $\Sigma \to 0$. It must be noted that the saddle integration path jumps to a different value g_r at these column modes in order to pass above the top branch point on the k_i-axis. Also it is observed that the s_1 saddle still remains the most unstable k^+/k^- pinch point though it moves to a lower k_r as the length scale associated with surface tension L_ref tends to zero.

4.2.3 Relevance of stability of unconfined single shear layer

The unconfined single shear layer with surface tension is discussed in § 4.1.1. The single shear layer presents a simple case where the analytical solutions of the dispersion relation can be obtained and used to develop a criteria for absolute instability. Therefore, before discussing the effect of addition of a second shear layer or confinement on the stability of jet/wake flows, the relevant results from the unconfined shear layer will be reviewed here.

When $\Sigma \ll 1$, the s_2 saddles move towards the k_i axis. This migration of the saddle point can also be seen in Fig. 4.9 as the value of Σ is decreased. The integration path passes over the s_1-saddle point and the through any of the s_2-saddles which lie between $k_\mathrm{i} = 0$ and the value of k_i where the integration path intersects the k_i-axis. Therefore, the impulse response is contributed by both the short wavelength (large k_r), rapidly evolving (highest g_i) surface tension modes (s_1), which causes the shear layers to behave independently, and the long wavelength, slowly evolving jet/wake column modes (s_2), which causes the shear layers to interact. In the limit $\Sigma \to 0$, the growth rate of the jet/wake column modes tends to zero ($g_i \to 0$) as can seen from the temporal growth rate plot Fig. 4.2 at $k_\mathrm{r} = 0$. The response then is dominated by the surface tension mode of the independent shear layers (s_1). This behaviour of double shear layer response can also be seen by considering the dispersion relations Eq. 4.70 and Eq. 4.71. As $\Sigma \to 0$, we have $\coth(2\xi/\Sigma(1 \pm h)) \to 1$ and $\tanh(2\xi/\Sigma(1 + h)) \to 1$, for sufficiently large ξ, *i.e.*, for modes lying far from the k_i-axis, like the s_1-saddle. Therefore, the dispersion relation for the single shear layer Eq. 4.41 is recovered far from the k_i-axis in low surface tension limit.

When $\Sigma \approx 1$, the shear layers interact with each other and with the walls. Again, the dispersion relations given by Eq. 4.70 and Eq. 4.71 transform back to the dispersion relation for the single shear layer given by Eq. 4.41 if the arguments of the hyperbolic functions are large. To obtain the limiting value of the stream width parameter h, which identifies the transition point when the spatio-temporal behaviour of the flow departs from the unconfined single shear layer behaviour, it is sufficient to acknowledge the fact that the hyperbolic functions assume values different than 1 when the argument is $\mathcal{O}(1)$ or lower. This happens when $2\xi/(\Sigma(1 \pm h)) \approx 1$, or

$$h \approx \pm \left(\frac{2\xi}{\Sigma} - 1 \right) . \tag{4.90}$$

The analytical solution of k can be used as a first order approximation to predict the limiting value from Eq. 4.90 when the influence of the second shear layer or the confinement becomes significant. From Eq. 4.46, we have the value of k in leading order as $k \approx -8(1/\Lambda + S)^2/9$. Substituting this value in Eq. 4.90 gives the sheet thickness parameter as

$$h \approx \pm \left(\frac{16(1/\Lambda + S)^2}{9\Sigma} - 1 \right) , \tag{4.91}$$

which gives the minimum value of parameter h up to which the second shear layer or confinement has no influence on the spatio-temporal behaviour while comparing the single and double shear layers.

When $\Sigma \gg 1$, the dispersion relation can be simplified to the algebraic form by approximating the hyperbolic functions in the strong surface tension limit. This will be discussed in § 6.3.2.

4.2.4 Conclusion

The effect of surface tension and confinement on the stability of jet/wake flows has been studied in this section. The spatio-temporal analysis and full impulse response methods were used for this purpose. It is shown that two modes govern the flow behaviour - one where the shear layers behave independently, and contribute to the surface tension modes, or the one where shear layers interact with the image system, and contribute to the jet/wake column modes. The surface tension mode dominates the impulse response owing to the higher value of the growth rate (g_i).

4.3 Semi-unconfined planar shear layer

The semi-unconfined shear layer flow is encountered in the wake of a micro-ramp which is used to suppress the Shock-Wave/Boundary-Layer Interaction (SWBLI). Groot *et al.* [9], investigated the applicability of the stability theory to reproduce the Kelvin-Helmholtz (KH) waves observed in experiments. The study found that the stability analysis on the mean flow predicts the most unstable wavelength within the experimentally observed range. In this chapter, the spatio-temporal analysis developed through § 4.1 and § 4.2 will be applied to the semi-unconfined shear layer and the stability will be studied.

4.3.1 Linear approximations to shear profile

As this chapter deals with the analytical study of the shear flow, the piecewise-linear profiles are considered to approximate the semi-unconfined shear layer and derive the algebraic dispersion relation. The semi-unconfined shear layer is characterised by a shear layer flow in the domain $y^\mathrm{d} \in [-h_\mathrm{w}, +\infty)$, where h_w is distance of the confining wall from the centre of the shear layer. Fig. 4.10 shows this flow configuration along with the piecewise linear approximations to the physical, smooth shear layer.

The piecewise linear velocity profiles, overlapped with the 'tanh' velocity profile and experimental base flow obtained from PIV (Particle Image Velocimetry) measurements by Groot *et al.* [9], is shown in Fig. 4.11. For the non-dimensional representation of the experimental base flow, Groot *et al.* [9] used the micro-ramp height h_r and streamwise edge velocity $\overline{U}_e(\cong U_2)$ as the length and velocity scales respectively. From Fig. 4.10, the values of the constants a and t define the piecewise linear profiles. For 3-piece and 5-piece linear profiles in Fig. 4.10, assigning the value $t = 2.5$ ensures that $U_2 \simeq 0.99U_\mathrm{e}$ on the 'tanh' profile in Fig. 4.11. For the 5-piece linear profile, the arbitrary value of $a = 0.25$ has been used in Fig. 4.11. For any other combination of values (a, t), it must be ensured that $0 \leq at < 1$. For $(a, t) = (0, 1)$, the 1-piece linear profile is obtained back from the 3-piece and 5-piece linear profiles. Also note that the study by Groot *et al.* [9] was performed for a homogeneous wake, *i.e.*, $\rho_1 = \rho_2$. The analytical dispersion relations will

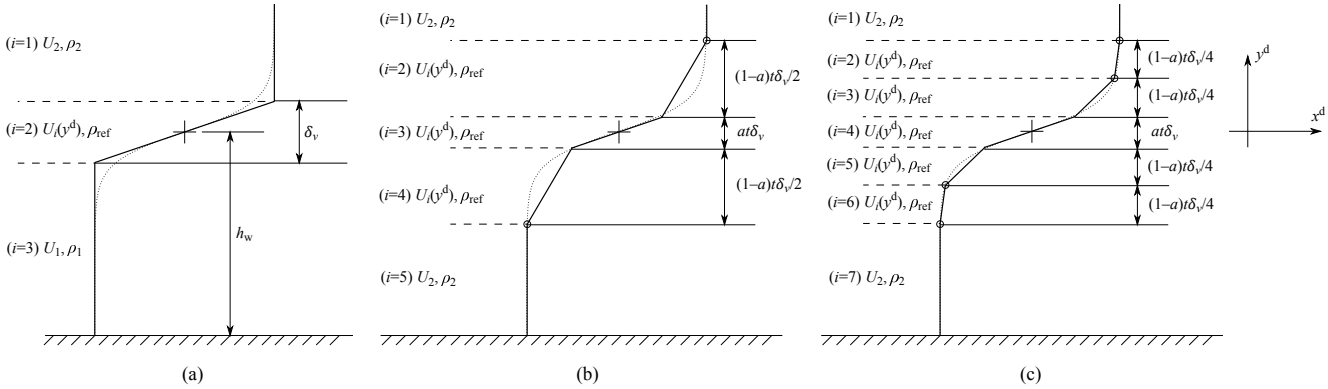

Figure 4.10: Velocity and density distribution in the wall-normal direction for a planar shear layer confined by a wall at $y^{\mathrm{d}} = -h_{\mathrm{w}}$ and unconfined in the direction $y^{\mathrm{d}} \to +\infty$. The velocity profile is approximated by (a) 1-piece, (b) 3-piece, and (c) 5-piece linear profiles. The density follows the plug profile with values ρ_1, ρ_2 in the outer flows and ρ_{ref} in the inner flow. The representation of the shear layer by a 'tanh' function is shown by dotted line. The small circles indicate the locations where the linear profile is concurrent with the 'tanh' profile.

be derived for the piecewise linear velocity profiles and compared with the results of the inviscid calculations performed by Groot *et al.* [9].

From the Fig. 4.10 and Fig. 4.11, the reference scales for length, velocity and density are defined as

$$L_{\mathrm{ref}} = \frac{\delta_{\mathrm{v}}}{2}\,, \tag{4.92}$$

$$U_{\mathrm{ref}} = \frac{\Delta U}{2} = \frac{U_2 - U_1}{2}\,, \tag{4.93}$$

$$\rho_{\mathrm{ref}} = \frac{\rho_1 + \rho_2}{2}\,, \tag{4.94}$$

where δ_{v} is the vorticity thickness defined in § 4.1.2. Also, the mean velocity used in Fig. 4.11 is given as $U_{\mathrm{m}} = (U_1 + U_2)/2$. The dimensionless variables can be then derived from the dimensional counterparts using the reference scales given as

$$c = \frac{c^{\mathrm{d}}}{U_{\mathrm{ref}}}, \quad k = k^{\mathrm{d}} L_{\mathrm{ref}}, \quad \xi = \xi^{\mathrm{d}} L_{\mathrm{ref}}, \quad \omega = \frac{\omega^{\mathrm{d}} L_{\mathrm{ref}}}{U_{\mathrm{ref}}}\,. \tag{4.95}$$

The dimensionless parameters are also given as

$$\Lambda = \frac{U_2 - U_1}{U_1 + U_2}\,, \tag{4.96}$$

$$S = \frac{\rho_2 - \rho_1}{\rho_1 + \rho_2}\,, \tag{4.97}$$

$$h = \frac{h_w}{\delta_{\mathrm{v}}/2}\,. \tag{4.98}$$

The base flow itself has been analytically characterised in several ways which allows the numerical implementation of profiles possible while preserving the physics of the flow. Meliga *et al.* [21] gave

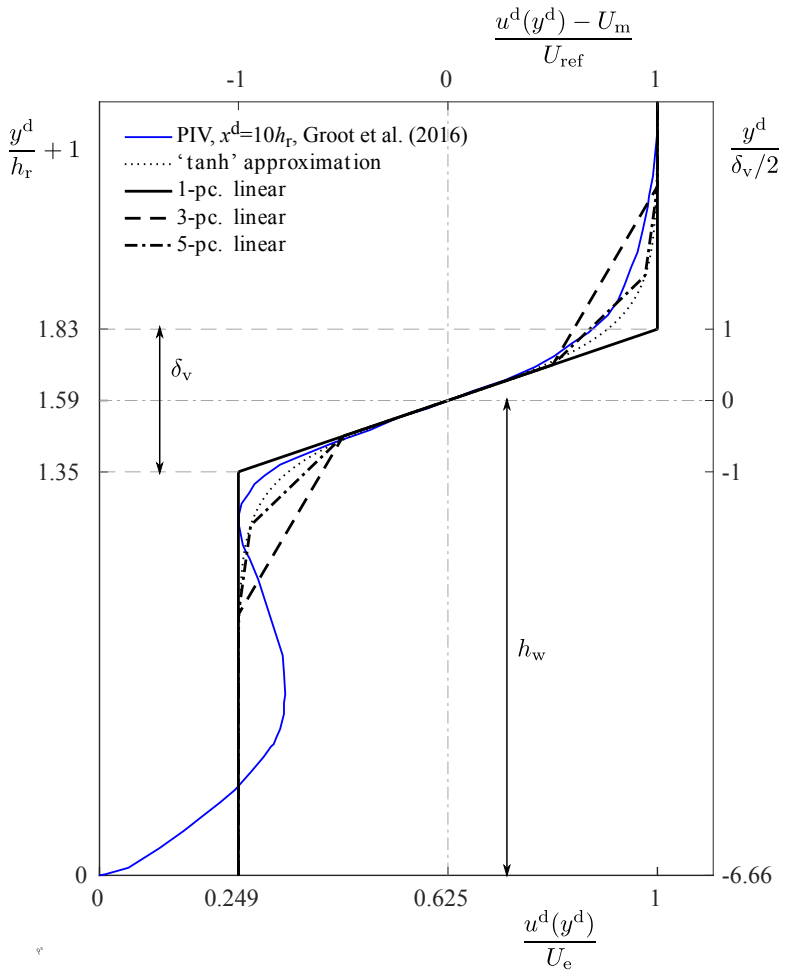

Figure 4.11: Velocity profiles to approximate the experimental base flow reported by Groot *et al.* [9] at a downstream distance of $x^{\mathrm{d}} = 10h_{\mathrm{r}}$ from the micro-ramp.

an algebraic representation of the jet/wake flows as

$$u(y) = 1 + \Lambda - \frac{2\Lambda}{1 + (2^{(y/h+1)^2} - 1)^{\eta}}\,, \tag{4.99}$$

where η is an integer value that controls the width of the shear layer. The base flow can also be represented in terms of an error function

$$u(y) = \mathrm{erf}\left(\frac{\sqrt{\pi}}{2}(y+h)\right)\,. \tag{4.100}$$

Lastly, Michalke [22] used the 'tanh' profile to study free jets as

$$u(y) = \frac{1}{\Lambda} + \tanh(y)\,. \tag{4.101}$$

Note that in the above profile definitions, the non-dimensional velocity $u = u^{\mathrm{d}}/U_{\mathrm{ref}}$ and length $y = y^{\mathrm{d}}/L_{\mathrm{ref}}$ has been used. In this chapter the 'tanh' profile will be considered in order to approximate the experimental base flow and to define the piecewise linear profiles.

4.3.2 Dispersion relation

The dispersion relations can be obtained analytically for the piecewise linear approximations to the 'tanh' profile. The derivation of the dispersion relations is similar to the ones used in the previous chapters, see *e.g.* § 4.1.2.1. For the 1-piece linear profile in Fig. 4.10(a), the eigenfunctions for the streams $i = 1$ to 3 are given as

$$\phi_1 = A_1 \mathrm{e}^{-\xi^{\mathrm{d}}(y^{\mathrm{d}} - \delta_{\mathrm{v}}/2)}\,, \tag{4.102}$$

$$\phi_2 = A_2 \mathrm{e}^{-\xi^{\mathrm{d}} y^{\mathrm{d}}} + B_2 \mathrm{e}^{+\xi^{\mathrm{d}} y^{\mathrm{d}}}\,, \tag{4.103}$$

$$\phi_3 = B_3 \sinh(\xi^{\mathrm{d}}(y^{\mathrm{d}} + h_{\mathrm{w}}))\,. \tag{4.104}$$

This and the subsequent eigenfunctions are chosen so as to satisfy the boundary conditions given in § 3.1.2.2. For the 3-piece linear profile in Fig. 4.10(b), the eigenfunctions for the streams $i = 1$ to 5 are given as

$$\phi_1 = A_1 \mathrm{e}^{-\xi^{\mathrm{d}}(y^{\mathrm{d}} - t\delta_{\mathrm{v}}/2)}\,, \tag{4.105}$$

$$\phi_2 = A_2 \mathrm{e}^{-\xi^{\mathrm{d}}(y^{\mathrm{d}} - at\delta_{\mathrm{v}}/2)} + B_2 \mathrm{e}^{+\xi^{\mathrm{d}}(y^{\mathrm{d}} - at\delta_{\mathrm{v}}/2)}\,, \tag{4.106}$$

$$\phi_3 = A_3 \mathrm{e}^{-\xi^{\mathrm{d}} y^{\mathrm{d}}} + B_3 \mathrm{e}^{+\xi^{\mathrm{d}} y^{\mathrm{d}}}\,, \tag{4.107}$$

$$\phi_4 = A_4 \cosh(\xi^{\mathrm{d}}(y^{\mathrm{d}} + at\delta_{\mathrm{v}}/2)) + B_4 \sinh(\xi^{\mathrm{d}}(y^{\mathrm{d}} + at\delta_{\mathrm{v}}/2))\,, \tag{4.108}$$

$$\phi_5 = B_5 \sinh(\xi^{\mathrm{d}}(y^{\mathrm{d}} + h_{\mathrm{w}}))\,. \tag{4.109}$$

Finally, for the 5-piece linear profile in Fig. 4.10(c), the eigenfunctions for the streams $i = 1$ to 7 are given as

$$\phi_1 = A_1 \mathrm{e}^{-\xi^{\mathrm{d}}(y^{\mathrm{d}} - t\delta_{\mathrm{v}}/2)}\,, \tag{4.110}$$

$$\phi_2 = A_2 \mathrm{e}^{-\xi^{\mathrm{d}}(y^{\mathrm{d}} - (1+a)t\delta_{\mathrm{v}}/4)} + B_2 \mathrm{e}^{+\xi^{\mathrm{d}}(y^{\mathrm{d}} - (1+1)t\delta_{\mathrm{v}}/4)}\,, \tag{4.111}$$

$$\phi_3 = A_3 \mathrm{e}^{-\xi^{\mathrm{d}}(y^{\mathrm{d}} - at\delta_{\mathrm{v}}/2)} + B_3 \mathrm{e}^{+\xi^{\mathrm{d}}(y^{\mathrm{d}} - at\delta_{\mathrm{v}}/2)}\,, \tag{4.112}$$

$$\phi_4 = A_4 \mathrm{e}^{-\xi^{\mathrm{d}} y^{\mathrm{d}}} + B_4 \mathrm{e}^{+\xi^{\mathrm{d}} y^{\mathrm{d}}}\,, \tag{4.113}$$

$$\phi_5 = A_5 \cosh(\xi^{\mathrm{d}}(y^{\mathrm{d}} + at\delta_{\mathrm{v}}/2)) + B_5 \sinh(\xi^{\mathrm{d}}(y^{\mathrm{d}} + at\delta_{\mathrm{v}}/2))\,, \tag{4.114}$$

$$\phi_6 = A_6 \cosh(\xi^{\mathrm{d}}(y^{\mathrm{d}} + (1+a)t\delta_{\mathrm{v}}/4)) + B_6 \sinh(\xi^{\mathrm{d}}(y^{\mathrm{d}} + (1+a)t\delta_{\mathrm{v}}/4))\,, \tag{4.115}$$

$$\phi_7 = B_7 \sinh(\xi^{\mathrm{d}}(y^{\mathrm{d}} + h_{\mathrm{w}}))\,. \tag{4.116}$$

The matching conditions at the interfaces can be used to obtain the dispersion relations for the three linear profiles. The final expression for the dispersion relations are given in matrix form in the Appendix C. The dispersion relations are 2^{nd}, 4^{th} and 6^{th} order in c for the 1-piece, 3-piece, and 5-piece linear profiles respectively.

4.3.3 Stability analysis

The higher order dispersion relations $\mathcal{D}(k, \omega)$ for the piecewise linear shear profiles produce multiple Riemann sheets in the complex k-space. As discussed earlier, each Riemann sheet corresponds to a solution c of the dispersion relation. The solution c for the 1-piece linear profile is easily obtained analytically as the dispersion relation is quadratic and the coefficients of c^n, where $n = 0, 1, 2,$

can be easily segregated. However, for the 3-piece and 5-piece linear profiles, the dispersion relation loses this conciseness, it becomes tedious to segregate the coefficients of c^n. To solve these equations, the fact that the solution c to the dispersion relations of the order higher than 2 remains bounded by the the solution to the second order dispersion relation is used. As we are only interested in the highest growth rate, calculating the upper and lower bounds of the solution for a given value of complex k is sufficient. For this purpose, MATLAB's `fsolve` function is used to obtain the solutions to the dispersion relations for 3-piece and 5-piece linear profiles by using the solution to the dispersion relation of the 1-piece linear profile at the corresponding value of k as the initial guess.

To validate the results, the temporal stability analysis is first performed for the piecewise linear profiles and results are compared with that from Groot *et al.* [9]. Later, the spatio-temporal analysis is also performed.

Temporal stability analysis

For the temporal stability analysis, the solutions to the dispersion relations of the piecewise linear profiles are calculated for the real values of wavenumber ($k \in \mathbb{R}$). The solutions are compared with the results of the inviscid 1-piece linear and inviscid 'tanh' profiles studied by Groot *et al.* [9]. The temporal branches are plotted in Fig. 4.12 and compared with the analytical and LST results from literature.

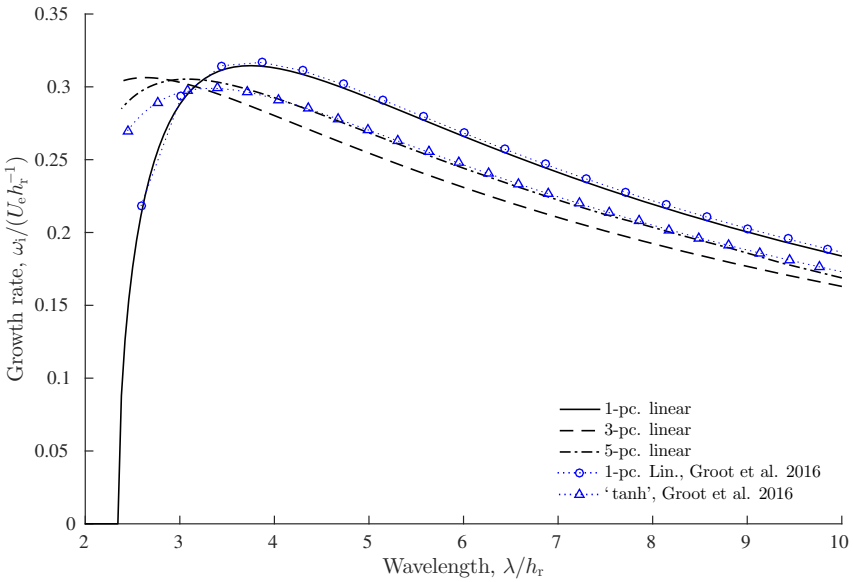

Figure 4.12: Temporal branches from the analytical dispersion relations compared with the results of Groot *et al.* [9].

It was determined by Groot *et al.* [9] that for the monochromatic perturbation, the maximum growth rate is associated with the wavelength of $(3.5 \pm 0.5)h_r$ in the downstream range of $x^d = 8h_r$ to $10h_r$. The temporal branch of the 1-piece linear profile matches the linear inviscid result of Groot *et al.* [9]. The comparison of the temporal branches for the 3-piece and 5-piece profiles with the results for the 'tanh' profile shows that the results converge towards the LST result as the number of linear pieces in the approximation increase. The temporal branch of the 5-piece profile shows

deviation from the 'tanh' profile result in the low wavelength range but shows excellent agreement in the higher wavelength range. The wavelengths associated with the maximum growth rate are all within the experimentally obtained range of $(3.5 \pm 0.5)h_{\mathrm{r}}$.

As the 1-piece linear profile offers the simplicity of analytical solution while approximating the behaviour of the experimental base flow, the subsequent section uses this profile to study the spatio-temporal behaviour.

Spatio-temporal stability analysis

The spatio-temporal stability analysis is performed for the 1-piece linear profile for the configuration shown in Fig. 4.11. The Riemann sheet for one of the solutions to the dispersion relation is shown in the Fig. 4.13. The saddle points are obtained near the k_{i}-axis owing to the appearance of the hyperbolic functions in the dispersion relation as a result of the confining wall. In the absence of surface tension, none of the saddle points is a valid pinch point. This implies that the shear flow confined by a wall on one side stays convectively unstable, as long as $\omega_{\mathrm{i}} > 0$ for the maximum temporal growth rate. A similar behaviour is encountered for the inhomogeneous shear layers.

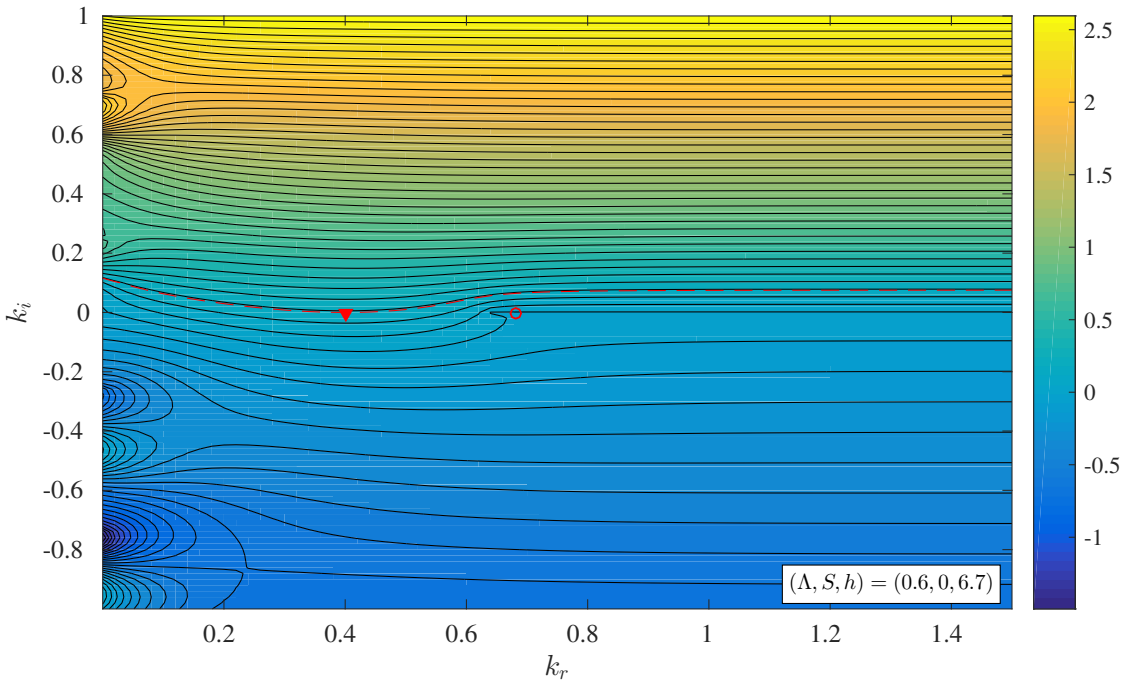

Figure 4.13: Contours of ω_{i} uniform density ($S = 0$) semi-unconfined shear layer approximated by a 1-piece linear profile. No valid pinch points are obtained for the given flow configuration. The saddles near the k_{i}-axis (say $s_{2\mathrm{a}}, s_{2\mathrm{b}}$, etc. in order from top to bottom) represent the column modes associated with the confinement. The position of the maximum growth rate predicted by temporal analysis is shown by a triangle.

4.3.4 Conclusion

The stability of a semi-unconfined shear layer has been studied in this chapter. The 1-piece linear profile approximation of the base flow predicts the wavelength associated with the maximum temporal growth rate in the same range as the experiment. However, the 5-piece linear profile matches the result of the inviscid 'tanh' profile in the large wavelength range. From the spatio-temporal analysis, it is concluded that the semi-unconfined shear layer is not absolutely unstable.

□

Chapter 5

Non-analytical models

From the study performed in the previous chapters, it is inferred that the simple models, with linear profiles for velocity and density along the wall normal direction, are able to capture the basic level of physics associated with a shear. The analytical solutions to the governing equations offer an advantage of obtaining closed form solutions to the dispersion relations. This allows the implementation of the instability criteria to a large range of parameter space inexpensively.

To incorporate more physics into the model, it is necessary to discard the linear profile approximations. This implies that the analytical dispersion relations can no longer be derived for such flows and the numerical approach must be adopted to solve the governing equations.

5.1 Validation case for shear flow

The semi-unconfined single shear layer discussed in § 4.3.2 will be studied for the purpose of validation of the numerical approach and to perform a convergence check for the computational parameters - domain length (L_d) and the number of spectral collocation points (N). The solution to the eigenvalue problem is sensitive to the choice of the parameters L_d and N. It is essential to verify the numerical solution by comparing it with analytical solution obtained *a priori* in order to correctly set the parameters that influence the solver performance.

The solution of the analytical dispersion relation for an arbitrary value of wavenumber k can be used as the target value that the numerical solution must approach. For current study, the analytical solution for the parameter set $(\Lambda, S, h) = (-3, 0, 225)$ at $k = 0.02 - 0.02\mathrm{i}$, given as

$$\omega = 0.0122737781478568 + 0.0266598592148586\mathrm{i}$$

is considered. One of the Riemann sheets corresponding to given parameter set and the eigenfunction, which corresponds to the amplitude of the wall normal perturbation velocity, are shown in Fig. 5.1.

For the numerical counterpart, the spatio-temporal analysis begins with the selection of the most unstable mode from the spectrum of eigenmodes. The spectrum corresponding to the parameter set

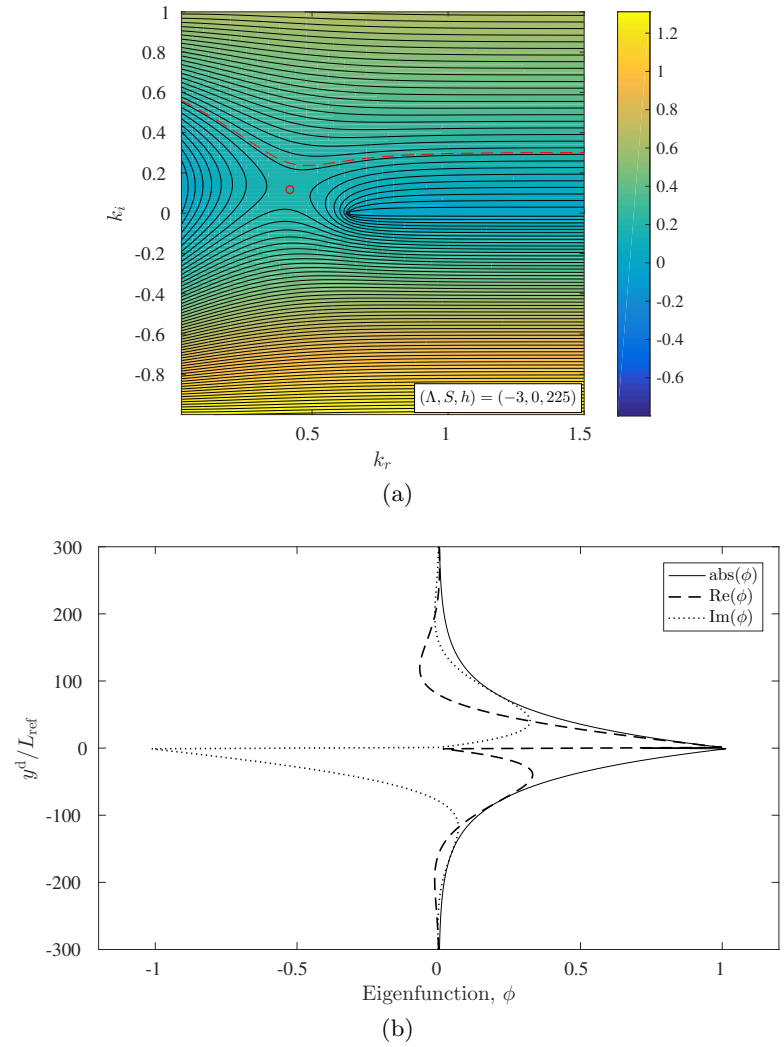

Figure 5.1: (a) Contours of constant ω_{i} in k-plane for an semi-unconfined single shear layer flow, and (b) eigenfunction corresponding to the wall normal velocity perturbation at wavenumber $k = 0.02 - 0.02\mathrm{i}$.

$(\Lambda, S, h) = (-3, 0, 225)$ at $k = 0.02 - 0.02\mathrm{i}$ is shown in Fig. 5.2. The spectrum contains two distinct types of modes – the *continuous spectra* corresponding to the outer flows and the *discrete modes* corresponding to the inner flow which includes the shear layer. The discrete modes obtained here are the non-spurious modes that are the solutions to the numerical dispersion relation. Further, it is seen that only one of these discrete modes lies in the unstable $\omega_{\mathrm{i}} > 0$ half plane. The eigenfunctions corresponding to this mode is shown in Fig. 5.2(b). It can be seen that the shape of the eigenfunction for the wall normal velocity perturbation matches the one obtained from the analytical dispersion relation, as shown in Fig. 5.1(b).

The collocation dependence of solution is studied first by fixing the domain length L_{d} and varying the number of collocation points. The solutions, or the eigenvalues, obtained from the spectral calculations is listed in Table 5.1. As we are interested in the growth rate of the perturbations, it is sufficient for the current study to focus on the convergence of the imaginary part of the frequency (ω_{i}). It is observed that, using the Chebyshev collocation method, the convergence to the fourth

decimal place is reached in few steps. But as the number of nodes increases, the solution oscillates which prevents the convergence up to higher decimal places.

Table 5.1: Eigenvalue for the semi-unconfined single shear layer flow for the parameters $(\Lambda, S, h) = (-3, 0, 225)$ at $k = 0.02 - 0.02\mathrm{i}$, $L_\mathrm{d} = 390$.

$N+1$	ω
51	0.0128142081559752 + 0.0236475682649652i
101	0.0124313027961779 + 0.0255915591025048i
151	0.0123337145233326 + 0.0266332136422957i
201	0.0122402879698834 + 0.0266712790020062i
301	0.0122300466612902 + 0.0266097081813941i

Next, the influence of the domain length for a fixed number of collocation nodes is studied next. The calculated eigenvalues from the convergence study are shown in Table 5.2. Again, focusing on the imaginary part of the eigenvalue, it is observed that the solution converges up to the fourth decimal place as L_d increases, and then starts oscillating. The importance of selecting the right domain length can be seen from the eigenfunction plots in Fig. 5.2(b). If the domain length is too short, the eigenfunction does not decay to zero, which violates the boundary conditions. For the current case, with $\xi_\mathrm{r} = 0.02$ and $L_\mathrm{d} = 400$, an approximation to the order of magnitude of the eigenfunction at the boundaries can be obtained as $\exp(-\xi^\mathrm{d} L_\mathrm{d}/2) \approx \mathcal{O}(10^{-6})$.

Table 5.2: Eigenvalue for the semi-unconfined single shear layer flow for the parameters $(\Lambda, S, h) = (-3, 0, 225)$ at $k = 0.02 - 0.02\mathrm{i}$, $N + 1 = 151$.

L_d	ω
100	0.0121443706955975 + 0.0268628730307754i
200	0.0118350612641270 + 0.0266586623453859i
300	0.0126698427748996 + 0.0270006375294625i
400	0.0125631711622492 + 0.0268894996821126i

5.2 Solutions to smooth shear layer profiles

The main advantage offered by the numerical tool is that it allows the application of the stability criteria to identify convective/absolute transition boundary, developed in the previous chapters, to the physical flows. In this regard, the results of the temporal analysis performed on the piecewise linear approximations of the experimental base flow in § 4.3 will be compared with the results obtained from the numerical calculations. Next, the smooth shear layer profiles discussed in introduced in § 4.3.1 will be solved using the numerical tool and the results will be compared with the one reported by Groot *et al.* [9].

The numerical solution matches the analytical solution for a significant range of wavelengths as shown in Fig. 5.3. The deviation in the small wavelength range is only because of the discretisation of the k-space for obtaining the analytical solution, an artefact that is not present in the numerical solution. Moreover, the maximum temporal growth rate is also correctly captured by the numerical temporal branch. This comparison acts as a validation that the numerical tool can be applied to smooth profiles for more physical solutions.

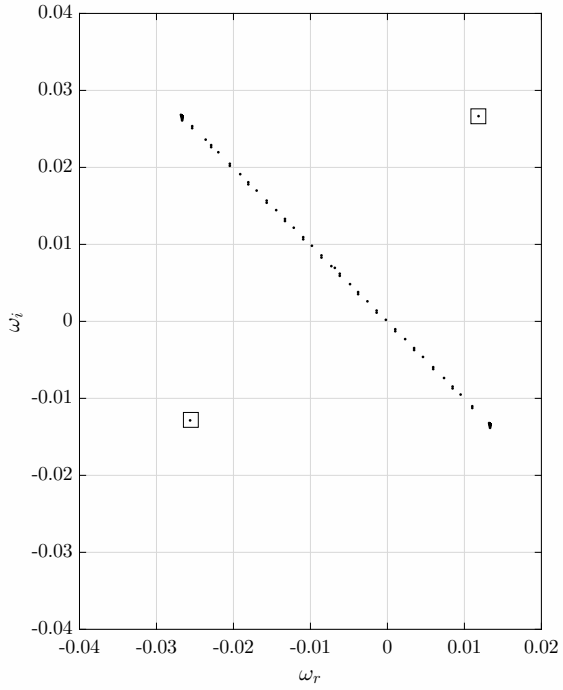

(a)

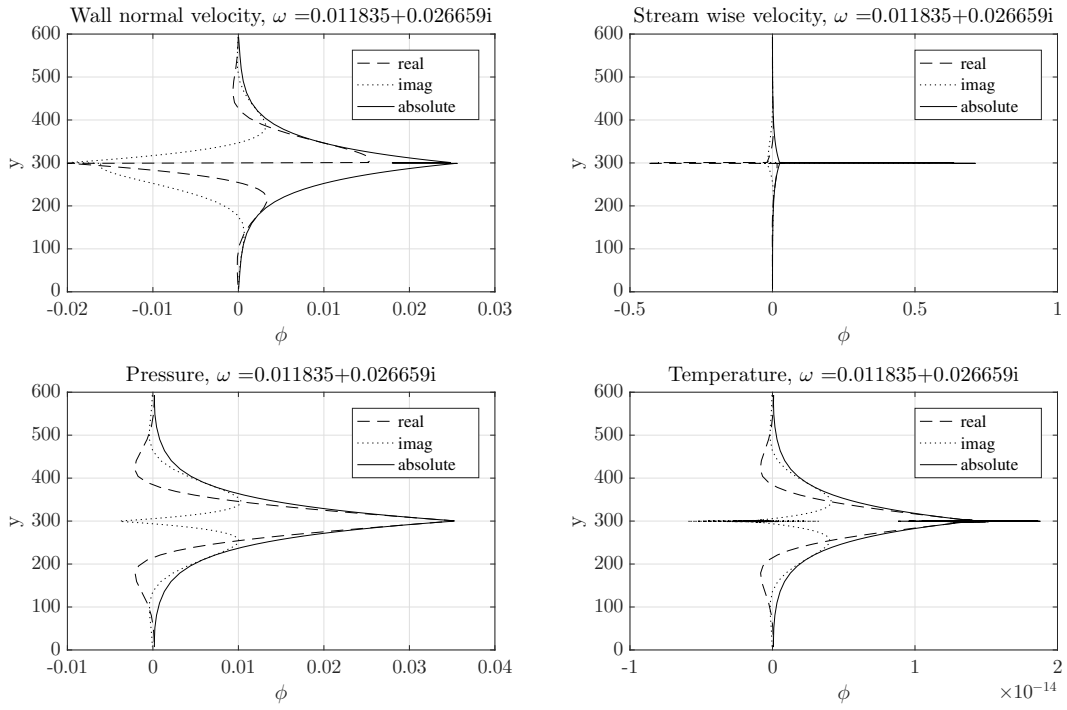

(b)

Figure 5.2: (a) Spectrum showing the eigenmodes for the unconfined single shear layer flow at $(\Lambda, S, h) = (-3, 0, 225)$, $k = 0.02 - 0.02\mathrm{i}$. The squares bound the discrete modes. (b) Eigenfunctions corresponding to the most unstable mode selected from the spectrum in (a).($L_\mathsf{d} = 390, N + 1 = 151$)

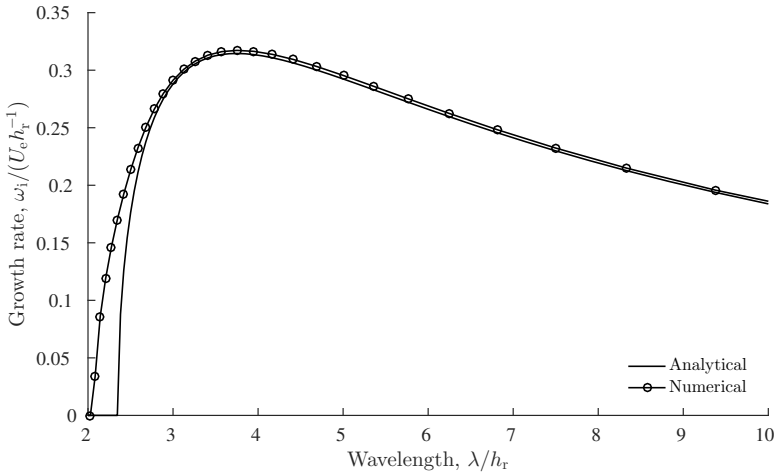

Figure 5.3: Comparison of temporal branches calculated using the analytical dispersion relation with the numerical solution ($L_d = 460, N + 1 = 151$).

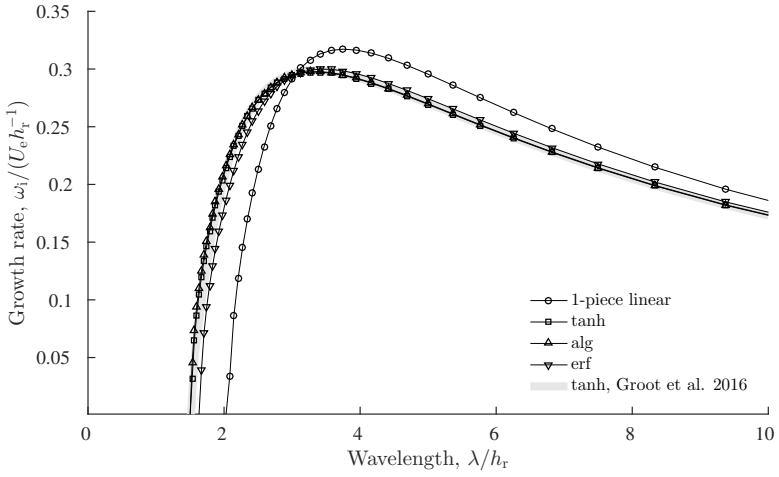

Figure 5.4: Comparison of temporal branches for the 1-piece linear, 'tanh', algebraic, and error-function approximations of the experimental base flow obtained from the numerical tool ($L_d = 460, N + 1 = 151$).

As shown in Fig. 5.4, the temporal branches for the 'tanh', algebraic, and error-function profiles – that approximate the experimental base flow discussed in § 4.3.1 – match with the temporal branch of the inviscid 'tanh' profile solution reported by Groot *et al.* [9]. The smooth profiles are chosen such as the vorticity thickness δ_ω remains same as that of the experimental base flow. For the algebraic profile, this requires $\eta = 2h/\log(2)$.

5.3 Conclusion

The numerical tools in VESTA have been implemented to study the stability of the semi-unconfined shear layer and the results are validated against the analytical solutions. The numerical solution can be extended to smooth approximations of the physical mean flow profile to produce the convective/absolute transition boundaries using the tools developed for piecewise linear profiles.

□

Chapter 6

Convective/Absolute instability transition boundary

6.1 Saddle point and Convective-Absolute Instability Boundary

The implementation of the analytical dispersion relation $\mathcal{D}(k, \omega)$ will be described in this section.

The saddle point $(k_\mathrm{s}, \omega_\mathrm{s})$ can be evaluated by satisfying Eq. 2.31. In the current form, the two complex equations have two complex variables k and ω. The real and imaginary parts can be considered individually which gives four real equations in terms of four variables $k_\mathrm{r}, k_\mathrm{i}, \omega_\mathrm{r}, \omega_\mathrm{i}$. This way of splitting the complex equation gives independent control over the tolerance of the solutions to the real and imaginary equations.

The solution to Eq. 2.31 is obtained iteratively from a suitable initial guess (k_0, ω_0) using the Newton-Raphson scheme. The root-search function `fsolve` from MATLAB's Optimisation Toolbox has been used to solve the system of equations, allowing an maximum absolute tolerance of 10^{-8}.

The saddle points are formed by the pinching of k-branches as described in §2.3. The pinch points are distinctly identifiable form the contour plots of ω_i or ω_r in the complex-k space. The pinch point lies in the region where two hills meet two adjacent valleys, with one hill extending in the upper half k-plane and the other hill extending in the lower half k-plane.

The saddle point (k_{0s}, ω_{0s}) is located for an initial parameter $R_0 = (r_{10}, r_{20})$ such that the dispersion relation given by Eq. 1.3 is satisfied. To determine the convective-absolute instability boundary (CAIB), the saddle point must be tracked in the parameter space $R = (r_1, r_2)$. The methodology adopted by Rees [26] will be discussed here. The CAIB is given by the locations in the k-space where the temporal growth rate is zero

$$\omega_{s,i}(r_1, r_2) = 0\,. \tag{6.1}$$

For analytical dispersion relations, the higher derivatives can be calculated *a priori*. This allows for the parametrisation of solution with a parametric variable τ. For the dispersion relation

$\mathcal{D}(k(\tau),\omega(\tau);R)$, where $k,\omega\in\mathbb{C}$, the saddle point equation Eq. 2.31 can be expressed as

$$\begin{aligned}\mathcal{D}(k_{\mathrm{r}}(\tau),k_{\mathrm{i}}(\tau),\omega_{\mathrm{r}}(\tau),\omega_{\mathrm{i}}(\tau),r_1(\tau),r_2(\tau))&=0\,,\\ \mathcal{D}_k(k_{\mathrm{r}}(\tau),k_{\mathrm{i}}(\tau),\omega_{\mathrm{r}}(\tau),\omega_{\mathrm{i}}(\tau),r_1(\tau),r_2(\tau))&=0\,.\end{aligned}\tag{6.2}$$

The equations must hold for all τ and therefore, it must satisfy

$$\begin{aligned}\frac{\mathrm{d}\mathcal{D}}{\mathrm{d}\tau}(k_{\mathrm{r}}(\tau),k_{\mathrm{r}}(\tau),\omega_{\mathrm{r}}(\tau),\omega_{\mathrm{i}}(\tau),r_1(\tau),r_2(\tau))&=0\,,\\ \frac{\mathrm{d}\mathcal{D}_k}{\mathrm{d}\tau}(k_{\mathrm{r}}(\tau),k_{\mathrm{i}}(\tau),\omega_{\mathrm{r}}(\tau),\omega_{\mathrm{i}}(\tau),r_1(\tau),r_2(\tau))&=0\,.\end{aligned}\tag{6.3}$$

As $k=k_{\mathrm{r}}+\mathrm{i}k_{\mathrm{i}}$ and $\omega=\omega_{\mathrm{r}}+\mathrm{i}\omega_{\mathrm{i}}$, we have

$$\frac{\partial\omega}{\partial\omega_{\mathrm{r}}}=1,\ \frac{\partial\omega}{\partial\omega_{\mathrm{i}}}=\mathrm{i},\ \frac{\partial k}{\partial k_{\mathrm{r}}}=1,\ \frac{\partial k}{\partial k_{\mathrm{i}}}=\mathrm{i}\,,\tag{6.4}$$

which gives

$$\begin{aligned}\frac{\mathrm{d}\mathcal{D}}{\mathrm{d}\tau}&=\mathcal{D}_k\frac{\mathrm{d}k_{\mathrm{r}}}{\mathrm{d}\tau}+\mathrm{i}\mathcal{D}_k\frac{\mathrm{d}k_{\mathrm{i}}}{\mathrm{d}\tau}+\mathcal{D}_\omega\frac{\mathrm{d}\omega_{\mathrm{r}}}{\mathrm{d}\tau}+\mathrm{i}\mathcal{D}_\omega\frac{\mathrm{d}\omega_{\mathrm{i}}}{\mathrm{d}\tau}+\mathcal{D}_{r_1}\frac{\mathrm{d}r_1}{\mathrm{d}\tau}+\mathcal{D}_{r_2}\frac{\mathrm{d}r_2}{\mathrm{d}\tau}=0\,,\\ \frac{\mathrm{d}\mathcal{D}_k}{\mathrm{d}\tau}&=\mathcal{D}_{kk}\frac{\mathrm{d}k_{\mathrm{r}}}{\mathrm{d}\tau}+\mathrm{i}\mathcal{D}_{kk}\frac{\mathrm{d}k_{\mathrm{i}}}{\mathrm{d}\tau}+\mathcal{D}_{k\omega}\frac{\mathrm{d}\omega_{\mathrm{r}}}{\mathrm{d}\tau}+\mathrm{i}\mathcal{D}_{k\omega}\frac{\mathrm{d}\omega_{\mathrm{i}}}{\mathrm{d}\tau}+\mathcal{D}_{kr_1}\frac{\mathrm{d}r_1}{\mathrm{d}\tau}+\mathcal{D}_{kr_2}\frac{\mathrm{d}r_2}{\mathrm{d}\tau}=0\,.\end{aligned}\tag{6.5}$$

The real and imaginary parts of Eq. 6.5 give the four equations for the six unknowns. As the problem is ill-posed, two additional equations are required.

In non-trivial cases, the initial choice of parameters (r_{10},r_{20}) will not give a saddle point that satisfies Eq. 6.1. Therefore, firstly, it is required to track the saddle point until the growth rate becomes zero. This gives one of the two additional parametric equations

$$\frac{\mathrm{d}\omega_{\mathrm{i}}}{\mathrm{d}\tau}=1\quad\text{or}\quad\frac{\mathrm{d}\omega_{\mathrm{i}}}{\mathrm{d}\tau}=-\omega_{s0,i}\,.\tag{6.6}$$

The first equation above characterises ω_{i} with respect to τ. As the change in τ requires equivalent change in ω_{i}, the parametric curve must be traversed over the interval $\tau\in[0,\omega_{s0,i}]$ for locating the CAIB. The second equation is just a normalised version of first equation where the parametric curve is traversed over the interval $\tau\in[0,1]$.

The last additional equation is given by considering the conservation of one of the variables $(k_{\mathrm{r}},k_{\mathrm{i}},\omega_{\mathrm{r}},r_1,r_2)$ as the parametric curve is traversed. As the CAIB lies in the (r_1,r_2)-plane, the last equation can be given by either of the following expressions

$$\frac{\mathrm{d}r_1}{\mathrm{d}\tau}=0\quad\text{or}\quad\frac{\mathrm{d}r_2}{\mathrm{d}\tau}=0\,.\tag{6.7}$$

The system of parametric equations Eq. 6.5, Eq. 6.6 and Eq. 6.7 can be written in matrix form as

$$\begin{bmatrix}(\mathcal{D}_k)_{\mathrm{r}} & -(\mathcal{D}_k)_{\mathrm{i}} & (\mathcal{D}_\omega)_{\mathrm{r}} & -(\mathcal{D}_\omega)_{\mathrm{i}} & (\mathcal{D}_{r_1})_{\mathrm{r}} & (\mathcal{D}_{r_2})_{\mathrm{r}}\\ (\mathcal{D}_k)_{\mathrm{i}} & (\mathcal{D}_k)_{\mathrm{r}} & (\mathcal{D}_\omega)_{\mathrm{i}} & (\mathcal{D}_\omega)_{\mathrm{r}} & (\mathcal{D}_{r_1})_{\mathrm{i}} & (\mathcal{D}_{r_2})_{\mathrm{i}}\\ (\mathcal{D}_{kk})_{\mathrm{r}} & -(\mathcal{D}_{kk})_{\mathrm{i}} & (\mathcal{D}_{k\omega})_{\mathrm{r}} & -(\mathcal{D}_{k\omega})_{\mathrm{i}} & (\mathcal{D}_{kr_1})_{\mathrm{r}} & (\mathcal{D}_{kr_2})_{\mathrm{r}}\\ (\mathcal{D}_{kk})_{\mathrm{i}} & (\mathcal{D}_{kk})_{\mathrm{r}} & (\mathcal{D}_{k\omega})_{\mathrm{i}} & (\mathcal{D}_{k\omega})_{\mathrm{r}} & (\mathcal{D}_{kr_1})_{\mathrm{i}} & (\mathcal{D}_{kr_2})_{\mathrm{i}}\\ 0 & 0 & 0 & 1 & 0 & 0\\ 0 & 0 & 0 & 0 & 0\text{ or }1 & 1\text{ or }0\end{bmatrix}\begin{bmatrix}\frac{\mathrm{d}k_{\mathrm{r}}}{\mathrm{d}\tau}\\ \frac{\mathrm{d}k_{\mathrm{i}}}{\mathrm{d}\tau}\\ \frac{\mathrm{d}\omega_{\mathrm{r}}}{\mathrm{d}\tau}\\ \frac{\mathrm{d}\omega_{\mathrm{i}}}{\mathrm{d}\tau}\\ \frac{\mathrm{d}r_1}{\mathrm{d}\tau}\\ \frac{\mathrm{d}r_2}{\mathrm{d}\tau}\end{bmatrix}=\begin{bmatrix}0\\0\\0\\0\\1\\0\end{bmatrix}\,.\tag{6.8}$$

When the saddle point is tracked, the values of $\mathbf{v} = (k_\mathrm{r}, k_\mathrm{i}, \omega_\mathrm{r}.\omega_\mathrm{i}, r_1, r_2)^\mathrm{T}$ are initialised for any given parametric value. Then the coefficient matrix in Eq. 6.8 is taken to the RHS to give the differentials as

$$\frac{\mathrm{d}\mathbf{v}}{\mathrm{d}\tau} = \mathbf{F}(\mathbf{v}, \tau)\,. \tag{6.9}$$

The solution $\mathbf{v}$ is obtained by numerical integration of Eq. 6.9. This serves as the initial condition $\mathbf{v}_0$ for the next step where the growth rate of the saddle point is brought to zero such that it lies on the CAIB. As the growth rate is invariant, we get

$$\frac{\mathrm{d}\omega_\mathrm{i}}{\mathrm{d}\tau} = 0\,. \tag{6.10}$$

The additional equation is given by the rate of traverse of the parameter space by the flow parameters

$$\frac{\mathrm{d}r_1}{\mathrm{d}\tau} = \pm 1 \quad \text{or} \quad \frac{\mathrm{d}r_2}{\mathrm{d}\tau} = \pm 1\,. \tag{6.11}$$

The system of parametric equations Eq. 6.5, Eq. 6.10 and Eq. 6.11 can be written in matrix form as

$$\begin{bmatrix} (\mathcal{D}_k)_\mathrm{r} & -(\mathcal{D}_k)_\mathrm{i} & (\mathcal{D}_\omega)_\mathrm{r} & -(\mathcal{D}_\omega)_\mathrm{i} & (\mathcal{D}_{r_1})_\mathrm{r} & (\mathcal{D}_{r_2})_\mathrm{r} \\ (\mathcal{D}_k)_\mathrm{i} & (\mathcal{D}_k)_\mathrm{r} & (\mathcal{D}_\omega)_\mathrm{i} & (\mathcal{D}_\omega)_\mathrm{r} & (\mathcal{D}_{r_1})_\mathrm{i} & (\mathcal{D}_{r_2})_\mathrm{i} \\ (\mathcal{D}_{kk})_\mathrm{r} & -(\mathcal{D}_{kk})_\mathrm{i} & (\mathcal{D}_{k\omega})_\mathrm{r} & -(\mathcal{D}_{k\omega})_\mathrm{i} & (\mathcal{D}_{kr_1})_\mathrm{r} & (\mathcal{D}_{kr_2})_\mathrm{r} \\ (\mathcal{D}_{kk})_\mathrm{i} & (\mathcal{D}_{kk})_\mathrm{r} & (\mathcal{D}_{k\omega})_\mathrm{i} & (\mathcal{D}_{k\omega})_\mathrm{r} & (\mathcal{D}_{kr_1})_\mathrm{i} & (\mathcal{D}_{kr_2})_\mathrm{i} \\ 0 & 0 & 0 & 1 & 0 & 0 \\ 0 & 0 & 0 & 0 & 0/1 & 1/0 \end{bmatrix} \begin{bmatrix} \frac{\mathrm{d}k_\mathrm{r}}{\mathrm{d}\tau} \\ \frac{\mathrm{d}k_\mathrm{i}}{\mathrm{d}\tau} \\ \frac{\mathrm{d}\omega_\mathrm{r}}{\mathrm{d}\tau} \\ \frac{\mathrm{d}\omega_\mathrm{i}}{\mathrm{d}\tau} \\ \frac{\mathrm{d}r_1}{\mathrm{d}\tau} \\ \frac{\mathrm{d}r_2}{\mathrm{d}\tau} \end{bmatrix} = \begin{bmatrix} 0 \\ 0 \\ 0 \\ 0 \\ 0 \\ \pm 1 \end{bmatrix}\,. \tag{6.12}$$

As the parameters (r_1, r_2) are functions of τ only, the integration domain with respect to τ can be chosen such that the upper and lower bounds of the (r_1, r_2)-space are traversed.

6.2 Unconfined single vortex sheet

From Eq. 4.18, it is observed that the growth rate ω_i is characterised by the quantity $Q \equiv 2\Lambda S(2\Lambda S + 1) - 3\Lambda^2 + 1$. For $Q > 0$, the quantities c, k and ω are real and the saddle point will be located on the real k-axis with $\omega_\mathrm{i} = 0$. When $Q < 0$, the saddle point is situated at a location with (possibly) complex k-value with $\omega_\mathrm{i} > 0$; spatio-temporal instability. The convective/absolute transition occurs when $Q = 0$, which gives

$$\frac{1}{3}\left(\frac{1}{\Lambda} + S\right)^2 + S^2 = 1\,, \tag{6.13}$$

which has a shape of the ellipse in the parametric space $(1/\Lambda, S)$ as shown in Fig. 6.1.

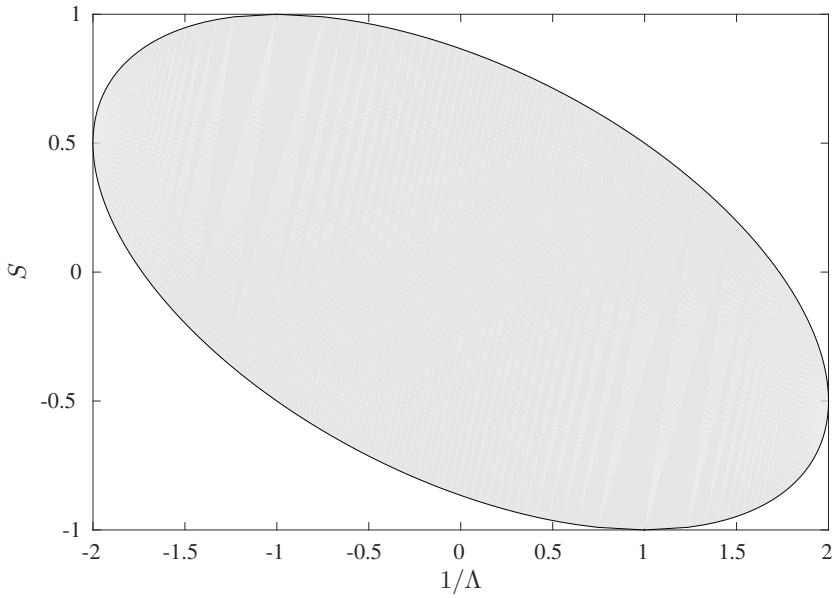

Figure 6.1: Absolutely unstable region (grey) of an unconfined vortex sheet with surface tension as a function of shear Λ, and density ratio S.

6.3 Inviscid planar jets and wakes

6.3.1 Effect of density (S), shear (Λ), and surface tension (Σ) for unconfined jet/wake flows

The conventional spatio-temporal stability analysis is performed to estimate the regions of absolute instability in the parameter space. The region is formed by the convective-absolute instability boundary (CAIB) which is obtained by following the procedure explained in § 6.1.

The varicose and sinuous dispersion relations in the limit of unconfined double shear layer flow can be obtained from Eq. 4.70 and Eq. 4.71 as

$$(1-S)(1/\Lambda-1-c)^2\coth(\xi/\Sigma)+(1+S)(1/\Lambda+1-c)^2-\xi=0\,,\ \text{and} \tag{6.14}$$

$$(1-S)(1/\Lambda-1-c)^2\tanh(\xi/\Sigma)+(1+S)(1/\Lambda+1-c)^2-\xi=0\,, \tag{6.15}$$

where the fact that $h\to 1$ and $h_{\text{ref}}\to h_1$ as $h_2\to\infty$ has been used. The Fig. 6.2 shows the CAIB in the $(1/\Lambda, S)$-space. The simply connected boundary is obtained by following the most dominant saddle point (s_1) as the parameter S assumes discrete values and value of parameter $1/\Lambda$ is calculated such that the saddle point represents marginally stable mode, *i.e.*, $\omega_{\text{i}}=0$.

The Fig. 6.3 shows the variation of the CAIB with the surface tension Σ. At low surface tensions, the wavelength of the most unstable mode is very small compared to the distance between the shear layers and therefore the shear layers do not interact. The instability is governed by the single shear layers which is evident from the CAIB for both varicose and sinuous perturbations at $\Sigma=0.1$ which is identical to the CAIB obtained for single shear layer Fig. 6.1.

As surface tension Σ increases, the absolutely unstable region shifts to low density (S) region for varicose perturbations while it shifts to higher density region for sinuous perturbations.

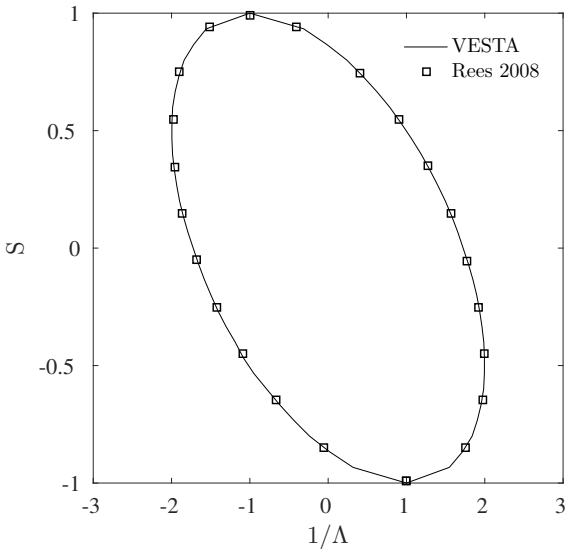

Figure 6.2: CAIB for varicose perturbations of an unconfined jet/wake flow at $\Sigma = 0.1$. The computed values are compared against the values obtained by Rees [26] after the transformation $1/\Lambda \to -1/\Lambda$ and $S \to -S$.

The value of Σ at which the surface tension starts to influence the stability of the jet/wake column mode is predictable analytically. For low values of Σ, the s_2-saddles are clustered in the vicinity of the k_i-axis and far from the dominant s_1-saddle, as seen from Fig. 4.9. As the value of Σ increases, the column modes move away from the k_i-axis and starts interacting with the dominant s_1-saddle. From the analytical dispersion relation and following the same procedure as in § 4.2.3 for the current unconfined case ($h = 1$), we obtain the limit that the two modes start interacting when $\Sigma \gtrsim 8(1/\Lambda + S)^2/9$. From Fig. 6.3, it can be seen that for $S \sim 0$ and $\Sigma = 1$, the transition boundary matches with that for the single shear layer. This is because for $|1/\Lambda| > 0$, we have $8(1/\Lambda + S)^2/9 > 1$, which means that there is no interaction of the modes. On the other hand, for $|S| \sim 1$, the transition boundaries are not same as that for the single shear layer. As $|1/\Lambda| \sim 1$, $|(1/\Lambda + S)| \sim 1$ and $8(1/\Lambda + S)^2/9 < 1$. For values of $\Sigma \geq 1$, therefore, the modes interact and the transition boundary deviates from that obtained for the single shear layer. The deviation is negligible for $\Sigma = 0.1$ and it gets significant as the parameter value Σ increases.

6.3.2 Effect of confinement (h), density (S), shear (Λ), and surface tension (Σ) for unconfined jet/wake flows

In this section, the conventional spatio-temporal analysis will be used to estimate the CAIB in the $(1/\Lambda, h)$-space for discrete values of density (S) and surface tension (Σ) parameters. The value covers a range from the weak surface tension limit ($\Sigma \to 0$), where the single shear layer instability is the dominating phenomenon, to the strong surface tension regime ($\Sigma \to \infty$), where the shear layers interact.

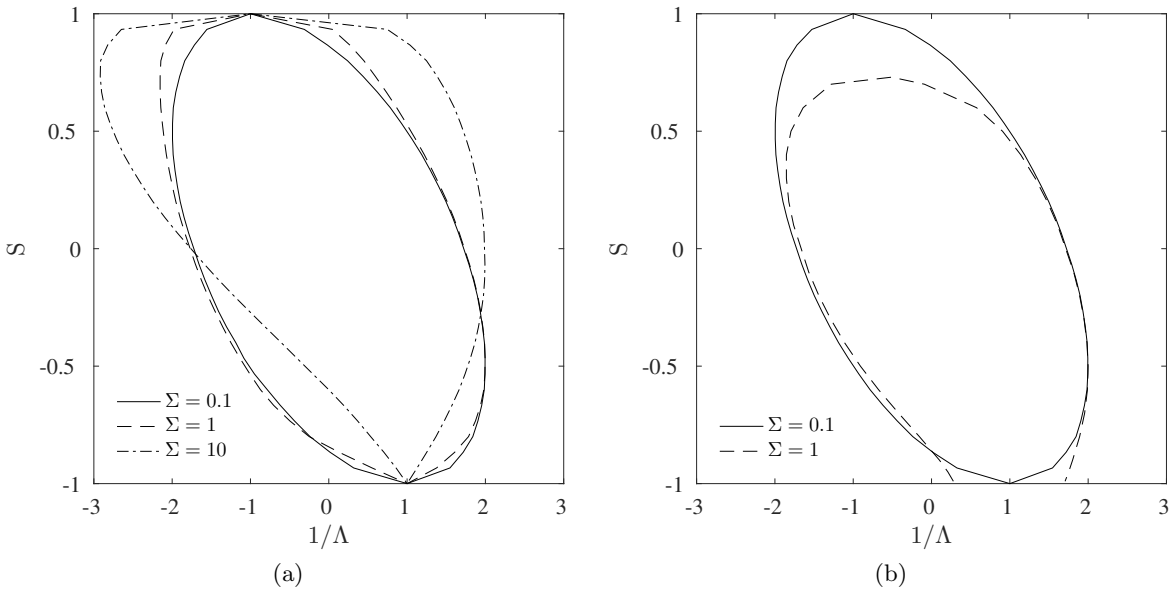

Figure 6.3: CAIB for varicose (a) and sinuous (b) perturbations of an unconfined jet/wake flow at discrete values of surface tension Σ. The boundary in the $(1/\Lambda, S)$-plane is simply connected. The region inside the boundary indicates absolute instability while the region outside the boundary represents convective instability.

6.3.2.1 Strong surface tension limit

When $\Sigma \gg 1$, the surface tension forces dominate over the inertial forces. The small wavelength disturbances are strongly stabilised. The unstable wavelengths are therefore of order L_{ref}, which are much larger than the scale of confinement h_{ref}. In this limit, the hyperbolic terms in the dispersion relations Eq. 4.70 and Eq. 4.71 can be approximated by the leading order term in the Taylor expansion, as given by Eq. 4.76 and Eq. 4.77.

For the varicose perturbations, Eq. 4.70 is simplified to the algebraic form as

$$\mathcal{D}(k,\omega) = \frac{\Sigma(1+h)(1-S)(1/\Lambda - 1 - c)^2}{2\xi} + \frac{\Sigma(1-h)(1+S)(1/\Lambda + 1 - c)^2}{2\xi} - \xi\,. \tag{6.16}$$

The first two terms in Eq. 6.16 represent the pressure fluctuations in the inner and outer flows while the third term represents the pressure jump across the interface due to surface tension. As seen, both the terms are $\mathcal{O}(\Sigma)$. Therefore, at long wavelengths (small ξ), the two terms are large enough to overcome the strong surface tension and are therefore responsible for sustaining the oscillations at the interface.

The range of wavenumbers for which the unconfined varicose flow is unstable can be rewritten from Eq. 4.78 as

$$0 < k < \sqrt{\frac{(1-h^2)(1-S^2)\Sigma}{1-hS}}\,. \tag{6.17}$$

Therefore, the flow is stable for the values of $S = \pm 1$ or $h = \pm 1$. In dimensional framework, the range of unstable wavenumbers scales with $\sigma^{-1/2}$ as $k^{\text{d}} = k/L_{\text{ref}}$. Thus, the stability results at high Σ differ from the ones at low Σ in which k scales with σ^{-1}.

For the unconfined single shear layer, the reference density is formulated as $\rho_{\text{ref}} = (\rho_1 + \rho_2)/2$, which allows the fact that the denser stream has dominant influence on the velocity of the unstable wavepacket. In strong surface tension limit, the unstable modes have wavelengths that are larger than the width of either streams. Therefore, the confining walls and neighbouring shear layer influence the perturbation behaviour, as also seen in § 4.2.3. The dominant stream in this case is determined from the weighted density with respect to the width of the streams. The new reference density is given as

$$\rho'_{\text{ref}} = \left(\frac{\rho_1}{h_1} + \frac{\rho_2}{h_2}\right)\frac{h'_{\text{ref}}}{2}\,, \tag{6.18}$$

where, the new reference width scale h'_{ref} is given as the geometric mean of the two stream widths

$$h'_{\text{ref}} = (h_1 h_2)^{1/2}\,. \tag{6.19}$$

The reference length scale is also given as the geometric mean of h'_{ref} and the surface tension length scale.

$$L'_{\text{ref}} = \left(\frac{h'_{\text{ref}}\sigma}{\rho'_{\text{ref}}U^2_{\text{ref}}}\right)^{1/2}\,. \tag{6.20}$$

The dimensionless variables are given as

$$c' = \frac{c^{\text{d}}}{U_{\text{ref}}}, \quad k' = k^{\text{d}}L'_{\text{ref}}, \quad \xi' = \xi^{\text{d}}L'_{\text{ref}}, \quad \omega' = \frac{\omega^{\text{d}}L'_{\text{ref}}}{U_{\text{ref}}}\,. \tag{6.21}$$

The dimensionless parameter in terms of the weighted densities is given as

$$S' = \frac{\rho_2/h_2 - \rho_1/h_1}{\rho_2/h_2 + \rho_1/h_1} = \frac{S-h}{1-Sh}\,. \tag{6.22}$$

The dispersion relation for varicose perturbations in the strong surface tension limit given by Eq. 6.16 is given in terms of the new reference scales and parameters as

$$\mathcal{D}' = (1-S')(1/\Lambda - 1 - c')^2 + (1+S')(1/\Lambda + 1 - c')^2 - 2\xi'^2\,. \tag{6.23}$$

The dispersion relation in this form is similar to the form of dispersion relation for unconfined single vortex sheet given by Eq. 4.41. The only difference is in the last term, where the term ξ for single shear layer is replaced by $2\xi^2$ in the double shear layer case.

The saddle points can be obtained analytically by following the same steps as performed for the unconfined single vortex sheet in § 4.1.3.1. First, we redefine the mass flux and momentum flux, defined by Eq. 4.39 and Eq. 4.40 respectively, in terms of the new non-dimensional density parameter as

$$\mathcal{M} = \frac{1}{\Lambda} + S'\,, \text{ and} \tag{6.24}$$

$$\mathcal{J} = \frac{1}{\Lambda^2} + \frac{2S'}{\Lambda} + 1\,. \tag{6.25}$$

Using the above definition and the dispersion relation given by Eq. 6.23, the location of the saddle point is given as

$$c' = \frac{1}{4}\mathcal{M}'\left(1 \pm \left(1 - \frac{2}{3}\mathcal{Q}'\right)^{1/2}\right)\,, \text{ and} \tag{6.26}$$

$$k' = \pm\frac{\mathcal{M}'}{2\sqrt{2}}\left(\pm\left(1-\frac{2}{3}\mathcal{Q}'\right)^{1/2} - (1-\mathcal{Q}')\right)^{1/2}\,, \tag{6.27}$$

where, $\mathcal{Q}' = 4\mathcal{J}'/(3\mathcal{M}'^2)$. From Eq. 6.26 and noting that $\mathcal{J}' = \mathcal{M}'^2 - S'^2 + 1$, we obtain the equation for the CAIB in the $(1/\Lambda, S, h)$-space as $\mathcal{Q}' = 3/2$, or

$$\frac{1}{8}\mathcal{M}'^2 + \mathcal{S}'^2 = 1\,. \tag{6.28}$$

The minimum shear at which the absolute instability occurs can be obtained by calculating the value of S' for which $1/\Lambda$ is maximum. The value of $1/\Lambda$ is obtained from Eq. 6.28 as

$$\frac{1}{\Lambda} = \pm 2\sqrt{2(1 - S'^2)} - S'\,. \tag{6.29}$$

The maximum value of $1/\Lambda$ is obtained by solving $\mathrm{d}(1/\Lambda)/\,\mathrm{d}S' = 0$ for S', which gives $S' = \pm 1/3$. The corresponding value of shear is $\Lambda = \mp 1/3$, '$+$' for wakes ($U_2 > U_1$) and '$-$' for jets ($U_1 > U_2$). Using Eq. 6.22, the analytical relation between the parameters S and h that requires least shear to achieve absolute instability is given as

$$h = \frac{3S - 1}{S - 3}\,, \text{ for jets, and} \tag{6.30}$$

$$h = \frac{3S + 1}{S + 3}\,, \text{ for wakes.} \tag{6.31}$$

Fig. 6.4 shows the CAIB for the varicose perturbations of confined jet/wake shear flow as a function of shear (Λ), density parameter (S), confinement parameter (h), and surface tension parameter (Σ). The analytical expression for the absolutely unstable region in the strong surface tension limit is calculated from Eq. 6.28 as

$$\frac{1}{\Lambda} = \frac{\pm\sqrt{8(h^2 - 1)(S^2 - 1) + S - h}}{Sh - 1}\,, \tag{6.32}$$

and is shown as a shaded area along with the instability transition boundaries at discrete values of $\Sigma = 0.1, 1, 10, 1000$. The numerical calculation for $\Sigma = 1000$, which represents $\Sigma \gg 1$, is in excellent agreement with the analytical expression. For $S = 0$ in Fig. 6.4(a), the boundary is elliptical in the $(1/\Lambda, h)$-plane. This is similar to the boundary for the unconfined case, which is also elliptical in the $(1/\Lambda, S)$-plane, as shown in Fig. 6.3(a). Also, for values of S and h equal to ± 1, the inner flow, corresponding to $S = h = +1$, or the outer flow, corresponding to $S = h = -1$, fluctuations vanish and the flow becomes stable.

For the sinuous perturbations in the strong surface tension limit $\Sigma \to \infty$, the dispersion relation Eq. 4.71 can be transformed into an algebraic relation by using the first-order approximations of the hyperbolic terms given in Eq. 4.76 and Eq. 4.77.

$$\mathcal{D} = \frac{2\xi(1 - S)(1/\Lambda - 1 - c)^2}{\Sigma(1 + h)} + \frac{\Sigma(1 - h)(1 + S)(1/\Lambda + 1 - c)^2}{2\xi} - \xi\,. \tag{6.33}$$

As with the general dispersion relation Eq. 4.71, the simplified dispersion relation for sinuous case given by Eq. 6.33 remains asymmetric. Unlike the varicose case, the analytic solutions for the sinuous case does not provide any additional information about the convective/absolute transition. Alternatively, the physical interpretation of the terms in the dispersion relation can be derived. The pressure fluctuation in the inner flow, given by the first term, is an $\mathcal{O}(\Sigma^2)$ smaller than the

pressure fluctuations in the outer flow, given by the second term. Therefore, the magnitude is not large enough to overcome the pressure jump across the interface due to surface tension, given by the last term, and the perturbations at the interface cannot be sustained. The pressures in the inner and outer flows can be balanced only around the value $(1+h) \sim \mathcal{O}(\Sigma^{-2})$. This can be observed from Fig. 6.5 where the region of absolute instability for the high value of Σ ($\Sigma = 1000$), such that $\Sigma^{-2} \to 0$, is virtually absent as it is confined to a very small area near the $h = -1$ line.

6.3.2.2 General values of surface tension

The influence of confinement parameter h can be observed for a general parameter set (Λ, S, Σ). For varicose perturbations, it can be observed from Fig. 3.4 that the flow is symmetric in the transformation $(U_1, U_2, \rho_1, \rho_2, h_1, h_2, \sigma) \leftrightarrow (U_2, U_1, \rho_2, \rho_1, h_2, h_1, \sigma)$. This transformation is represented in terms of the non-dimensional parameters as $(\Lambda, S, h, \Sigma) \leftrightarrow (-\Lambda, -S, -h, \Sigma)$. In the limit of strong confinement ($h \to -1$) it can be inferred from Fig. 3.4 that the sinuous perturbations also obey the same transformation $(\Lambda, S, h, \Sigma) \leftrightarrow (-\Lambda, -S, -h, \Sigma)$ as the varicose perturbations. This may also be understood by observing that the distinguishing hyperbolic terms in the dispersion relations Eq. 4.70 and Eq. 4.71 assume equivalent values $\coth(2\xi/((1+h)\Sigma)) \to 1$ and $\tanh(2\xi/((1+h)\Sigma)) \to 1$ in the limit $h \to -1$. From Eq. 4.91, the strong confinement limit for which the sinuous-varicose symmetry is valid, is given as

$$|h| \ll \frac{16(1/\Lambda + S)^2}{9\Sigma} - 1\,. \tag{6.34}$$

The symmetry is therefore valid in a band around $h = -1$ with the size of the band decreasing with the increasing value of Σ. This allows the calculation of transition boundary in the strong confinement limit for sinuous and varicose perturbations from the unconfined ($h = 1$) varicose results. This can be clearly observed from Fig. 6.4 and Fig. 6.5 where the convective/absolute instability boundary for the sinuous and varicose cases at strong confinement ($h = -1$) can be obtained from the varicose case at weak confinement ($h = 1$) under the transformation $(\Lambda, S) \leftrightarrow (-\Lambda, -S)$.

For general values of surface tension parameter Σ, it can be seen that the regions of absolute instability expands with decreasing value of S or reduces with increasing value of Σ. For $S = 0$, the confined varicose case conforms to the symmetric transformation $(\Lambda, h) \leftrightarrow (-\Lambda, -h)$. The absolutely unstable regions are also widest for $h > 0$ for the values of $S > 0$, which becomes more prominent as S or Σ increases. For $S < 0$ (not plotted), the CAIB is mirror about the $h = 0$ line.

For sinuous perturbations, the region of absolute instability reduces with increasing S and vanishes for values of $\Sigma \gg 1$. The symmetric transformation, similar to the varicose perturbations, is not obeyed by the sinuous perturbations. The plots, along with the dispersion relation Eq. 4.71, also highlight the fact that for weak confinement ($0 < h < 1$), the pressure fluctuations are subdued by the surface tension, which reduces the absolute stability region. On the other had, for strong confinement ($-1 < h < 0$), the absolute instability region exists even for the strong values of co-flow ($|1/\Lambda| > 1$).

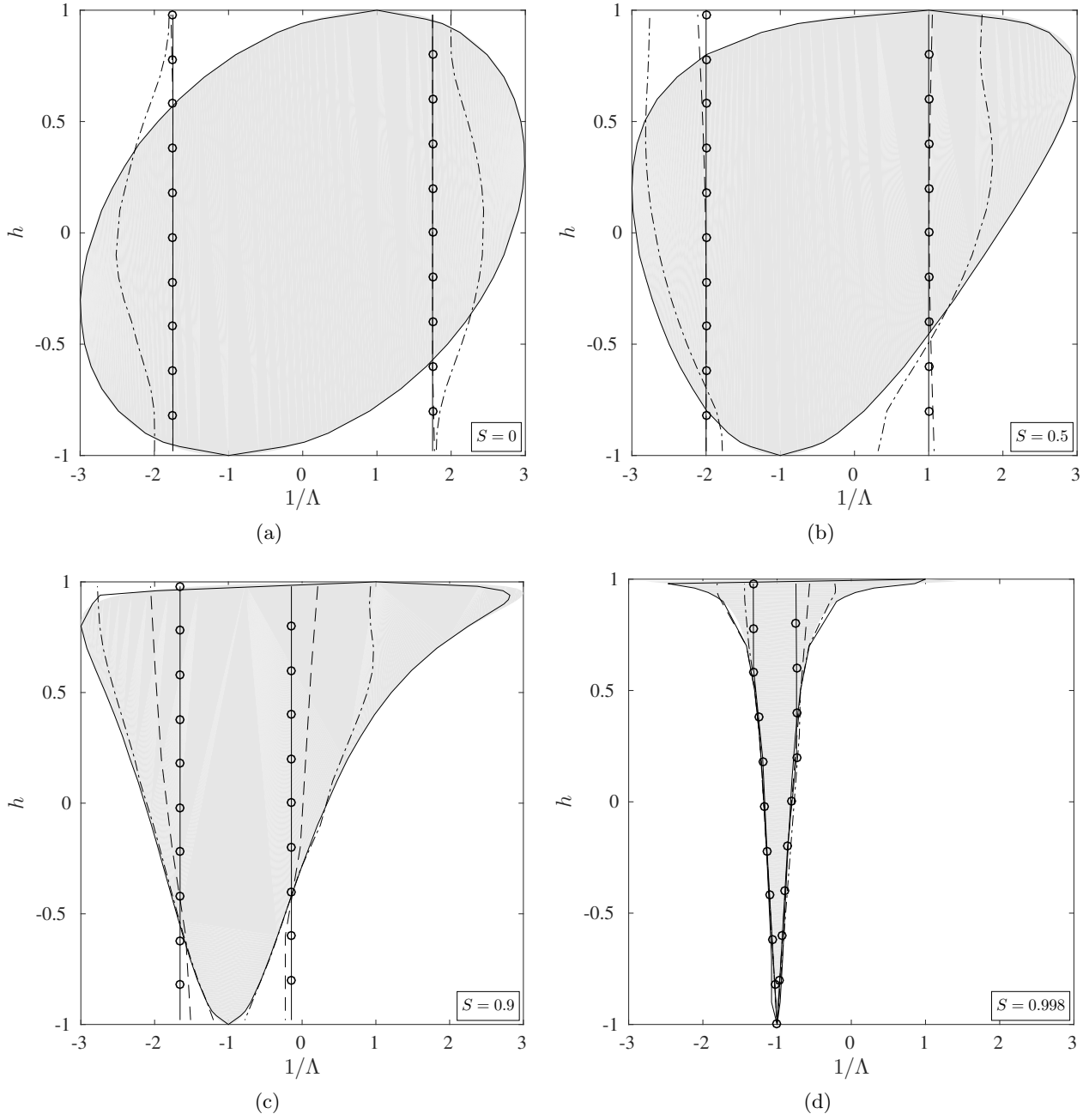

Figure 6.4: Convective/absolute instability transition boundaries for varicose perturbations of a confined jet/wake shear flow as a function of (Λ, S, h, Σ). At each discrete value of S, the CAIB is plotted in the $(1/\Lambda, h)$ for $\Sigma = 1000$ (solid), $\Sigma = 10$ (dot-dashed), $\Sigma = 1$ (dashed), $\Sigma = 0.1$ (circle). The shaded region is obtained from the analytic relation for the CAIB for strong surface tension limit, $\Sigma \gg 1$.

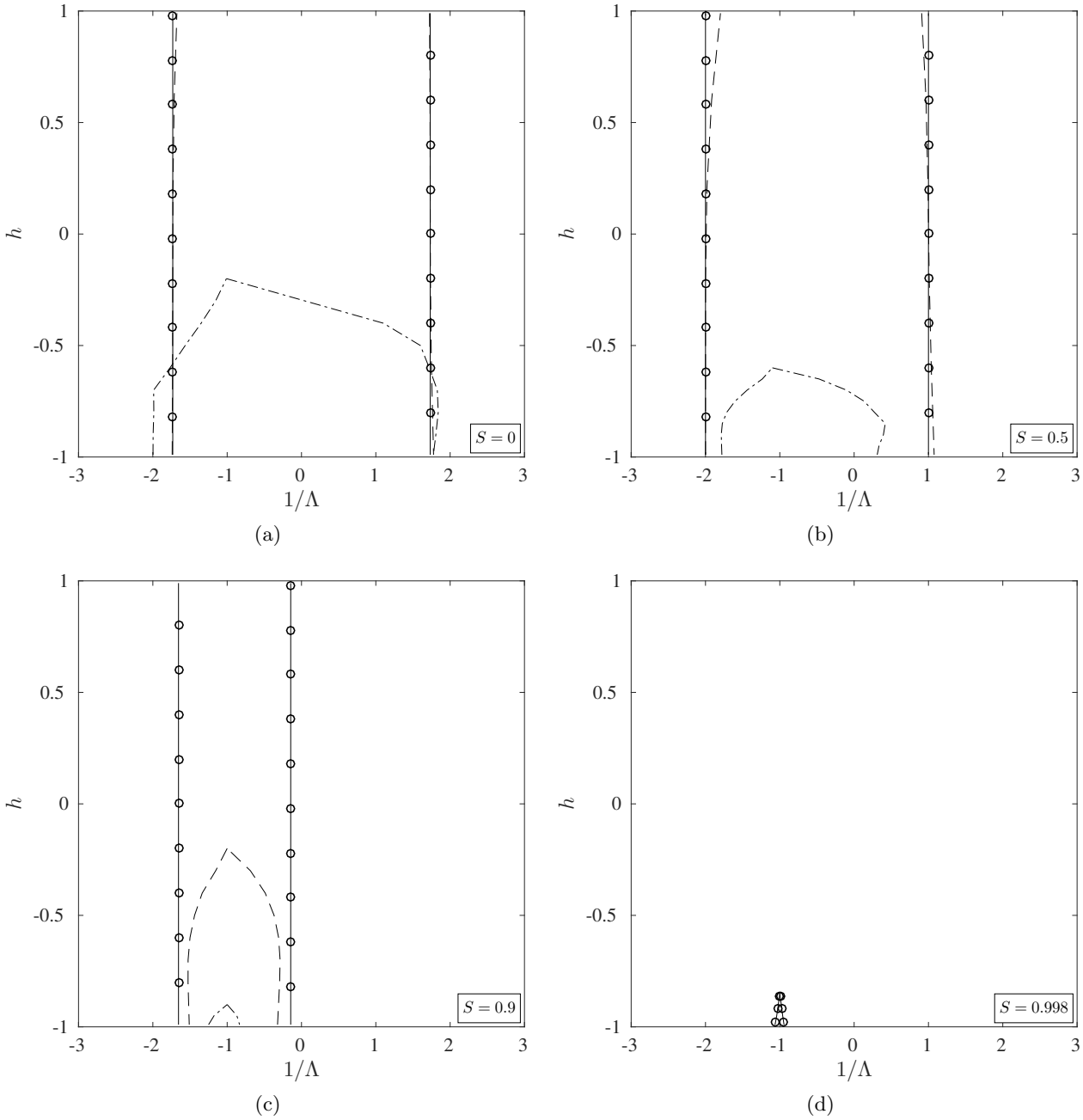

Figure 6.5: Convective/absolute instability transition boundaries for sinuous perturbations of a confined jet/wake shear flow as a function of (Λ, S, h, Σ). At each discrete value of S, the CAIB is plotted in the $(1/\Lambda, h)$ for $\Sigma = 10$ (dot-dashed), $\Sigma = 1$ (dashed), $\Sigma = 0.1$ (circle).

6.3.3 Conclusion

The effect of surface tension and confinement on the stability of jet/wake flows is studied as an extension of the study performed in § 4.2. For the unconfined jets and wakes, the surface tension mode does not interact significantly with the primary jet/wake column mode when $\Sigma < 8\mathcal{M}^2/9$, where $\mathcal{M}$ is the mass flux. At low values of Σ, the surface tension mode is always more unstable than the jet/wake column mode. When $\Sigma > 8\mathcal{M}^2/9$, the surface tension mode and jet/wake column modes start to interact. Increasing the surface tension causes the varicose perturbations to be more unstable at $S < 0$ (dense inner fluid) and more stable at $S > 0$ (light inner fluid). The sinuous perturbations behave in reverse manner. At moderate values of Σ, therefore, jet/wake flows with surface tension are more unstable than equivalent single shear layers with surface tension and much more unstable than equivalent jets/wakes without surface tension. Anyway, increasing Σ stabilises all the perturbations.

For confined jets and wakes in strong surface tension limit, the behaviour of varicose perturbations is symmetric under the transformation $(S, h) \leftrightarrow (h, S)$. In other words, the change in confinement acts as change in density ratio between the fluids. Therefore, for uniform density ratio, the absolutely unstable region is an ellipse in the $(1/\Lambda, h)$-space. which extends to $1/\Lambda = \pm 3$. For other density ratios, the flow is absolutely unstable when $8\mathcal{J}' > 9\mathcal{M}'^2$. At high value of Σ, the varicose mode is highly absolutely unstable for strongly confined dense jet/wake flows ($h > 0, S < 0$). Also, the varicose perturbations are more unstable than the sinuous perturbations.

It can be concluded from this analysis that surface tension and confinement considerably influences the stability of planar jet/wake flows. It must be noted that the results have been derived for plug flow velocity profiles and inviscid fluids. The results will be not accurate $Re < 10^2$ but accurate for $Re > 10^3$. Also, the results will not be applicable when the actual shear layer thickness exceeds the wavelength of the surface tension mode that is predicted by this model, $\lambda \sim \pi\sigma/(\rho_{\text{ref}} U_{\text{ref}}^2)$.

□

Chapter 7

Conclusion and future work

This thesis aims at studying the instability of the shear flows by using the low order models. Simple analytical flows are considered first which offer an insight into the important features that affect the stability of jet and wake flows. These results are useful in validating the instability analysis results of the smooth approximations of experimental base flows.

7.1 Conclusion

The analytical shear layer models represent simple features, *e.g.* shear strength and confinement, that give rise to instability. The importance of studying these models lies in the fact that the simple features contribute to the instability of the realistic flows. It is observed that the shear layer models in general cannot give rise to absolute instability without the presence of a dispersive medium, *e.g.* when the surface tension has a finite non-zero value. When the temporal stability is considered, both the surface tension and finite thickness of the shear layer act as stabilising mechanisms for the flow at short wavelengths, the cut-off wavelength being governed by the magnitude of the surface tension and/or the shear width. The CAIB of the single shear layer with surface tension is an ellipse in the $(1/\Lambda, S)$-space. The absolutely unstable region extends to a significant region of co-flow, $|\Lambda| < 1$.

The jet and wake flows are studied and it is observed that the effect of surface tension and confinement for varying velocity and density ratios is significant in deciding the spatio-temporal behaviour. Two distinct modes – the *surface tension* modes, where the shear layers behave independently, and the *jet/wake column* modes, where the shear layers interact in sinuous or varicose manner – govern the response of the flow. The surface tension mode dominates the asymptotic response.

For unconfined jets and wakes with varicose perturbations, the flow is more unstable when the inner fluid is more dense than the outer fluid ($S < 0$) and more stable when the inner fluid is less dense than the outer fluid ($S > 0$). The sinuous perturbations behave in reverse manner. It is observed that, jet/wake flows with moderate value of surface tension are more unstable than

the equivalent single shear layers with surface tension and much more unstable than the jet/wake flows without surface tension. Very high value of surface tension stabilises all the perturbations.

For the confined flows in strong surface tension limit, it is observed that the change in confinement is similar to the change in the density ratio of the flows. For jet/wake flows with non-uniform densities, absolute instability is obtained when $8\mathcal{J}' > 9\mathcal{M}'^2$. For high values of surface tension, the varicose mode is found to be highly absolutely unstable for strongly confined dense jet/wake flows ($h > 0, S < 0$).

The semi-unconfined planar shear layer is studied analytically and successfully implemented numerically for smooth profile approximations to the experimental base flows. Due to absence of a dispersive medium in the form of viscosity and surface tension, the flow does give rise to absolute instability. However, the temporal branches obtained numerically for the smooth profiles show excellent agreement with the literature, which indicates that the linear profile approximations offer great insight into the instability mechanism without sacrificing simplicity and that the spatio-temporal analysis can be extended to realistic flow profiles.

7.2 Future work

The future extension of this work mostly includes the application of the numerical tools developed for the low order models to the high order models such as the experimental base flows can be considered in a more general manner. The following extensions will improve the applicability of the numerical tools to more general cases:

1. Though the inviscid solution to the Rayleigh's equation was sufficient for the scope of current thesis, for several applications the viscous Orr-Sommerfeld equation can be considered. Viscosity will influence the diffusion of the perturbations and may change the spatio-temporal behaviour of the flows where viscosity cannot be neglected. Rees [26] observed that the viscosity can be exclusively destabilising.

2. As many flow geometries are axisymmetric, especially jet/wake flows, it will be beneficial to adopt cylindrical coordinate system. The planar flows studied in thesis can be considered as validation cases for the round flows where the curvature effects are negligible and the shear and confinement continue to destabilise the flow.

3. It has been shown that the density ratio influences the instability behaviour of the flows. Therefore, the influence of temperature in a realistic reacting flow on the density profile must be considered. The spatio-temporal stability behaviour needs to be recalculated for the cases considered in this thesis to study the influence of temperature variations.

4. The LST tool used in this thesis requires the flow to be locally parallel. The variation of the streamwise component of the wavenumber is therefore neglected. To study more realistic non-parallel flows, more sophisticated stability theories like the Parabolised Stability Equations or the BiGlobal Theory can be applied with the numerical tools developed here for the spatio-temporal analysis.

□

Appendix A

Proof of Briggs-Bers criteria

The general formulation for the response of a spatially infinite system to a sinusoidal source introduced at $t = 0$ is given as

$$\mathcal{G}(x,t) = \int_{-\infty+\mathrm{i}\sigma}^{+\infty+\mathrm{i}\sigma} \frac{\mathrm{d}\omega}{2\pi} \mathrm{e}^{-\mathrm{i}\omega t} I(x,\omega) \tag{A.1}$$

where

$$I(x,\omega) = \int_{-\infty}^{\infty} \frac{\mathrm{d}k}{2\pi} \frac{\mathrm{e}^{\mathrm{i}kx}}{\mathcal{D}(k,\omega)} \tag{A.2}$$

The unstable, time-asymptotic behaviour of $\mathcal{G}(x,t)$ is determined by the singularities in the ω-plane between the L-contour and the real ω-axis. These singularities prevent the extension of the region of absolute convergence into the lower-half ω-plane (as shown in Fig. A.1). The causality condition requires that the integral $I(x,\omega)$ should be analytic for $\omega_\mathrm{i} > \sigma$ for the response $\mathcal{G}(x,t)$ to be zero for $t < 0$. Therefore, the analytic continuation of $I(x,\omega)$ below the original L-contour leads to a situation where the branches of $\omega(k_\mathrm{i})$ are encountered. As these branches cannot be crossed without violating causality, lines of discontinuity form in the function $I(x,\omega)$.

The lines of discontinuity can be deformed as long as the F-contour remains within the strip of convergence (as shown in Fig. A.1(a)). The singularities of $I(x,\omega)$ appear at the values for which F-contour cannot be deformed, and thus, restricting the further lowering of L-contour. This condition can be verified for simple cases where it is assumed that $\mathcal{D}^{-1}$ is single valued with isolated singularities only, and $\lim_{k\to\infty} \mathcal{D}^{-1} \to 0$ at least as fast as $|k|$. Therefore, for ω within the domain of absolute convergence, these assumptions allow the integral in Eq. A.2 to be calculated by closure of the contour at $|k| \to \infty$ in the upper half of k-plane for $x > 0$ (as shown in Fig. A.2) and in the lower half of k-plane for $x < 0$.

Here, for the simple case, the integrand in Eq. A.2 has poles in the complex k-plane for fixed value of ω on the L-contour at the *normal modes*, *i.e.*, at the roots of $\mathcal{D}(k,\omega) = 0$. However, for practical cases, in place of isolated poles, branch lines are obtained in the k-plane for fixed value of ω. This is interpreted as a continuum of normal modes. The current assumptions can be extended to these

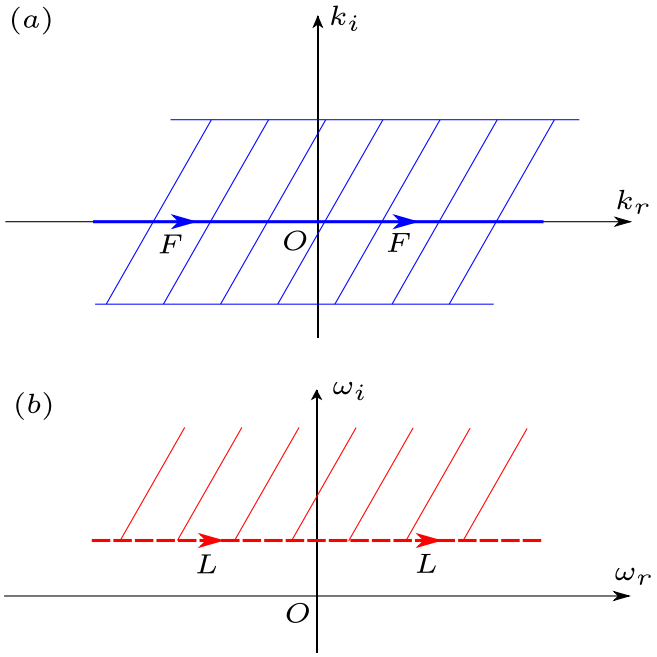

Figure A.1: Domains of absolute convergence for the Green's function $\mathcal{G}$. In the (a) complex k-plane, for a spatially finite, bidirectional (*i.e.*, for $x < 0$ and $x > 0$) response, the domain is a strip including the real k-axis. In the (b) complex ω-plane, to satisfy causality condition, the domain is considered as a half-plane.

cases. Returning to our current problem, the integral $I^+(x,\omega) \equiv I(x > 0, \omega)$ from Eq. A.2 can be evaluated using residue theorem as the sum of normal modes

$$I^+(x,\omega) = +\cancel{2\pi}\mathrm{i} \sum_{\substack{\text{enclosed} \\ \text{poles } k^+}} \operatorname*{Res}_{k=k^+} \left\{ \frac{1}{\cancel{2\pi}} \cdot \frac{\mathrm{e}^{\mathrm{i}kx}}{\mathcal{D}(k,\omega)} \right\} . \tag{A.3}$$

Here, the integration is positive for the counter-clockwise orientation of the contour. The residual is evaluated at each normal mode as follows

$$\begin{aligned}
\operatorname*{Res}_{k=k^+} \left\{ \frac{\mathrm{e}^{\mathrm{i}kx}}{\mathcal{D}(k,\omega)} \right\} &= \lim_{k\to k^+} (k-k^+) \frac{\mathrm{e}^{\mathrm{i}kx}}{\mathcal{D}(k,\omega)} \\
&= \lim_{k\to k^+} (k-k^+) \frac{\mathrm{e}^{\mathrm{i}kx}}{\cancel{\mathcal{D}|_{k^+}}^{\,0} + \frac{\partial \mathcal{D}}{\partial k}\big|_{k^+} (k-k^+) + \frac{1}{2} \frac{\partial^2 \mathcal{D}}{\partial k^2}\Big|_{k^+} (k-k^+)^2 + \mathcal{O}(k^3)} \\
&= \lim_{k\to k^+} \frac{\mathrm{e}^{\mathrm{i}kx}}{\frac{\partial \mathcal{D}}{\partial k}\big|_{k^+} + \frac{1}{2} \frac{\partial^2 \mathcal{D}}{\partial k^2}\Big|_{k^+} (k-k^+) + \mathcal{O}(k^2)} \\
&= \frac{\mathrm{e}^{\mathrm{i}k^+x}}{\frac{\partial \mathcal{D}}{\partial k}\big|_{k^+}} .
\end{aligned} \tag{A.4}$$

Thus, from Eq. A.3, we get

$$I^+(x,\omega) = \mathrm{i}H(x) \sum_{k^+} \frac{\mathrm{e}^{\mathrm{i}k^+(\omega)x}}{\frac{\partial \mathcal{D}}{\partial k}\big|_{k^+}} . \tag{A.5}$$

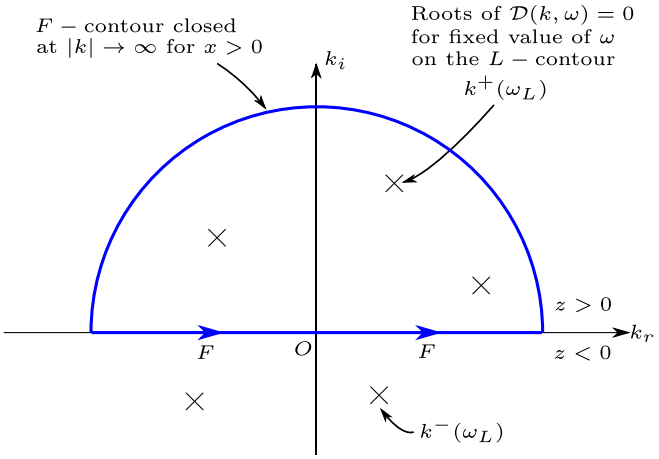

Figure A.2: Integration contour for $I(x,\omega)$ for $z > 0$ with isolated poles ($\times$) given by the roots of dispersion relation $\mathcal{D}(k,\omega) = 0$.

Similarly, for the lower half of k-plane, the integral is given as

$$I^-(x,\omega) = -\mathrm{i}H(-x)\sum_{k^-}\frac{\mathrm{e}^{\mathrm{i}k^-(\omega)x}}{\frac{\partial\mathcal{D}}{\partial k}\big|_{k^-}}\,. \tag{A.6}$$

Here, H is the Heaviside step function in x. The integrand in Eq. A.2 is finally given as the sum of I^+ and I^- from Eqs. A.5 and A.6

$$I(x,\omega) = \mathrm{i}H(x)\sum_{k^+}\frac{\mathrm{e}^{\mathrm{i}k^+(\omega)x}}{\frac{\partial\mathcal{D}}{\partial k}\big|_{k^+}} - \mathrm{i}H(-x)\sum_{k^-}\frac{\mathrm{e}^{\mathrm{i}k^-(\omega)x}}{\frac{\partial\mathcal{D}}{\partial k}\big|_{k^-}}\,. \tag{A.7}$$

In Eq. A.7, the residues are calculated at the first-order poles in the k-plane for fixed value of ω taken within the region of absolute convergence, as shown in Fig. A.1. This means that for $\omega = \omega_L$, the corresponding branches in k-plane ($k(\omega_L)$) are divided in two sets: the branches lying in upper k-plane, $k_\mathrm{i}(\omega_L) > 0$, designated as k^+, and the branches lying in lower k-plane, $k_\mathrm{i}(\omega_L) < 0$, designated as k^- (see Eq. A.7). Also note that both terms on the right side of Eq. A.7 are spatially decaying.

The detailed response of a system can be calculated from the Laplace contour integration as given in Eq. A.1. For defining asymptotic response, the Laplace contour in Fig. A.1(b) needs to be deformed to the lower ω-plane. From Eq. A.1 and the causality condition, it is evident that the asymptotic response will be governed by the highest singularity of $I(x,\omega)$ in the ω-plane.

The analyticity of $I(x,\omega)$ is explored by traversing the complex ω-plane. From Fig. A.2, it is evident that the $I(x,\omega)$ is a well-behaved function as long as the poles (given by the roots of $\mathcal{D}(k,\omega)$) do not cross the real k-axis. As the frequency $\omega' = \omega'_\mathrm{i} + \mathrm{i}\sigma'$ is crossed by the Laplace contour, the value of $I(x,\omega)$ jumps by an amount equal to the residue at the pole that crossed the real k-axis.

We note here that in order to allow the pole of $\mathcal{D}^{-1}(k,\omega)$ to cross the real k-axis, the dispersion relation must provide complex ω solutions with $\omega_\mathrm{i} > 0$ for some real values of k. This means that the infinite, homogeneous system must support unstable modes. Therefore, the value of σ in

integral Eq. A.1 must be selected larger than the maximum temporal growth rate of any unstable wave, as stated before.

The integral $I(x,\omega)$ can be analytically continued across the branch point by deforming the integration contour to $\widetilde{F}$ as shown in Fig. A.3. The contour deformation ensures that the poles which have $k_\mathrm{i} > 0$ ($k_\mathrm{i} < 0$) when $\omega_\mathrm{i} > \sigma'$ enter the sum as modes k^+ (k^-) in the Eq. A.7. The number of poles for $x > 0$ and $x < 0$ remain same and there is no discontinuity in the value of $I(x,\omega)$ when the Laplace contour crosses ω'. It is easily observed that the pole B (and A) represents an amplifying wave for $x > 0$ ($x < 0$) as it crossed the real k-axis, thus making the term e^{k^+x} (e^{k^-x}) in Eq. A.7 growing.

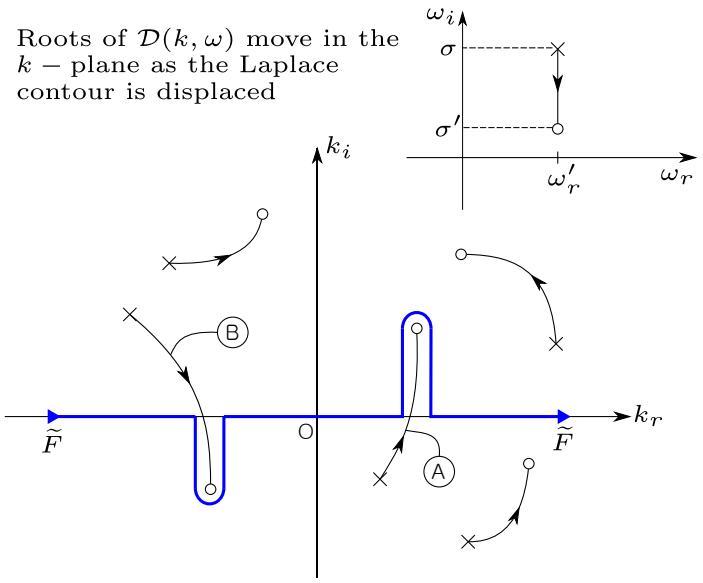

Figure A.3: Deformation of Fourier contour $\widetilde{F}$ around the poles crossing the real k-axis. (Briggs [3])

However, the contour deformation gets inhibited at some $\omega = \omega_s$ when the $\widetilde{F}$-contour becomes *pinched* by two merging poles at a corresponding complex $k = k_s$ as shown in Fig. A.4. As $(\omega - \omega_s) \to 0$, the function $I(x,\omega) \to \infty$. The double root at k_s is a *saddle point* of $\omega(k)$ and ω_s is the *branch point* of $k(\omega)$. In this situation, $I(x,\omega)$ exhibits a singularity due to the double root in k at k_s implying $\mathcal{D} = 0$ and $(\partial\mathcal{D}/\partial k) = 0$. The singularity criterion as stated by Bers [2] is

> Among all double (or multiple) roots in k that occur for ω below ω_L, and are given by the simultaneous solutions of $\mathcal{D} = 0$ and $(\partial\mathcal{D}/\partial k) = 0$, only the ones that coalesce by pinching the deformed F-contour give rise to a singularity in $I(x,\omega)$ at the ω corresponding to the pinch. [2]

The statement can be validated analytically from the behaviour of $I(x,\omega)$ in the neighbourhood of the double pole (k_s,ω_s). The double pole satisfies

$$\left.\frac{\partial\mathcal{D}}{\partial k}\right|_{(k_s,\omega_s)} = 0 \quad \text{and} \quad \mathcal{D}(k_s,\omega_s) = 0\,. \tag{A.8}$$

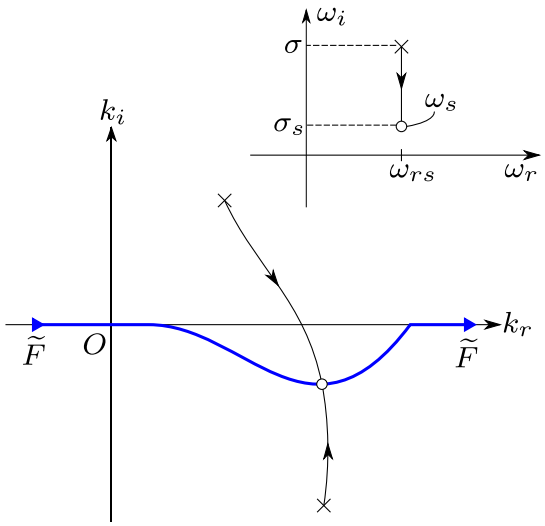

Figure A.4: Merging of poles through contour $\widetilde{F}$. (Briggs [3])

The Taylor expansion of the dispersion relation near the singularity (k_s, ω_s) is

$$\mathcal{D}(k,\omega) = \cancelto{0}{\mathcal{D}\big|_s} + (k-k_s)\cancelto{0}{\frac{\partial \mathcal{D}}{\partial k}\bigg|_s} + (\omega-\omega_s)\,\frac{\partial \mathcal{D}}{\partial \omega}\bigg|_s + \frac{(k-k_s)^2}{2!}\,\frac{\partial^2 \mathcal{D}}{\partial k^2}\bigg|_s + \mathcal{O}(k^3,\omega^2) = 0\,. \quad \text{(A.9)}$$

The lowest order approximation gives

$$\begin{aligned} \mathcal{D}(k,\omega) &= (\omega-\omega_s)\,\frac{\partial \mathcal{D}}{\partial \omega}\bigg|_s + \frac{(k-k_s)^2}{2}\frac{\partial^2 \mathcal{D}}{\partial k^2}\bigg|_s = 0 \\ \Rightarrow \quad (k-k_s) &= \pm \mathrm{i}\left[2\left(\frac{\partial \mathcal{D}}{\partial \omega}\right)\left(\frac{\partial^2 \mathcal{D}}{\partial k^2}\right)^{-1}\right]_s^{1/2} (\omega-\omega_s)^{1/2}\,. \end{aligned} \quad \text{(A.10)}$$

The positive value (+ sign) in Eq. A.10 corresponds to the region above the F-contour as we have $k^+ > k_s$. Similarly, the negative value (- sign) corresponds to the region below the F-contour where $k^- < k_s$.

As our primary interest is in the behaviour of $I(x,\omega)$ near the double pole, we need to use Eq. A.10 to calculate the derivative $\partial\mathcal{D}/\partial k$ and substitute in Eq. A.4. We begin with taking the k-derivative of Eq. A.9.

$$\frac{\partial \mathcal{D}}{\partial k}(k.\omega) = \frac{\partial \mathcal{D}}{\partial \omega}\bigg|_s \frac{\mathrm{d}\omega}{\mathrm{d}k} + \frac{\partial^2 \mathcal{D}}{\partial \omega^2}\bigg|_s (\omega-\omega_s)\frac{\mathrm{d}\omega}{\mathrm{d}k} + \frac{\partial^2 \mathcal{D}}{\partial k^2}\bigg|_s (k-k_s) + \mathcal{O}(k^2,\omega^2)\,. \quad \text{(A.11)}$$

In the limit $k \to k_s$ and $\omega \to \omega_s$, the Eq. A.11 reduces to

$$\frac{\partial \mathcal{D}}{\partial k}(k_s.\omega_s) = \frac{\partial \mathcal{D}}{\partial \omega}\bigg|_s \frac{\mathrm{d}\omega}{\mathrm{d}k} + 0\,. \quad \text{(A.12)}$$

For the double pole, we have $(\partial\mathcal{D}/\partial k)_S = 0$ and generally $(\partial\mathcal{D}/\partial\omega)_S \neq 0$. Thus, for Eq. A.12 to be satisfied, we require

$$\frac{\mathrm{d}\omega}{\mathrm{d}k} = 0 \quad \text{at} \quad k = k_s \quad \text{(A.13)}$$

This result will be used to calculate the derivative $\partial\mathcal{D}/\partial k$. Taking the k-derivative of the first expression in Eq. A.10

$$\left.\frac{\partial\mathcal{D}}{\partial k}\right|_s = \left.\frac{\partial\mathcal{D}}{\partial\omega}\right|_s \cancelto{0}{\left.\frac{\mathrm{d}\omega}{\mathrm{d}k}\right|_s} + \left.\frac{\partial^2\mathcal{D}}{\partial k^2}\right|_s (k-k_s) = \left.\frac{\partial^2\mathcal{D}}{\partial k^2}\right|_s (k-k_s)\,. \tag{A.14}$$

Substituting the value of $(k-k_s)$ from Eq. A.10, we get

$$\begin{aligned}\left.\frac{\partial\mathcal{D}}{\partial k}\right|_s &= \left.\frac{\partial^2\mathcal{D}}{\partial k^2}\right|_s \left(\pm\mathrm{i}\left[2\left(\frac{\partial\mathcal{D}}{\partial\omega}\right)\left(\frac{\partial^2\mathcal{D}}{\partial k^2}\right)^{-1}\right]_s^{1/2}(\omega-\omega_s)^{1/2}\right)\\ &= \pm C(\omega-\omega_s)^{1/2}, \quad \text{where} \quad C = \mathrm{i}\left[2\left(\frac{\partial\mathcal{D}}{\partial\omega}\right)\left(\frac{\partial^2\mathcal{D}}{\partial k^2}\right)\right]_s^{1/2}.\end{aligned} \tag{A.15}$$

The derivative $\partial\mathcal{D}/\partial k$ can now be substituted from Eq. A.15 into Eq. A.7.

$$I(x,\omega) = \frac{\mathrm{i}H(x)\mathrm{e}^{\mathrm{i}k^+(\omega)x}}{C(\omega-\omega_s)^{1/2}} - \frac{\mathrm{i}H(-x)\mathrm{e}^{\mathrm{i}k^-(\omega)x}}{-C(\omega-\omega_s)^{1/2}} + I_R(x,\omega)\,, \tag{A.16}$$

where I_R represents the contribution from the k^+ and k^- poles that are not in the vicinity of k_s. Using the property $H(-x) = 1 - H(x)$, Eq. A.16 can be re-written as

$$I(x,\omega) = \frac{\mathrm{i}\mathrm{e}^{\mathrm{i}k^-(\omega)x}}{C(\omega-\omega_s)^{1/2}} + \mathrm{i}H(x)\left[\frac{\mathrm{e}^{\mathrm{i}k^+(\omega)x} - \mathrm{e}^{\mathrm{i}k^-(\omega)x}}{C(\omega-\omega_s)^{1/2}}\right] + I_R(x,\omega)\,. \tag{A.17}$$

For the limit $\omega \to \omega_s$, $k^+ \to k_s$ and $k^- \to k_s$, and using Eq. A.10 and Eq. A.10

$$I(x,\omega) = \frac{\mathrm{i}\mathrm{e}^{\mathrm{i}k_s(\omega)x}}{C(\omega-\omega_s)^{1/2}} + \mathrm{i}H(x)\left[\left(\frac{\partial^2\mathcal{D}}{\partial k^2}\right)^{-1}\frac{\partial(\mathrm{e}^{\mathrm{i}k(\omega)x})}{\partial k}\right]_s + I_R(x,\omega_s)\,. \tag{A.18}$$

It is clearly observed that the first term applies to the complete k-plane and has a branch-pole singularity at $\omega = \omega_s$. The second and third terms, on the contrary, are regular in ω. An important conclusion can be now drawn from the singularity term in Eq. A.18 regarding the double pole. If the double pole is formed by the merging of either two k^+ roots or two k^- roots, the first two terms in Eq. A.16 would both contain either $H(x)$ or $H(-x)$ and the singularity term would not exist. Thus, as stated by Bers [2], the ω_s solutions of Eq. A.8 will be the singular points of $I(x,\omega)$ only if the corresponding k_s is obtained by the pinching of the deformed F-contour.

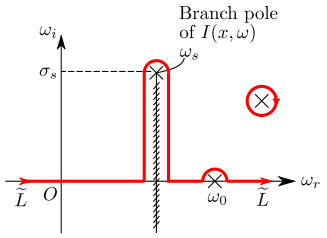

Figure A.5: Laplace contour for evaluating asymptotic response $\widetilde{F}$. (Briggs [3])

The contour deformation in both k and ω complex planes is performed and all the *pinch* points are identified by continuous lowering of the L-contour. The time-asymptotic response is dominated by the contribution of the pinch-point singularity which has $\omega_i = \max(\omega_{s,i})$ as shown in Fig. A.5. The singularity term in Eq. A.18 dominates near this pinch point and the asymptotic response is obtained by substituting $I(x,\omega)$ into Eq. A.1

$$\begin{aligned}\lim_{t\to\infty} \mathcal{G}(x,t) &\sim \oint_{\omega_s} \frac{\mathrm{d}\omega}{2\pi} \mathrm{e}^{-\mathrm{i}\omega t} I(x,\omega) \\ &= \frac{\mathrm{e}^{\mathrm{i}(k_s x - \omega_s t)}}{\left[2\left(\frac{\partial \mathcal{D}}{\partial \omega}\right)\left(\frac{\partial^2 \mathcal{D}}{\partial k^2}\right)\right]_s^{1/2}} \int \frac{\mathrm{e}^{-\mathrm{i}(\omega-\omega_s)t}}{(\omega-\omega_s)^{1/2}} \frac{\mathrm{d}\omega}{2\pi}\,.\end{aligned}$$

Performing the integration, we get, for the asymptotic response,

$$\lim_{t\to\infty} |\mathcal{G}(x,t)| \sim \frac{\mathrm{e}^{\mathrm{i}(k_s x - \omega_s t)}}{\left[2\pi\mathrm{i}\left(\frac{\partial \mathcal{D}}{\partial \omega}\right)\left(\frac{\partial^2 \mathcal{D}}{\partial k^2}\right)\right]_s^{1/2} t^{1/2}}\,, \tag{A.19}$$

where the contour has been deformed around the branch point and branch cut at ω_s. As k_s is, in general, complex, the asymptotic response can have a exponential envelope in space. The expression is not valid for large values of x (distance from the source) as we have kept x fixed as $t \to \infty$.

□

Appendix B

Rayleigh's equation and matching conditions

B.1 Rayleigh's equation

Proceeding with the base flow form of Eq. 2.2 and Eq. 2.3 and applying inviscid assumption, the Euler equation and the continuity equation is written in non-dimensional variables as

$$\rho\frac{\partial \mathbf{u}}{\partial t} + \rho\mathbf{u}\cdot\nabla\mathbf{u} = -\nabla p\,, \tag{B.1}$$

$$\nabla\cdot\mathbf{u} = 0\,. \tag{B.2}$$

Similar to Eq. 2.1, the flow quantities are decomposed as

$$\begin{aligned} u(x,y,z,t) &= U(y) + u'(x,y,z,t)\,,\\ v(x,y,z,t) &= v'(x,y,z,t)\,,\\ w(x,y,z,t) &= w'(x,y,z,t)\,,\\ p(x,y,z,t) &= P_0 + p'(x,y,z,t)\,. \end{aligned} \tag{B.3}$$

The Eq. B.3 is substituted in Eq. B.1 and Eq. B.2, and subsequently linearised to obtain

$$\rho\left(\frac{\partial}{\partial t} + U\frac{\partial}{\partial x}\right)\mathbf{u}' + \rho v'\frac{\mathrm{d}U}{\mathrm{d}y}\mathbf{i} = -\nabla p'\,, \tag{B.4}$$

$$\nabla\cdot\mathbf{u}' = 0\,. \tag{B.5}$$

The stability of the base flow is studied by introducing linear perturbations similar to the form given by Eq. 2.4. The decomposition of the perturbations into elementary stability waves is

therefore given as

$$\begin{aligned} u'(x,y,z,t) &= \widetilde{u}(y)\mathrm{e}^{\mathrm{i}(\alpha x+\beta z-\alpha ct)}\,, \\ v'(x,y,z,t) &= \widetilde{v}(y)\mathrm{e}^{\mathrm{i}(\alpha x+\beta z-\alpha ct)}\,, \\ w'(x,y,z,t) &= \widetilde{w}(y)\mathrm{e}^{\mathrm{i}(\alpha x+\beta z-\alpha ct)}\,, \\ p'(x,y,z,t) &= \widetilde{p}(y)\mathrm{e}^{\mathrm{i}(\alpha x+\beta z-\alpha ct)}\,, \end{aligned} \tag{B.6}$$

where $c = \omega/\alpha$ is the phase velocity. The components of Eq. B.5 can be expressed as

$$\begin{aligned} \mathrm{i}\alpha\rho(U-c)\widetilde{u} + \rho U'\widetilde{w} &= -\mathrm{i}\alpha\widetilde{p}\,, \\ \mathrm{i}\alpha\rho(U-c)\widetilde{v} &= -\widetilde{p}'\,, \\ \mathrm{i}\alpha\rho(U-c)\widetilde{w} &= -\mathrm{i}\beta\widetilde{p}\,, \\ \mathrm{i}(\alpha\widetilde{u}+\beta\widetilde{w}) + \widetilde{v}' &= 0\,, \end{aligned} \tag{B.7}$$

where the right-quote $'$ in Eq. B.7 above represents differentiation with respect to y (not to be mistaken with linear perturbation terms q' introduced in Eq. B.3). The boundary condition is

$$\widetilde{v} = 0 \quad \text{at} \quad y = y_1, y_2\,. \tag{B.8}$$

The governing equations derived above can be reduced to two-dimensional form by applying Squire's theorem [1]. This is achieved by applying transformations as given below

$$\widehat{k} \equiv \sqrt{\alpha^2+\beta^2}, \quad \widehat{k}\widehat{u} \equiv \alpha\widetilde{u} + \beta\widetilde{w}, \quad \frac{\widehat{p}}{\widehat{k}} \equiv \frac{\widetilde{p}}{\alpha} \text{ or } \frac{\widetilde{p}}{\beta}, \quad \widehat{v} \equiv \widetilde{v}, \quad \widehat{c} \equiv c\,. \tag{B.9}$$

The governing equation given by Eq. B.7 and the boundary condition given by Eq. B.8 can be now transformed to equivalent two-dimensional form

$$\begin{aligned} \mathrm{i}\widehat{k}\rho(U-c)\widehat{u} + \rho U'\widehat{v} &= -\mathrm{i}\widehat{k}\widehat{p}\,, \\ \mathrm{i}\widehat{k}\rho(U-c)\widehat{v} &= -\widehat{p}'\,, \\ \mathrm{i}\widehat{k}\widehat{u} + \widehat{v}' &= 0\,, \end{aligned} \tag{B.10}$$

where the x- and z-direction momentum equations in Eq. B.7 have been added. The boundary condition is also transformed as

$$\widehat{v} = 0 \quad \text{at} \quad y = y_1, y_2\,. \tag{B.11}$$

As the problem has been now transformed to two-dimensional form, the streamfunction can be introduced. The total streamfunction can be decomposed as

$$\psi(x,y,t) = \int^y U(y')\,\mathrm{d}y' + \psi'(x,y,t)\,, \tag{B.12}$$

where ψ' is the linear perturbation about the mean streamfunction. Therefore, by definition of the streamfunction, the perturbation velocities in two-dimensional incompressible flow regime are given as

$$u' = \frac{\partial\psi'}{\partial y} \quad \text{and} \quad v' = -\frac{\partial\psi'}{\partial x}\,. \tag{B.13}$$

[1] According to Squire (1993) three-dimensional disturbances in the classical, inviscid problem can be transformed into an equivalent two-dimensional problem, *i.e.*, to each unstable three-dimensional disturbance there corresponds a more unstable two-dimensional one (Drazin [5]).

The Fourier transform of the perturbation streamfunctions gives

$$\psi'(x,y,t) = \phi(y)\mathrm{e}^{\mathrm{i}\widehat{k}(x-\widehat{c}t)}\,, \tag{B.14}$$

where $\phi(y)$ is the perturbation streamfunction amplitude which characterises the distribution of the disturbance in the normal direction. From Eq. B.13, we get

$$\widehat{u} = \phi' \quad \text{and} \quad \widehat{v} = -\mathrm{i}\widehat{k}\phi\,. \tag{B.15}$$

The final step in deriving the inviscid governing equation is the elimination of the pressure term $\widehat{p}$ from Eq. B.10. The x-direction momentum equation is used to get an expression for $\widehat{p}$

$$\begin{aligned}\widehat{p} &= -\rho(U-c)\widehat{u} + \rho U'\frac{\widehat{v}}{-\mathrm{i}\widehat{k}} \\ &= -\rho(U-c)\phi' + \rho U'\phi\,,\end{aligned} \tag{B.16}$$

and

$$\widehat{p}' = -\rho(U-c)\phi'' + \rho U''\phi\,. \tag{B.17}$$

Using Eq. B.17, pressure term can be eliminated from the y-direction momentum equation in Eq. B.10.

$$\widehat{k}^2\rho(U-c)\phi = \rho(U-c)\phi'' - \rho U''\phi\,. \tag{B.18}$$

Rearranging the terms and dropping the hat $\widehat{[\cdot]}$ for brevity, we get an ordinary differential equation with the cross-stream streamfunction amplitude as the eigenfunction

$$\rho\left[(U-c)(\phi'' - k^2\phi) - U''\phi\right] = 0\,, \tag{B.19}$$

and the boundary condition is also given in terms of the eigenfunction as

$$k\phi = 0 \quad \text{at} \quad y = y_1, y_2\,. \tag{B.20}$$

The Eqs. B.19-B.20 together form the Rayleigh's equation.

B.2 Matching conditions

To derive the first matching condition, the Rayleigh's equation Eq. B.19 is first rewritten in the following form by using chain rule

$$\left[\rho(U-c)\phi' - \rho U'\phi\right]' = \rho k^2(U-c)\phi\,. \tag{B.21}$$

As the eigenfunction ϕ is continuous across the sections, this equation can be integrated over the discontinuity at y_D

$$\left[\rho(U-c)\phi' - \rho U'\phi\right]_{y_D-\epsilon}^{y_D+\epsilon} = k^2\int_{y_D-\epsilon}^{y_D+\epsilon}\rho(U-c)\phi\,\mathrm{d}y\,. \tag{B.22}$$

The integral on the RHS vanishes in the limit $\epsilon \to 0$ which gives the *dynamic* matching condition

$$\left[\!\left[\rho(U-c)\phi' - \rho U'\phi\right]\!\right] = 0\,, \tag{B.23}$$

where $[\![\cdot]\!]$ gives the *jump* in a quantity. This matching condition for ϕ is equivalent to equating the pressure across the discontinuity. This can be verified from the Eq. B.16 also which has the same form as the terms inside brackets in Eq. B.1. The second matching condition is obtained by dividing the expression for pressure from Eq. B.16 by $(U-c)^2$

$$\frac{\widehat{p}}{(U-c)^2} = -\frac{\rho\phi'}{(U-c)} + \frac{\rho U'\phi}{(U-c)^2} = -\left[\frac{\rho\phi}{(U-c)}\right]' . \tag{B.24}$$

Integrating this equation over the discontinuity at y_D gives

$$\left[\frac{\rho\phi}{(U-c)}\right]_{y_D-\epsilon}^{y_D+\epsilon} = -\int_{y_D-\epsilon}^{y_D+\epsilon} \frac{\widehat{p}}{(U-c)^2}\,\mathrm{d}y\,. \tag{B.25}$$

Again, the integral on the RHS vanishes in the limit $\epsilon \to 0$ which gives the *kinematic* matching condition

$$\left[\!\!\left[\frac{\rho\phi}{(U-c)}\right]\!\!\right] = 0\,. \tag{B.26}$$

□

Appendix C

Dynamic matching condition for interface with non-zero surface tension

For shear layers with a finite value of surface tension σ, the dynamic matching condition includes the resulting pressure jump Δp^{d}, which is given as

$$\left[\!\left[\rho_i(U_i - c^{\mathrm{d}})\phi_i' - \rho_i U_i'\phi_i\right]\!\right] \mathrm{e}^{\mathrm{i}(k^{\mathrm{d}}x^{\mathrm{d}} - \omega^{\mathrm{d}}t^{\mathrm{d}})} = \Delta p^{\mathrm{d}}\,. \tag{C.1}$$

The instantaneous shape of the perturbed interface is shown in Fig. C.1. In three-dimensions, for

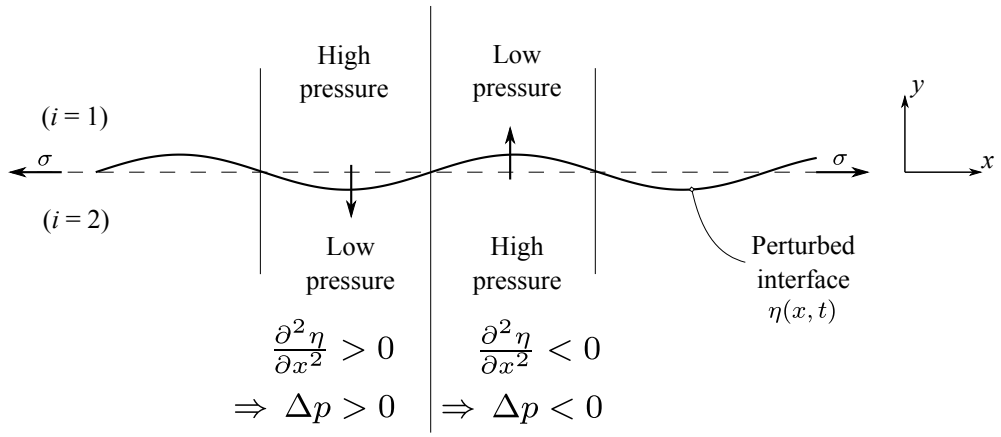

Figure C.1: Instantaneous shape of the perturbed interface $y = \eta(x,t)$

an interface with the principal curvatures as R_1 and R_2, the pressure jump is given as

$$\Delta p^{\mathrm{d}} = \sigma\left(\frac{1}{R_1} + \frac{1}{R_2}\right)\,. \tag{C.2}$$

While calculating Δp, the pressure is higher on the concave side of the interface. The curvature can also be defined in terms of the outward unit normal of the interface as $R_1^{-1} + R_2^{-1} = \nabla\cdot\widehat{\mathbf{n}}$. Thus,

$$\Delta p^{\mathrm{d}} = \sigma\nabla\cdot\widehat{\mathbf{n}}^{\mathrm{d}}\,. \tag{C.3}$$

The superscript 'd' representing dimensional quantities can be dropped for brevity. The perturbed interface can be expressed in the modal decomposed form as

$$\eta(x,t) = \widetilde{\eta_0} \mathrm{e}^{\mathrm{i}(kx-\omega t)} \,. \tag{C.4}$$

The normal to the interface is given as $\mathbf{n} = \pm\nabla(y-\eta)$. The sign of the normal vector is decided by the outward normal which in turn is decided by the definition of the two streams as outer and inner flows. If $i = 1$ corresponds to outer flow and $i = 2$ corresponds to inner flow, the outward normal points upwards and the normal vector is positive. Thus, the unit normal vector is given as

$$\widehat{\mathbf{n}} = \frac{\left(\frac{\partial\eta}{\partial x}, 0, 1\right)}{1 + \left(\frac{\partial\eta}{\partial c}\right)^2} \,. \tag{C.5}$$

Linearising the equation gives

$$\widehat{\mathbf{n}} = \left(\frac{\partial\eta}{\partial x}, 0, 1\right) + \mathcal{O} \,. \tag{C.6}$$

The pressure jump then becomes

$$\Delta p = \sigma\nabla\cdot\widehat{\mathbf{n}} = \sigma\frac{\partial^2\eta}{\partial x^2} \,. \tag{C.7}$$

Substituting the expression for $\eta(x,t)$ from Eq. C.4 to Eq. C.7, we get

$$\Delta p = -\sigma k^2 \eta_0 \mathrm{e}^{\mathrm{i}(kx-\omega t)} \,. \tag{C.8}$$

We need to express the perturbation amplitude of the interface η_0 in terms of the amplitude of the perturbation eigenfunctions A and B. For this, the kinematic condition at the interface

$$\left.\frac{\mathrm{D}(y-\eta)}{\mathrm{D}t}\right|_{y=\eta} = 0 \,, \tag{C.9}$$

is used. The equation can be rearranged as

$$\left.\frac{\mathrm{D}y}{\mathrm{D}t}\right|_{y=\eta} = \frac{\mathrm{D}\eta}{\mathrm{D}t} \,. \tag{C.10}$$

The LHS can be expanded using Taylor's expansion as

$$\begin{aligned} \left.\frac{\mathrm{D}y}{\mathrm{D}t}\right|_{y=\eta} &= v(x,\eta,t) \\ &= v(x,0,t) + \eta\frac{\partial v}{\partial y}(x,0,t) + \mathcal{O}(\eta^2) \,. \end{aligned} \tag{C.11}$$

Then, using the identity

$$v(x,y,t) = \frac{\partial\psi_i(x,y,t)}{\partial x} = \mathrm{i}k\phi_i(y)\mathrm{e}^{\mathrm{i}(kx-\omega t)} \,, \tag{C.12}$$

we get

$$\begin{aligned}\left.\frac{\mathrm{D}y}{\mathrm{D}t}\right|_{y=\eta} &= \mathrm{i}k\left[\phi_i(0)+\eta\phi_i'(0)\right]\mathrm{e}^{\mathrm{i}(kx-\omega t)}+\mathcal{O}(\eta^2)\\ &= \mathrm{i}k\phi_i(0)\left[1+\eta\frac{\phi_i'(0)}{\phi(0)}\right]\mathrm{e}^{\mathrm{i}(kx-\omega t)}+\mathcal{O}(\eta^2)\end{aligned} \tag{C.13}$$

The RHS of Eq. C.10 can also be expanded as

$$\begin{aligned}\frac{\mathrm{D}\eta}{\mathrm{D}t} &= \frac{\partial\eta}{\partial t}+\frac{\mathrm{d}x}{\mathrm{d}t}\frac{\partial\eta}{\partial x}\\ &= \frac{\partial\eta}{\partial t}+U_i\frac{\partial\eta}{\partial x}\\ &= \mathrm{i}k(U_i-c)\eta\\ &= \mathrm{i}k(U_i-c^d)\eta_0\mathrm{e}^{\mathrm{i}(kx-\omega t)}\,.\end{aligned} \tag{C.14}$$

Linearising the LHS Eq. C.13 to $\mathcal{O}(\eta)$ and equating with the RHS Eq. C.14, we get

$$\begin{aligned}\mathrm{i}k\phi_i(0) &= \mathrm{i}k(U_i-c)\eta_0\\ \Rightarrow\qquad \eta_0 &= \frac{\phi_i(0)}{(U_i-c)}\,.\end{aligned} \tag{C.15}$$

The interface perturbation amplitude η_0 can be calculated from the appropriate eigenfunction ϕ_i corresponding to any of the streams. Finally, η_0 can be substituted in Eq. C.8 to give the expression for pressure drop

$$\Delta p = -\sigma k^2\frac{\phi_i(0)}{(U_i-c)}\mathrm{e}^{\mathrm{i}(kx-\omega t)}\,. \tag{C.16}$$

□

Appendix D

Dispersion relations for piecewise linear profiles of plane semi-unconfined shear layer

The dispersion relations for the piecewise linear profiles for plane semi-unconfined shear layers is derived using the computer algebra system, MAXIMA. For the derivation, the matching condition was applied to the eigenfunctions given in § 4.3.2. From the two matching conditions, the coefficients of the constants A_i, B_j can be collected in matrix $\mathbf{D}^{\mathrm{d}}(k^{\mathrm{d}}, \omega^{\mathrm{d}})$, which is given as

$$\mathbf{D}(k, \omega) \begin{bmatrix} \mathbf{A} \\ \mathbf{B} \end{bmatrix} = 0 \,, \tag{D.1}$$

where, $\mathbf{A}$ and $\mathbf{B}$ are the column vectors with n element each representing the $2n$ constants A_i, B_j in the ascending order the values of i and j. For example, for 1-piece linear profile, $\mathbf{A} = [A_1 A_2]^{\mathrm{T}}$ and $\mathbf{B} = [B_2 B_3]^{\mathrm{T}}$. The determinant of the $2n \times 2n$ matrix $\mathbf{D}$ gives the dispersion relation as $\mathcal{D}(k, \omega) = \det \mathbf{D}$. Note that the coefficient matrix $\mathbf{D}$ is in terms of non-dimensional variables given by Eq. 4.95.

The non-zero elements of the matrix $\mathbf{D}$ are listed in the following sections.

D.1 1-piece linear profile

For the 1-piece linear profile, the matrix $\mathbf{D}$ is a 4×4 matrix which gives a dispersion relation $\mathcal{D}(k, \omega)$ which is second order in c.

$$
\begin{aligned}
&\mathbf{D}[1,1] = 1\,,\\
&\mathbf{D}[1,2] = -\mathrm{e}^{-\xi}\,,\\
&\mathbf{D}[1,3] = -\mathrm{e}^{+\xi}\,,\\
&\mathbf{D}[2,2] = \mathrm{e}^{+\xi}\,,\\
&\mathbf{D}[2,3] = \mathrm{e}^{-\xi}\,,\\
&\mathbf{D}[2,4] = -\sinh(\xi(h-1))\,,\\
&\mathbf{D}[3,1] = \xi((c-1)\Lambda - 1)(1+S)\,,\\
&\mathbf{D}[3,2] = -(\xi\Lambda(c-1) - \xi - \Lambda)\mathrm{e}^{-\xi}\,,\\
&\mathbf{D}[3,3] = (\xi\Lambda(c-1) - \xi + \Lambda)\mathrm{e}^{+\xi}\,,\\
&\mathbf{D}[4,2] = (\xi\Lambda(c+1) - \xi - \Lambda)\mathrm{e}^{+\xi}\,,\\
&\mathbf{D}[4,3] = -(\xi\Lambda(c+1) - \xi + \Lambda)\mathrm{e}^{-\xi}\,,\\
&\mathbf{D}[4,4] = -\xi\cosh((h-1)\xi)((c+1)\Lambda - 1)(S-1)\,.
\end{aligned}
$$

D.2 3-piece linear profile

For the 3-piece linear profile, the matrix $\mathbf{D}$ is a 8×8 matrix which gives a dispersion relation $\mathcal{D}(k,\omega)$ which is fourth order in c.

$$
\begin{aligned}
&\mathbf{D}[1,1] = 1\,,\\
&\mathbf{D}[1,2] = -\mathrm{e}^{+(a-1)t\xi}\,,\\
&\mathbf{D}[1,5] = -\mathrm{e}^{-(a-1)t\xi}\,,\\
&\mathbf{D}[2,2] = 1\,,\\
&\mathbf{D}[2,3] = -\mathrm{e}^{-at\xi}\,,\\
&\mathbf{D}[2,5] = 1\,,\\
&\mathbf{D}[2,6] = -\mathrm{e}^{+at\xi}\,,\\
&\mathbf{D}[3,3] = \mathrm{e}^{+at\xi}\,,\\
&\mathbf{D}[3,4] = -1\,,\\
&\mathbf{D}[3,6] = \mathrm{e}^{-at\xi}\,,\\
&\mathbf{D}[4,4] = \cosh((a-1)t\xi)\,,\\
&\mathbf{D}[4,7] = \sinh((a-1)t\xi)\,,\\
&\mathbf{D}[4,8] = \sinh((t-h)\xi)\,,
\end{aligned}
$$

$$
\begin{aligned}
\mathbf{D}[5,1] &= 2(a-1)t(1+S)((c-1)\Lambda-1)\xi\,,\\
\mathbf{D}[5,2] &= 2\mathrm{e}^{+(a-1)t\xi}(-(c-1)(a-1)t\xi\Lambda+(at-1)\Lambda+(a-1)t\xi)\,,\\
\mathbf{D}[5,5] &= 2\mathrm{e}^{-(a-1)t\xi}((c-1)(a-1)t\xi\Lambda+(at-1)\Lambda-(a-1)t\xi)\,,\\
\mathbf{D}[6,2] &= -2((a-1)(at-c)t\xi\Lambda+(at-1)\Lambda+(a-1)t\xi)\,,\\
\mathbf{D}[6,3] &= 2(a-1)t\mathrm{e}^{-at\xi}((at-c)\xi\Lambda+\Lambda+\xi)\,,\\
\mathbf{D}[6,5] &= 2((a-1)(at-c)t\xi\Lambda-(at-1)\Lambda+(a-1)t\xi)\,,\\
\mathbf{D}[6,6] &= -2(a-1)t\mathrm{e}^{+at\xi}((at-c)\xi\Lambda-\Lambda+\xi)\,,\\
\mathbf{D}[7,3] &= 2(a-1)t\mathrm{e}^{+at\xi}((at+c)\xi\Lambda-\Lambda-\xi)\,,\\
\mathbf{D}[7,4] &= 2(at-1)\Lambda\,,\\
\mathbf{D}[7,6] &= -2(a-1)t\mathrm{e}^{-at\xi}((at+c)\xi\Lambda+L-\xi)\,,\\
\mathbf{D}[7,7] &= 2(a-1)t((at+c)\Lambda-1)\xi\,,\\
\mathbf{D}[8,4] &= -2((a-1)t\xi((c+1)\Lambda-1)\sinh((a-1)t\xi)+(at-1)\Lambda\cosh((a-1)t\xi))\,,\\
\mathbf{D}[8,7] &= -2((a-1)t\xi((c+1)\Lambda-1)\cosh((a-1)t\xi)+(at-1)\Lambda\sinh((a-1)t\xi))\,,\\
\mathbf{D}[8,8] &= 2(a-1)t(1-S)\cosh((t-h)\xi)((c+1)\Lambda-1)\xi\,.
\end{aligned}
$$

D.3 5-piece linear profile

For the 5-piece linear profile, the matrix $\mathbf{D}$ is a 12×12 matrix which gives a dispersion relation $\mathcal{D}(k,\omega)$ which is sixth order in c.

$$
\begin{aligned}
\mathbf{D}[1,1] &= 1\,,\\
\mathbf{D}[1,2] &= -\mathrm{e}^{+(a-1)t\xi/2}\,,\\
\mathbf{D}[1,7] &= -\mathrm{e}^{-(a-1)t\xi/2}\,,\\
\mathbf{D}[2,2] &= 1\,,\\
\mathbf{D}[2,3] &= -\mathrm{e}^{+(a-1)t\xi/2}\,,\\
\mathbf{D}[2,7] &= 1\,,\\
\mathbf{D}[2,8] &= -\mathrm{e}^{-(a-1)t\xi/2}\,,\\
\mathbf{D}[3,3] &= 1\,,\\
\mathbf{D}[3,4] &= -\mathrm{e}^{-at\xi}\,,\\
\mathbf{D}[3,8] &= 1\,,\\
\mathbf{D}[3,9] &= -\mathrm{e}^{at\xi}\,,\\
\mathbf{D}[4,4] &= \mathrm{e}^{at\xi}\,,\\
\mathbf{D}[4,5] &= -1\,,\\
\mathbf{D}[4,9] &= \mathrm{e}^{-at\xi}\,,\\
\mathbf{D}[5,5] &= \cosh((a-1)t\xi/2)\,,\\
\mathbf{D}[5,6] &= -1\,,
\end{aligned}
$$

$$
\begin{aligned}
\mathbf{D}[5,10] &= \sinh((a-1)t\xi/2)\,,\\
\mathbf{D}[6,6] &= \cosh((a-1)t\xi/2)\,,\\
\mathbf{D}[6,11] &= \sinh((a-1)t\xi/2)\,,\\
\mathbf{D}[6,12] &= \sinh((t-h)\xi)\,,\\
\mathbf{D}[7,1] &= (a-1)((c-1)\Lambda-1)t\xi\,,\\
\mathbf{D}[7,2] &= -((a-1)((c-1)\Lambda-1)t\xi - 2\Lambda\tanh((a+1)t/2)+2\Lambda)\mathrm{e}^{+(a-1)t\xi/2}\,,\\
\mathbf{D}[7,7] &= ((((a-1)c-a+1)\Lambda-a+1)t\xi + 2\Lambda\tanh((a+1)t/2)-2\Lambda)\mathrm{e}^{-(a-1)t\xi/2}\,,\\
\mathbf{D}[8,2] &= ((1-a)\Lambda t\tanh((a+1)t/2)+((a-1)c\Lambda-a+1)t)\xi - 2\Lambda\tanh((a+1)t/2)+2\Lambda\,,\\
\mathbf{D}[8,3] &= (((a-1)\Lambda t\tanh((a+1)t/2)+((1-a)c\Lambda+a-1)t)\xi\\
&\quad - 2\Lambda\tanh((a+1)t/2)+2a\Lambda t)\mathrm{e}^{+(a-1)t\xi/2}\,,\\
\mathbf{D}[8,7] &= ((a-1)\Lambda t\tanh((a+1)t/2)+((1-a)c\Lambda+a-1)t)\xi - 2\Lambda\tanh((a+1)t/2)+2\Lambda\,,\\
\mathbf{D}[8,8] &= -(((a-1)\Lambda t\tanh((a+1)t/2)+((1-a)c\Lambda+a-1)t)\xi\\
&\quad + 2\Lambda\tanh((a+1)t/2)-2a\Lambda t)\mathrm{e}^{-(a-1)t\xi/2}\,,\\
\mathbf{D}[9,3] &= ((a-a^2)\Lambda t^2+((a-1)c\Lambda-a+1)t)\xi + 2\Lambda\tanh((a+1)t/2)-2a\Lambda t\,,\\
\mathbf{D}[9,4] &= (((a^2-a)\Lambda t^2+((1-a)c\Lambda+a-1)t)\xi+(a-1)\Lambda t)\mathrm{e}^{-at\xi}\,,\\
\mathbf{D}[9,8] &= ((a2-a)\Lambda t^2+((1-a)c\Lambda+a-1)t)\xi + 2\Lambda\tanh((a+1)t/2)-2a\Lambda t\,,\\
\mathbf{D}[9,9] &= (((a-a^2)\Lambda t^2+((a-1)c\Lambda-a+1)t)\xi+(a-1)\Lambda t)\mathrm{e}^{at\xi}\,,\\
\mathbf{D}[10,4] &= (((a^2-a)\Lambda t^2+((a-1)c\Lambda-a+1)t)\xi+(1-a)\Lambda t)\mathrm{e}^{at\xi}\,,\\
\mathbf{D}[10,5] &= 2a\Lambda t - 2\Lambda\tanh((a+1)t/2)\,,\\
\mathbf{D}[10,9] &= -(((a^2-a)\Lambda t^2+((a-1)c\Lambda-a+1)t)\xi+(a-1)\Lambda t)\mathrm{e}^{-at\xi}\,,\\
\mathbf{D}[10,10] &= ((a^2-a)\Lambda t^2+((a-1)c\Lambda-a+1)t)\xi\,,\\
\mathbf{D}[11,5] &= ((1-a)\Lambda t\tanh((a+1)t/2)+((1-a)c\Lambda+a-1)t)\xi\sinh((a-1)t\xi/2)\\
&\quad + (2\Lambda\tanh((a+1)t/2)-2a\Lambda t)\cosh((a-1)t\xi/2)\,,\\
\mathbf{D}[11,6] &= 2\Lambda\tanh((a+1)t/2)-2\Lambda\,,\\
\mathbf{D}[11,10] &= (2\Lambda\tanh((a+1)t/2)-2a\Lambda t)\sinh((a-1)t\xi/2)+((1-a)\Lambda t\tanh((a+1)t/2)\\
&\quad + ((1-a)c\Lambda+a-1)t)\xi\cosh((a-1)t\xi/2)\,,\\
\mathbf{D}[11,11] &= ((a-1)\Lambda t\tanh((a+1)t/2)+((a-1)c\Lambda-a+1)t)\xi\,,\\
\mathbf{D}[12,6] &= ((((1-a)c-a+1)\Lambda+a-1)t\xi\sinh((a-1)t\xi/2)\\
&\quad + (2\Lambda-2\Lambda\tanh((a+1)t/2))\cosh((a-1)t\xi/2)\,,\\
\mathbf{D}[12,11] &= (2\Lambda-2\Lambda\tanh((a+1)t/2))\sinh((a-1)t\xi/2)\\
&\quad + (((1-a)c-a+1)\Lambda+a-1)t\xi\cosh((a-1)t\xi/2)\,,\\
\mathbf{D}[12,12] &= (((a-1)c+a-1)\Lambda-a+1)t\xi\cosh((t-h)\xi)\,.
\end{aligned}
$$

□

References

[1] T. F. Balsa. On the spatial instability of piecewise linear free shear layers. *Journal of Fluid Mechanics*, 174:553–563, 1987.

[2] A. S. Bers. Space-Time Evolution of Plasma instabilities. In M.N Rosenbluth and R.Z. Sagdeev, editors, *Basic Plasma Physics*, chapter 3.2, pages 451–517. North-Holland Publishing Company, 1983.

[3] R. J. Briggs. *Electron-stream Interaction with Plasmas*, volume 29 of *M.I.T. Press Research Monographs*. M.I.T. Press, 1964.

[4] M. Chiatto. Numerical study of plasma jets by means of linear stability theory. *RM Report*, 2014.

[5] P. G. Drazin. *Introduction to Hydrodynamic Stability*. Cambridge Texts in Applied Mathematics. Cambridge University Press, 2002.

[6] D. Duffy. *Green's Functions with Applications*. Chapman and Hall/CRC, 2nd edition, 2015.

[7] M. Gaster. A note on the relation between temporally-increasing and spatially-increasing disturbances in hydrodynamic stability. *Journal of Fluid Mechanics*, 14(02):222–224, 1962.

[8] M. Gaster, E. Kit, and I. Wygnanski. Large-scale structures in a forced turbulent mixing layer. *Journal of Fluid Mechanics*, 150:23–39, 1985.

[9] K. J Groot, Q. Ye, B. W. van Oudheusden, Y. Zhang, and F. Pinna. Biglobal stability analysis of a micro-ramp wake using piv base flows. In *46th AIAA Fluid Dynamics Conference*, page 4383, 2016.

[10] C. M. Ho and P. Huerre. Perturbed free shear layers. *Annual Review of Fluid Mechanics*, 16(1):365–422, 1984.

[11] P. Huerre and P. A. Monkewitz. Absolute and convective instabilities in free shear layers. *Journal of Fluid Mechanics*, 159:151–168, 1985.

[12] P. Huerre and P. A. Monkewitz. Local and global instabilities in spatially developing flows. *Annual Review of Fluid Mechanics*, 22(1):473–537, 1990.

[13] J. Jiménez. *The Global Geometry of Turbulence: Impact of Nonlinear Dynamics*, volume 268. Springer Science & Business Media, 2012.

[14] M. P. Juniper. The full impulse response of two-dimensional jet/wake flows and implications for confinement. *Journal of Fluid Mechanics*, 590:163–185, 2007.

[15] M. P. Juniper. The effect of confinement on the stability of non-swirling round jet/wake flows. *Journal of Fluid Mechanics*, 605:227–252, 2008.

[16] M. P. Juniper, A. Hanifi, and V. Theofilis. Modal Stability Theory: Lecture notes from the FLOW-NORDITA Summer School on Advanced Instability Methods for Complex Flows, Stockholm, Sweden, 2013. *Applied Mechanics Reviews*, 66(2):024804–024804, 2014.

[17] M.P. Juniper. The effect of confinement on the stability of two-dimensional shear flows. *Journal of Fluid Mechanics*, 565:171–195, 2006.

[18] K. Kupfer, A. Bers, and A. K. Ram. The cusp map in the complex-frequency plane for absolute instabilities. *Physics of Fluids (1958-1988)*, 30(10):3075–3082, 1987.

[19] L. D. Landau and E. M. Lifshitz. *Electrodynamics of Continuous Media*. Elsevier, 2nd edition, 1984. p. 113.

[20] R. J. Lingwood. Absolute instability of the boundary layer on a rotating disk. *Journal of Fluid Mechanics*, 299:17–33, 1995.

[21] P. Meliga, D. Sipp, and J.-M. Chomaz. Absolute instability in axisymmetric wakes: compressible and density variation effects. *Journal of Fluid Mechanics*, 600:373–401, 2008.

[22] A. Michalke. Instability of a compressible circular free jet with consideration of the influence of the jet boundary layer thickness. Technical Report 19780008055, NASA; Washington, DC, United States, 1977. Transl. into ENGLISH from Z. für Flugwissenschaften (West-Germany), v. 19, no. 8/9, 1971 p 319-328.

[23] P. A. Monkewitz and K. Sohn. Absolute instability in hot jets. *AIAA Journal*, 26(8):911–916, 1988.

[24] B. Pier and P. Huerre. Nonlinear self-sustained structures and fronts in spatially developing wake flows. *Journal of Fluid Mechanics*, 435:145–174, 2001.

[25] F. Pinna. Numerical study of stability of flows from low to high mach number. *PhD Dissertation*, 2012.

[26] S. J. Rees. Hydrodynamic instability of confined jets & wakes & implications for gas turbine fuel injectors. *PhD Dissertation*, 2008.

[27] P. J. Schmid and D. S. Henningson. *Stability and Transition in Shear Flows*. Springer New York, 2001.

[28] P. A. Sturrock. Kinematics of growing waves. *Physical Review*, 112(5):1488–1503, 1958.

[29] S. A. Suslov. Numerical aspects of searching convective/absolute instability transition. *Journal of Computational Physics*, 212(1):188–217, 2006.

[30] R. Q. Twiss. On Bailey's Theory of Amplified Circularly Polarized Waves in an Ionized Medium. *Physical Review*, 84(3):448–457, 1951.

[31] R. Q. Twiss. On Oscillations in Electron Streams. *Proceedings of the Physical Society. Section B*, 64(8):654, 1951.

[32] R. Q. Twiss. Propagation in Electron-Ion Streams. *Physical Review*, 88(6):1392–1407, 1952.

[33] M.-H. Yu and P. A. Monkewitz. The effect of nonuniform density on the absolute instability of two-dimensional inertial jets and wakes. *Physics of Fluids A: Fluid Dynamics (1989-1993)*, 2(7):1175–1181, 1990.